Phenomenology of Neutrino Oscillations at the Neutrino Factory

Dissertation zur Erlangung des
naturwissenschaftlichen Doktorgrades
der Bayerischen Julius-Maximilians-Universität Würzburg

vorgelegt von

Jian Tang

aus Hunan, China

Würzburg 2011

Eingereicht am: November 7th, 2011

bei der Fakultät für Physik und Astronomie

1. Gutachter: Prof. Dr. Reinhold Rückl
2. Gutachter: Prof. Dr. Raimund Ströhmer

der Dissertation

1. Prüfer: Prof. Dr. Reinhold Rückl
2. Prüfer: Prof. Dr. Raimund Ströhmer
3. Prüfer: Prof. Dr. Friedrich Röpke

im Promotionskolloquium

Tag des Promotionskolloquiums: December 19th, 2011

Doktorurkunde ausgehändigt am: ______________________

Abstract

We consider the prospects for a neutrino factory measuring mixing angles, the CP violating phase and mass-squared differences by detecting wrong-charge muons arising from the chain $\mu^+ \to \nu_e \to \nu_\mu \to \mu^-$ and the right-charge muons coming from the chain $\mu^+ \to \bar{\nu}_\mu \to \bar{\nu}_\mu \to \mu^+$ (similar to μ^- chains), where $\nu_e \to \nu_\mu$ and $\bar{\nu}_\mu \to \bar{\nu}_\mu$ are neutrino oscillation channels through a long baseline. First, we study physics with near detectors and consider the treatment of systematic errors including cross section errors, flux errors, and background uncertainties. We illustrate for which measurements near detectors are required, discuss how many are needed, and what the role of the flux monitoring is. We demonstrate that near detectors are mandatory for the leading atmospheric parameter measurements if the neutrino factory has only one baseline, whereas systematic errors partially cancel if the neutrino factory complex includes the magic baseline. Second, we perform the baseline and energy optimization of the neutrino factory including the latest simulation results from the magnetized iron neutrino detector (MIND). We also consider the impact of τ decays, generated by appearance channels $\nu_\mu \to \nu_\tau$ and $\nu_e \to \nu_\tau$, on the discovery reaches of the mass orderings, the leptonic CP violation, and the non-zero θ_{13}, which we find to be negligible for the considered detector. Third, we make a comparison of a high energy neutrino factory to a low energy neutrino factory and find that they are just two versions of the same experiment optimized for different regions of the parameter space. In addition, we briefly comment on whether it is useful to build the bi-magic baseline at the low energy neutrino factory. Finally, the effects of one additional massive sterile neutrino are discussed in the context of a combined short and long baseline setup. It is found that near detectors can provide the required sensitivity at the LSND-motivated Δm^2_{41}-range, while some sensitivity can also be obtained in the region of the atmospheric mass splitting introduced by the sterile neutrino from the long baselines.

Kurzzusammenfassung

Wir prüfen die Aussichten einer Neutrino Factory die Mischungswinkel, die CP-verletzende Phase und die Differenz der Massenquadrate mittels Detektion von Myonen mit falschem Vorzeichen, die bei $\mu^+ \to \nu_e \to \nu_\mu \to \mu^-$ und $\mu^+ \to \bar{\nu}_\mu \to \bar{\nu}_\mu \to \mu^+$ (vergleichbar mit μ^-), durch $\nu_e \to \nu_\mu$ und $\bar{\nu}_\mu \to \bar{\nu}_\mu$ als Neutrinooszillationen entstehen, zu messen. Als Erstes untersuchen wir die Physik mit Nahdetektoren und überprüfen die Behandlung systematischer Fehler inklusive der Fehler auf dem Wechselwirkungsquerschnitt und auf dem Neutrinofluss sowie Unsicherheiten des experimentellen Signalhintergrundes. Wir erläutern für welche Messungen Nahdetektoren gebraucht werden, diskutieren wieviele dieser Detektoren benötigt werden und welche Rolle die Überwachung des Neutrinosflusses spielt. Wir demonstrieren, dass Nahdetektoren zwingend für Messungen der atmosphärischen Paramter notwendig sind, falls die Neutrino Factory nur eine sogenannte “baseline” besitzt, wohingegen sich die systematischen Fehler partiell aufheben wenn der Neutrino Factory Komplex die “magic baseline” enthlt. Als Zweites führen wir die baseline- und Energieoptimierung für die Neutrino Factory inklusive der neusten Simulationsergebnisse für den Neutrinodetektor aus magnetisiertem Eisen (MIND) durch. Außerdem betrachten wir den Einfluss von τ-Zerfällen, die durch $\nu_\mu \to \nu_\tau$ oder $\nu_e \to \nu_\tau$ Übergänge erzeugt werden, auf die Massenhierachie, auf die CP-Verletzung und auf den Entdeckungsbereich von θ_{13}, welchen wir im Falle des betrachteten Detektors für vernachlässigbar befinden. Als Drittes stellen wir einen Vergleich der Hochenergie Neutrino Factory mit der Niederenergie Neutrino Factory an und folgern, dass sie nur zwei Versionen des selben Experimentes sind, das jedoch für unterschiedliche Parameterbereiche optimiert wurde. Zusätzlich kommentieren wir kurz, ob es nützlich wäre die “bi-magic baseline” bei einer Niederenergie Neutrino Factory zu bauen. Schließ werden die Effekte zustzlichen “sterilen” Neutrinos im Kontext eines kombinierten Aufbaus mit kurzer und langer baseline diskutiert. Es zeigt sich, dass Nahdetektoren die benötigte Sensitivität in der LSND-motivierten Δm^2_{41}-Region liefern, während eine gewisse Sensitivität auch mittels der langen baseline im Bereich der atmosphärischen Massenaufspaltung erreicht werden kann, welche durch das sterile Neutrino induziert wurde.

Contents

To my family ···

Chapter 1

Introduction

In the Standard Model (SM) of particle physics, neutrinos are embedded into the three generation of lepton doublets. We name neutrinos by lepton flavors electron neutrinos (ν_e), muon neutrinos (ν_μ) and tau neutrinos (ν_τ). Further, neutrinos are assumed to be massless, left-handed and take part in weak interactions only. Neutrino oscillation experiments, however, have provided compelling evidence that the active neutrinos are massive particles [1], calling for physics beyond the Standard Model. According to the principle in Quantum Mechanics, we know that massive neutrinos must have two different eigenstates: flavor eigenstates and mass eigenstates, and they will mix with each other during neutrino evolutions in space. With knowledge of SM interactions, neutrinos can be detected by weak interactions, in which neutrino flavor states are correlated with the corresponding charged leptons. In fact, we measure neutrino signals by weak interactions in a neutrino detector. Given three generations of massive neutrinos, there must be two characteristic mass squared splittings $(\Delta m^2_{31}\,, \Delta m^2_{21})$[*] and three mixing angles $(\theta_{12}\,, \theta_{13}\,, \theta_{23})$ as well as a Dirac-type CP violation phase δ_{CP} affecting neutrino oscillations. From now on we will not mention the existence of Majorana neutrino phases because they will not be involved in neutrino oscillations. Disappearance of muon neutrinos, which is mainly driven by $|\Delta m^2_{31}|$ and θ_{23}, has been observed in atmospheric neutrino oscillation experiments, such as Super-Kamiokande [2], and in the MINOS long baseline experiment [3]. Disappearance of electron neutrinos has been observed from solar neutrino oscillation experiments very sensitive to θ_{12} [4], whereas Δm^2_{21} has been strongly constrained by the KamLAND long baseline reactor neutrino experiment [5]. The CHOOZ short-baseline reactor neutrino oscillation experiment [6] has provided a limit of $\sin^2 2\theta_{13} \lesssim 0.1$. There are still unknown problems in the standard scenario: whether $\Delta m^2_{31} > 0$ (normal ordering) or $\Delta m^2_{31} < 0$ (inverted ordering); the value of θ_{13}, as there has been a recent hint for $\theta_{13} > 0$ [7], and whether there is CP violation (CPV) in the lepton sector. Recently there is a piece of exciting news from T2K [8], where they claimed a 2.5σ discovery of non-zero θ_{13}. In

---

[*] We use the convention: $\Delta m^2_{ij} \equiv m^2_i - m^2_j$ through the whole context.

addition, the collaboration group at MINOS shows us results which disfavor the zero θ_{13} hypothesis at 89% confidence level [9]. As an exotic result, OPERA reports that a neutrino might travel with the velocity faster than the speed of light [10].

Apart from the aforementioned measurements, there has been the exceptional LSND measurement related to an incompatible anomaly [11]. The simplest interpretation has been an additional sterile neutrino added to the standard picture with $|\Delta m^2_{41}| \gg |\Delta m^2_{31}|$. A global fit to all experimental data, however, is not in favor to this hypothesis [12], which means that more exotic scenarios would be required to describe this anomaly, such as a decaying sterile neutrino [13]. The recent results from MiniBooNE, however, are consistent with sterile neutrino oscillations in the antineutrino sector [14]. If we assume there is an additional sterile neutrino, four mass eigenstates bring in six mass squared differences $(\Delta m^2_{31}, \Delta m^2_{21}, \Delta m^2_{41}, \Delta m^2_{42}, \Delta m^2_{43})$, six mixing angles $(\theta_{12}, \theta_{13}, \theta_{23}, \theta_{14}, \theta_{24}, \theta_{34})$ and three Dirac CP phases $(\delta_1, \delta_2, \delta_3)$. It is worth noting that an interpretation of LSND results requires significant mixings with the active neutrinos, whereas small mixings are not excluded even if $|\Delta m^2_{41}| \gg |\Delta m^2_{31}|$. On the other hand, sterile neutrinos with $|\Delta m^2_{41}| \sim |\Delta m^2_{31}|$ or $|\Delta m^2_{41}| \sim \Delta m^2_{21}$, as they are motivated by a recent cosmological data analysis [15], have been hardly studied in the literature. Without doubt, such sterile neutrinos have to have small mixings with the active ones in order not to spoil the leading three-flavor fits.

We need more powerful neutrino oscillation experiments in the future to conduct the standard measurements required by three active neutrinos and find clues whether there are any sterile neutrinos or not. A Neutrino Factory is presented as the most powerful machine to study neutrino oscillation physics, where electron neutrinos and muon neutrinos are produced by pure muon decays. Then signals are followed by wrong-charge muons arising from the chain $\mu^+ \to \nu_e \to \nu_\mu \to \mu^-$ and the right-charge muons coming from the chain $\mu^+ \to \bar{\nu}_\mu \to \bar{\nu}_\mu \to \mu^+$ (similar to μ^- chains), where $\nu_e \to \nu_\mu$ and $\bar{\nu}_\mu \to \bar{\nu}_\mu$ are neutrino oscillation channels through a long baseline. The requirements can not be fulfilled without charge identifications in the detector. The feasibility has been subject of several, extensive international studies, such as in [16–18]. The International Neutrino Factory and Superbeam Scoping Study [18–20] has laid the foundations for the currently ongoing Design Study for the Neutrino Factory (IDS-NF) [21]. The goal of the IDS-NF is to present a conceptual design report, a schedule, a cost estimate, and a risk assessment for a Neutrino Factory facility by 2013. The IDS-NF defines a first-version baseline setup of a High Energy Neutrino Factory (HENF) with $E_\mu = 25\,\mathrm{GeV}$ and two baselines $L_1 \simeq 3\,000 - 5\,000\,\mathrm{km}$ and $L_2 \simeq 7\,500\,\mathrm{km}$ (the "magic" baseline [22]) served by two racetrack-shaped storage rings, with a muon energy of 25 GeV based on optimization discussions [23–30] in details. A key component is the magnetized iron detector (MIND) as a far detector, where the magnetization is able to distinguish the "right-sign" muons from the "wrong-sign" ones. This setup has been demonstrated to have excellent discovery reaches in $\sin^2 2\theta_{13}$ in order to address the open questions in the three flavor scenario [28], to be robust against many potential new physics effects [30,31] or systematic errors [32], and to be useful for degeneracy resolution independently of the finally achieved luminosity [22];

and for the physics case in terms of the very long baseline [29]. The neutrino factory is claimed to be a precision instrument not only because it can answer the unknown problems addressed above, but also because it can tell us the story beyond three flavor neutrino oscillation physics. Examples are unitarity violations of the mixing matrix coming from heavy fermion singlets [33–38] and non-standard interactions during neutrino productions, propagation in matter, or detection [30, 31, 38–44]. As for a more recent development, a Low-Energy Neutrino Factory (LENF) with $E_\mu \simeq 4\,\mathrm{GeV}$ to $5\,\mathrm{GeV}$ has been proposed as an alternative to the HENF [45–48]. The main purpose of this alternative has been the reduction of accelerator cost in the case of large θ_{13}. While the HENF relies on the MIND, the LENF has been proposed to use a magnetized Totally Active Scintillator Detector (TASD), which allows for a lower threshold, better energy resolution, and (possibly) electron charge identification.

In this thesis, we first introduce a basic description of neutrino oscillations in quantum mechanics in the Chapter 2. In the Chapter 3, we present a short review of current neutrino oscillation experiments and the progress of the next generation neutrino experiment. The Chapter 4 is devoted to the basic idea and status of the neutrino factory. In the Chapter 5, we propose the use of near detector technologies to monitor beam fluxes in order to reduce systematic uncertainties at the neutrino factory. The consequent physics performance is judged. After this, we revisit the optimization of the neutrino factory in the Chapter 6 with the latest migration matrices which provide a correlation of efficiencies between the true neutrino energy with the reconstructed neutrino energy. The impact of backgrounds coming from tau neutrinos is also included in the physics study. A scan of the baseline L and the beam energy E is discussed. Based on the knowledge of L/E, we make a comparison of physics performance between the HENF and the LENF, where both adopt the same type of neutrino detections based on the MIND in consistency. A minimal requirement of the LENF for three physics performance indicators is illustrated in the Chapter 7. In the Chapter 8, we comment on the existence of the bimagic baseline at a low energy neutrino factory as suggested in [49]. In the Chapter 9, we extend our physics searches with a neutrino factory to three active neutrino plus one sterile neutrino. A basic descriptions of new oscillation probabilities are provided. We also compare physics sensitivities of mixing angles and mass squared differences at a high energy neutrino factory with those given by MINOS. Finally, we summarize and give an outlook for future studies in the same direction. If one is interested in some derivations of oscillation probabilities based on perturbative expansions, please refer to the appendices. Moreover, some inputs of muon fluxes and cross sections are also shown in the appendices.

Chapter 2

Theoretical descriptions of neutrino oscillations

Massive neutrinos propagate in space-time with mass eigenstates while neutrinos in experiment are measured by flavor interactions. The coherence between mass eigenstates and flavor eigenstates provides us with a phenomenology of neutrino oscillation. It is a natural consequence of quantum theory. Once a neutrino oscillation is observed in experiments, it is also a direct proof of massive neutrinos which is certainly a signal beyond current standard model (SM) where neutrinos are massless. Usually we can categorize neutrinos into two types: active neutrinos which participate in SM interactions and sterile neutrinos which have no SM interactions. It is adopted also because of the different pictures of neutrino oscillations in matter, as we will see later.

2.1 Two active neutrinos in vacuum and matter

We can describe the neutrino oscillation by coherent quantum states. Suppose that we have a state mixture of two neutrino species $|\nu_a\rangle$ and $|\nu_b\rangle$ in the flavor basis or $|\nu_1\rangle$ and $|\nu_2\rangle$ in the mass basis with the form:

$$\Phi(x) = \Phi_a(x)|\nu_a\rangle + \Phi_b(x)|\nu_b\rangle = \Phi_1(x)|\nu_1\rangle + \Phi_2(x)|\nu_2\rangle \,, \tag{2.1}$$

and in terms of Dirac equations ($\beta \equiv \gamma_0 \,, \alpha_x \equiv \gamma_0\gamma_x$), we derive the equations of motion for neutrinos in the mass basis:

$$E\Phi_1(x) \quad = \left[-i\alpha_x \tfrac{\partial}{\partial x} + \beta m_1\right] \Phi_1(x) \tag{2.2}$$

$$E\Phi_2(x) \quad = \left[-i\alpha_x \tfrac{\partial}{\partial x} + \beta m_2\right] \Phi_2(x) \,. \tag{2.3}$$

Simplify it and decompose $\Phi_i(x) = \nu_i(x)\phi_i$ $(i = 1, 2)$ where ϕ_i is the Dirac spinor satisfying:

$$\left(\alpha_x \sqrt{E^2 - m_i^2} + \beta m_i\right) \phi_i = E\phi_i \,. \tag{2.4}$$

Then ϕ_i has the free spinor solutions with energy E:

$$-i\frac{\partial\nu_1(x)}{\partial x} = \sqrt{E^2 - m_1^2}\nu_1(x) \tag{2.5}$$

$$-i\frac{\partial\nu_2(x)}{\partial x} = \sqrt{E^2 - m_2^2}\nu_2(x)\,. \tag{2.6}$$

If we take the relativistic limit $\sqrt{E^2 - m_i^2} \approx E - \frac{m_i^2}{2E}$, they can be rewritten as:

$$-i\frac{\partial}{\partial x}\begin{bmatrix} \nu_1(x) \\ \nu_2(x) \end{bmatrix} = \begin{bmatrix} E - \frac{m_1^2}{2E} & 0 \\ 0 & E - \frac{m_2^2}{2E} \end{bmatrix}\begin{bmatrix} \nu_1(x) \\ \nu_2(x) \end{bmatrix} \tag{2.7}$$

We can always go back to the flavor basis by unitary transformations:

$$\nu_\alpha = U_{\alpha i}(\theta)\nu_i \text{ with } U = \begin{bmatrix} \cos\theta & \sin\theta \\ -\sin\theta & \cos\theta \end{bmatrix} \tag{2.8}$$

The evolution equation in the flavor basis is:

$$-i\frac{\partial}{\partial x}\begin{bmatrix} \nu_\alpha(x) \\ \nu_\beta(x) \end{bmatrix} = U\begin{bmatrix} E - \frac{m_1^2}{2E} & 0 \\ 0 & E - \frac{m_2^2}{2E} \end{bmatrix}U^\dagger\begin{bmatrix} \nu_\alpha(x) \\ \nu_\beta(x) \end{bmatrix} \tag{2.9}$$

Explicitly, it becomes:

$$-i\frac{\partial}{\partial x}\begin{bmatrix} \nu_\alpha \\ \nu_\beta \end{bmatrix} = \left\{\left[E - \frac{m_1^2 + m_2^2}{4E}\right]\mathbf{I_2} - \begin{bmatrix} -\frac{\Delta m_{21}^2}{4E}\cos 2\theta & \frac{\Delta m_{21}^2}{4E}\sin 2\theta \\ \frac{\Delta m_{21}^2}{4E}\sin 2\theta & \frac{\Delta m_{21}^2}{4E}\cos 2\theta \end{bmatrix}\right\}\begin{bmatrix} \nu_\alpha \\ \nu_\beta \end{bmatrix} \tag{2.10}$$

The first term on the right-hand side will only provide an overall phase for all flavors during the evolution of neutrinos, which is irrelevant to neutrino flavor oscillations. From now on, we can safely suppress this term. Meanwhile, we change the notation by $\dot{\nu} \equiv \frac{\partial\nu}{\partial x}$ and simplify the above differential equations as follows:

$$\ddot{\nu}_\alpha + \omega^2\nu_\alpha = 0 \tag{2.11}$$

$$\ddot{\nu}_\beta + \omega^2\nu_\beta = 0 \tag{2.12}$$

with $\omega \equiv \frac{\Delta m_{21}^2}{4E} \equiv \frac{m_2^2 - m_1^2}{4E}$. As they are standard quantum states in flavor space and start the evolution from ν_α, we should have initial conditions $\nu_\alpha(0) = 1$ and $\nu_\beta(0) = 0$ as well as the normalization requirement $|\nu_\alpha|^2 + |\nu_\beta|^2 = 1$. We solve the standard wave equations to obtain:

$$\nu_\alpha(x) = \sin^2\theta \cdot e^{-i\omega x} + \cos^2\theta \cdot e^{+i\omega x} \tag{2.13}$$

$$\nu_\beta(x) = (\sin\theta\cos\theta) \cdot e^{-i\omega x} - (\sin\theta\cos\theta) \cdot e^{+i\omega x} \tag{2.14}$$

At this moment, we can retrieve why the overall phase term in Eqn.(2.10) can be suppressed. We can always attach the same phase to two evolv ed flavor states without changing the probability. The oscillation probability of $\nu_\alpha \to \nu_\beta$ becomes

$$P(\nu_\alpha \to \nu_\beta) = |\nu_\beta(L)|^2 = 2\sin^2\theta\cos^2\theta\,[1 - \cos(2\omega L)] = \sin^2 2\theta\sin^2\left(\frac{\Delta m_{21}^2}{2E}L\right) \tag{2.15}$$

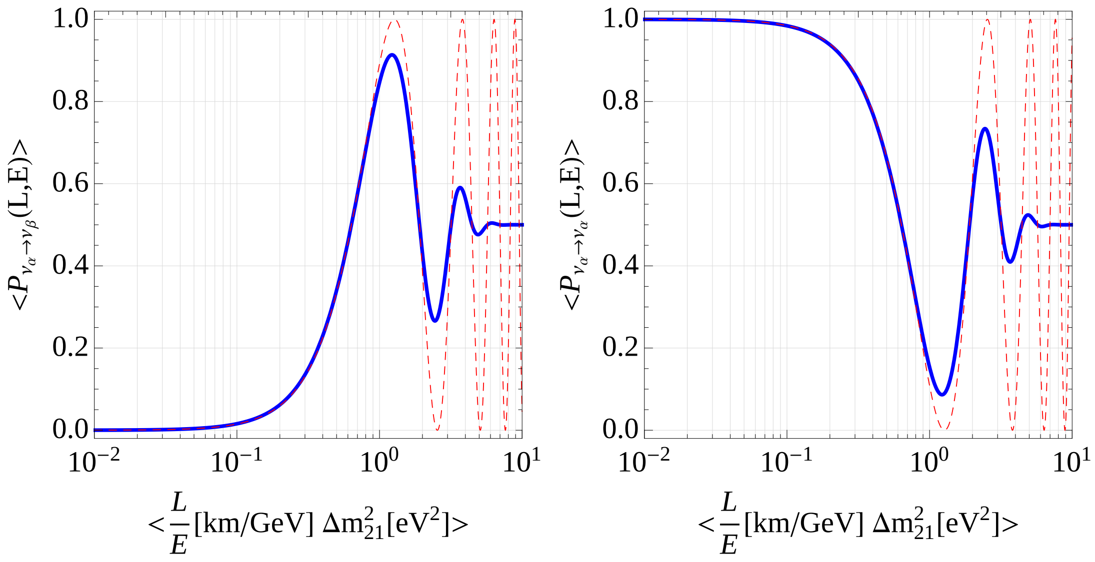

Figure 2.1: *The oscillation probability for two neutrino oscillations in vacuum is expressed by the solid line. The dashed line is the case before introducing the gaussian distribution* $\frac{1}{\sqrt{2\pi}\sigma}e^{-\frac{(L/E-<L/E>)^2}{2\sigma^2}}$ *of* L/E *with the standard deviation* σ *equivalent to* $0.2L/E$. *Here* $\sin^2 2\theta = 1$ *is assumed.*

The picture of two neutrino oscillations in vacuum are depicted in Fig. 2.1. An neutrino oscillation experiment usually has a flat energetic neutrino beam and detectors with a finite energy resolution. We actually measure the average oscillation probability rather than such a completely developed one. A comparison of them is shown by the solid line and the dashed line in Fig. 2.1. To illustrate the difference between the ideal probability and the real probability deduced from event rates, we include a gaussian distribution of L/E with 20% the standard deviation from the mean value for a comparison in Fig. 2.1. In the literature, it is also called the smearing of neutrino spectra by a detector with a finite energy resolution.

The aforementioned discussions are given in the vacuum. As Nature is more complicated, the path of neutrino propagations is full of matter which consists of electrons, protons and neutrons. We have to consider their impacts at the evolution of neutrinos. In a low energy scale limit with $p^2 \ll m_W^2$, we can describe their interactions with neutrinos by the effective Hamiltonian [50]:

$$\mathcal{H}_w = \frac{G_F}{\sqrt{2}}\left[J^{(+)\alpha}(x)J^{(-)}_\alpha(x) + \frac{1}{4}J^{(N)\alpha}(x)J^{(N)}_\alpha(x)\right] \tag{2.16}$$

with the following conventions ($s_w \equiv \sin\theta_{\text{weak}}$):

$$
\begin{aligned}
J_\alpha^{(+)}(x) &= \bar{\nu}_e(x)\gamma_\alpha(1-\gamma_5)e(x) \qquad (2.17)\\
J_\alpha^{(-)}(x) &= \bar{e}(x)\gamma_\alpha(1-\gamma_5)\nu_e(x) \qquad (2.18)\\
J_\alpha^{(N)}(x) &= \bar{\nu}_e\gamma_\alpha(1-\gamma_5)\nu_e(x) - \bar{e}[\gamma_\alpha(1-\gamma_5) - s_w^2\gamma_\alpha]e(x)\\
&\quad +\bar{p}(x)[\gamma_\alpha(1-g_A^p\gamma_5) - 4s_w^2\gamma_\alpha]p(x) - \bar{n}(x)[\gamma_\alpha(1-g_A^n\gamma_5) - 4s_w^2\gamma_\alpha]n(x) \qquad (2.19)
\end{aligned}
$$

where g_A^p and g_A^n are axial vector coupling constants for protons and neutrons, respectively. We take a look at the Charged Current (CC) interactions between neutrinos and electrons at first. Here $J_\alpha^i (i = \pm\, , N)$ expresses the currents in different situations. The average of CC interactions over the electron background in the rest frame of an electron medium is as follows:

$$
H_{CC}^{(e)} = \frac{G_F}{\sqrt{2}} \int d^3p_e f(E_e,T) \sum_s \langle e(s,p_e)|\bar{e}\gamma^\alpha(1-\gamma_5)\nu_e\bar{\nu}_e\gamma_\alpha(1-\gamma_5)e|e(s,p_e)\rangle \ , \tag{2.20}
$$

where $f(E_e,T)$ is the statistical energy distribution of electrons in a homogeneous and isotropic medium with the normalization $\int d^3p_e f(E_e,T) = 1$ and the initial and final electrons sharing the same s and p_e due to coherence. We rearrange it by a Fiertz transformation[*] and expand the electron fields in plane waves:

$$
\langle e(s,p_e)|\bar{e}\gamma_\alpha(1-\gamma_5)e|e(s,p_e)\rangle = \frac{1}{V}\left\langle e(s,p_e)|\bar{u}_s(p_e)a_s^\dagger(p_e)\gamma_\alpha(1-\gamma_5)a_s(p_e)u_s(p_e)|e(s,p_e)\right\rangle
$$

Since $a_s^\dagger(p_e)a_s(p_e) = N_e^{(s)}(p_e)$ is defined by the number density $N_e(p_e)$ with the momentum p_e and assuming there are the same number of electrons with spin 1/2 and $-1/2$:

$$
\begin{aligned}
\sum_s \langle e(s,p_e)|\bar{e}\gamma^\alpha(1-\gamma_5)\nu_e\bar{\nu}_e\gamma_\alpha(1-\gamma_5)e|e(s,p_e)\rangle &= \tfrac{N_e(p_e)}{2}\textstyle\sum_s \bar{u}_s(p_e)\gamma_\alpha(1-\gamma_5)u_s(p_e)\\
&= \tfrac{N_e(p_e)}{2}\mathrm{Tr}\left[\tfrac{\not{p}+m_e}{2E_e}\gamma_\alpha(1-\gamma_5)\right]\\
&= N_e(p_e)\tfrac{(p_e)_\alpha}{E_e} \qquad (2.21)
\end{aligned}
$$

In addition, the isotropic medium implies:

$$
\int d^3p_e\ \vec{\mathbf{p}}_e\ f(E_e,T) = 0\,. \tag{2.22}
$$

It can also be seen by looking at the odd integrand. Finally, we note the average number density of electrons in the medium:

$$
N_e \equiv \int d^3p_e f(E_e,T)N_e(p_e) \tag{2.23}
$$

Therefore, we obtain the final integrated CC Hamiltonian:

$$
\mathcal{H}_{CC}^{(e)} = \frac{G_F N_e}{\sqrt{2}}\bar{\nu}_e(x)\gamma_0(1-\gamma_5)\nu_e(x) \tag{2.24}
$$

---

[*] $\int d^3p_e f(E_e,T)\sum_s \langle|\cdots|\rangle = \bar{\nu}_e\gamma_\alpha(1-\gamma_5)\nu_e \int d^3p_e f(E_e,T)\sum_s \langle e(s,p_e)|\bar{e}\gamma^\alpha(1-\gamma_5)e|e(s,p_e)\rangle$.

Medium	CC potential	NC potential
$e^+\&e^-$	$\pm\sqrt{2}G_F(N_e-N_{\bar{e}})$	$\mp\frac{G_F}{\sqrt{2}}(N_e-N_{\bar{e}})(1-4s_w^2)$
$p\&\bar{p}$	0	$\mp\frac{G_F}{\sqrt{2}}(N_p-N_{\bar{p}})(1-4s_w^2)$
$n\&\bar{n}$	0	$\mp\frac{G_F}{\sqrt{2}}(N_n-N_{\bar{n}})$
Neutral medium $N_e=N_p$	$\pm\sqrt{2}G_FN_e$	$\mp\frac{G_F}{\sqrt{2}}N_n$

Table 2.1: *This table describes the effective potentials for different media.*

The corresponding effective potential for ν_e in an electron medium has the form:

$$V_{CC}=\left\langle\nu_e\left|\int d^3xH^{(e)}_{CC}(x)\right|\nu_e\right\rangle=\sqrt{2}G_FN_e \tag{2.25}$$

What is the value for this potential in practice? The average number density is $N_e=Y_e\rho/m_N$ where Y_e is the relative number density of electrons per nucleon, ρ is the number density with a unit g/cm^3 and m_N is the mass of nucleon. Since a mol of nucleon has one gram mass, the Avogadro constant N_A also means the number of nucleon per mass of the material with a unit $[/g]$.

$$V_{CC}\approx 7.6\times10^{-14}Y_e\frac{\rho}{[g/\mathrm{cm}^3]}\ \mathrm{eV} \tag{2.26}$$

In the earth [†], $Y_e\approx0.494$ and $\rho\approx2.6\mathrm{g/cm}^3$ if it is not too deep so that $V_{CC}\approx10^{-13}$ eV. As for the solar core, $V_{CC}\approx(10^{-14}\sim10^{-12})$ eV while $V_{CC}\approx\mathcal{O}(1)$ eV in supernovae. It is noted that for $\bar{\nu}_e$ we have to reverse the sign of V_{CC} for their effective potentials. As is well known, when light passes such a medium as water, it changes its propagation direction with the index of refraction of 1.33. The neutrino interactions in matter can also be understood as neutrino evolutions with an index of refraction due to coherent interference analogously (see original descriptions in [52–54]). The whole procedure of derivations for V_{CC} can be generalized for neutrino interactions with protons and neutrons. We summarize the effective potentials in Tab. 2.1. One may wonder why the axial vector couplings have no impact in the final effective potential for protons and neutrons. It is because these vector couplings take the form of coefficients in front of γ_5 in Eqn.(2.19) and all the terms containing γ_5 in Eqn.(2.21) disappear after the calculations of matrix trace. The fact that only terms proportional to γ_α are left provides the formalism at Tab.2.1 in the same story.

After introducing the effective potentials in a medium, we can turn to their impacts on neutrino oscillations. Compared to the vacuum evolutions of neutrino in Eqn.(2.10), neutrinos develope their transitions in matter in the flavor basis as follows (given $\nu_\alpha=\nu_e$):

$$-i\frac{\partial}{\partial x}\begin{bmatrix}\nu_e\\ \nu_\beta\end{bmatrix}=\left\{\left[E-V_{NC}-\frac{m_1^2+m_2^2}{4E}\right]\mathbf{I_2}-\begin{bmatrix}V_{CC}-\frac{\Delta m^2_{21}}{4E}\cos2\theta & \frac{\Delta m^2_{21}}{4E}\sin2\theta\\ \frac{\Delta m^2_{21}}{4E}\sin2\theta & \frac{\Delta m^2_{21}}{4E}\cos2\theta\end{bmatrix}\right\}\begin{bmatrix}\nu_e\\ \nu_\beta\end{bmatrix} \tag{2.27}$$

[†] For the details of matter density in the earth, see the Preliminary Reference Earth Model (PREM) [51].

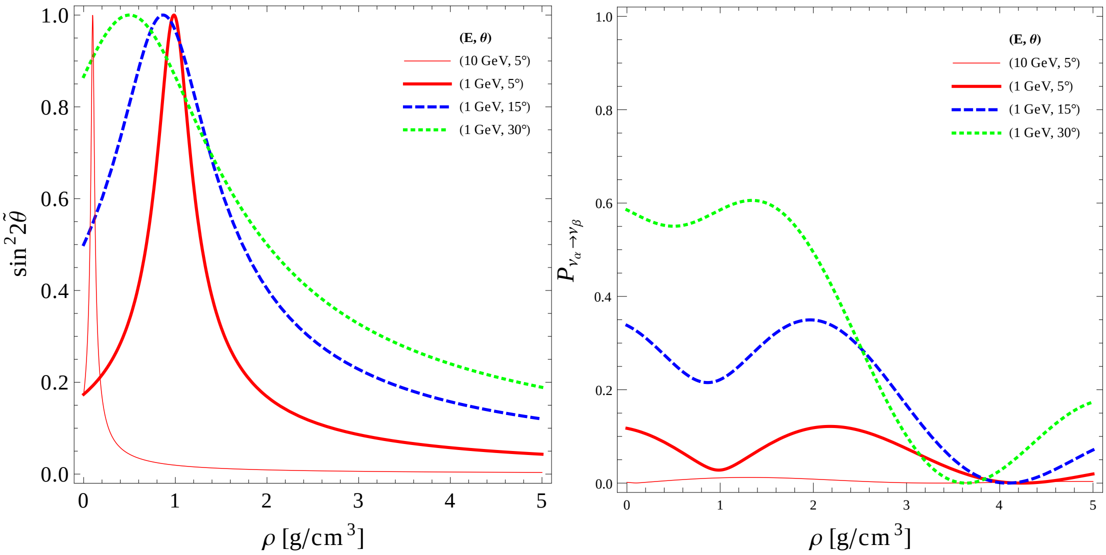

Figure 2.2: *The effective mixing angle and oscillation probability as a function of the matter density. The chosen* Δm^2_{21} *in vacuum is* 7.6×10^{-5} eV^2. *Other parameters like the neutrino energy* E *and mixing angles are shown explicitly in the legend.*

We can also define the effective mixing angles and masses, which are denoted by $\tilde{\theta}$ and $\tilde{m}$, for neutrinos so that they meet the requirements:

$$-i\frac{\partial}{\partial x}\begin{bmatrix}\nu_e\\ \nu_\beta\end{bmatrix} = \left\{\left[E - \frac{\widetilde{m}_1^2 + \widetilde{m}_2^2}{4E}\right]\mathbf{I_2} - \begin{bmatrix} -\frac{\Delta\widetilde{m}^2_{21}}{4E}\cos 2\widetilde{\theta} & \frac{\Delta\widetilde{m}^2_{21}}{4E}\sin 2\widetilde{\theta} \\ \frac{\Delta\widetilde{m}^2_{21}}{4E}\sin 2\widetilde{\theta} & \frac{\Delta\widetilde{m}^2_{21}}{4E}\cos 2\widetilde{\theta}\end{bmatrix}\right\}\begin{bmatrix}\nu_e\\ \nu_\beta\end{bmatrix} \quad (2.28)$$

Apart from the factor in front of the unit matrix which becomes a global phase, we subtract $V_{CC}/2$ in order to produce the same form of Eqn.(2.27) and Eqn.(2.28). Then we find

$$\Delta\widetilde{m}^2_{21}\sin 2\widetilde{\theta} = \Delta m^2_{21}\sin 2\theta \quad (2.29)$$

$$\Delta\widetilde{m}^2_{21}\cos 2\widetilde{\theta} = \Delta m^2_{21}\cos 2\theta - 2E\cdot V_{CC} \quad (2.30)$$

We solve two equations to get the effective mixing angles and masses:

$$\sin 2\widetilde{\theta} = \Delta m^2_{21}\sin 2\theta/\Delta\widetilde{m}^2_{21} \quad (2.31)$$

$$\Delta\widetilde{m}^2_{21} = \sqrt{(\Delta m^2_{21}\sin 2\theta)^2 + (\Delta m^2_{21}\cos 2\theta - 2E\cdot V_{CC})^2} \quad (2.32)$$

Now we could immediately see that the effective mixing angles and mass squared difference differ from those in the vacuum and additionally depend on the neutrino beam energy and the matter potential, *i.e.*, the matter density. To illustrate the dependence, we plot the effective mixing angles and effective oscillation probabilities in Fig. 2.2. In fact, this example is partly what happens to the solar neutrinos, which helps to explain solar neutrino deficits successfully[‡]. Finally, it is also easy to derive two neutrino oscillation

---

[‡] In reality, the survival probability of solar neutrinos includes two parts ($i = 1, 2$): P^{sun}_{ei} where solar ν_e leaves the sun as a mass eigenstates ν_i and P^{earth}_{ie} where a neutrino entering as ν_i arrives at the detector as ν_e.

probability in matter:

$$P(\nu_\alpha \to \nu_\beta) = |\nu_\beta(L)|^2 = \sin^2 2\widetilde{\theta} \sin^2 \left(\frac{\Delta\widetilde{m}^2_{21}}{2E} L \right) . \tag{2.33}$$

2.2 Three active neutrinos in vacuum and matter

As usual, we start the derivation in vacuum. The parametrization of mixing matrix U is the same to that in PDG [55]. It ensures the global fit values of oscillation parameters can be used in the simulations.

$$U = R_{23}(\theta_{23}, 0) R_{13}(\theta_{13}, \delta) R_{12}(\theta_{12}, 0) \tag{2.34}$$

Here $R_{ij}(\theta_{ij},\ \delta_l)$ are the complex rotation matrices in the ij-plane defined as:

$$[R_{ij}(\theta_{ij},\ \delta_l)]_{pq} = \begin{cases} \cos\theta_{ij} & p = q = i, j \\ 1 & p = q \neq i, j \\ \sin\theta_{ij}\ e^{-i\delta_l} & p = i; q = j \\ -\sin\theta_{ij}\ e^{i\delta_l} & p = j; q = i \\ 0 & \text{otherwise.} \end{cases} \tag{2.35}$$

As an analogy to the two-generation case, the three-generation neutrino oscillation probabilities in vacuum have the following form with $\mathcal{J}^{\alpha\beta}_{ij} \equiv U_{\alpha i} U^*_{\alpha j} U^*_{\beta i} U_{\beta j}$:

$$\mathcal{P}_{\alpha\beta} = \delta_{\alpha\beta} - 4\Sigma_{i<j} \mathrm{Re}(\mathcal{J}^{\alpha\beta}_{ij}) \sin^2 \left(\frac{\Delta m^2_{ij}}{4E} L \right) + 2\Sigma_{i<j} \mathrm{Im}(\mathcal{J}^{\alpha\beta}_{ij}) \sin \left(\frac{\Delta m^2_{ij}}{2E} L \right) \tag{2.36}$$

In order to learn the useful oscillation channels, we should further expand the equations up to the next order in terms of small dimensionless parameters. As a first step, we assume a hierarchical ordering of mass eigenstates. For example, assuming $\alpha \equiv |\frac{\Delta m^2_{21}}{\Delta m^2_{31}}| \ll 1$, we can do series expansions in terms of α for each channel with the abbreviations $\Delta_3 = \frac{\Delta m^2_{31}}{4E} L$, $c_{ij} = \cos\theta_{ij}$, $s_{ij} = \sin\theta_{ij}$ and $\delta = \delta_2$:

$$\begin{aligned} \mathcal{P}_{e\mu} &= 2c_{13}s_{13}s^2_{23}\sin^2(\Delta_3)\sin(2\theta_{13}) \\ &+ 2c_{13}s_{12}(\alpha\Delta_3)\left[c_{12}\sin(\Delta_3)\sin(2\theta_{13})\sin(2\theta_{23})\cos(\delta_2 - \Delta_3) - s_{12}s_{13}s^2_{23}\sin(2\Delta_3)\sin(2\theta_{13})\right] \\ &+ 4c_{13}s_{12}(\alpha^2\Delta^2_3)\{\frac{1}{2}s_{13}\cos(2\Delta_3)\left[s_{12}s^2_{23}\sin(2\theta_{13}) - c_{12}c_{13}\cos(\delta_2)\sin(2\theta_{23})\right] \\ &+ \frac{1}{2}c_{12}c_{13}\left[c^2_{23}\sin(2\theta_{12}) + s_{13}\cos(\delta_2)\sin(2\theta_{23})\cos(2\theta_{12}) - s^2_{13}s^2_{23}\sin(2\theta_{12})\right] \\ &- c_{12}c_{13}c_{23}s_{13}s_{23}\sin(\delta_2)\sin(2\Delta_3)\} \end{aligned} \tag{2.37}$$

$$\begin{aligned} \mathcal{P}_{e\tau} &= c^2_{23}\sin^2(\Delta_3)\sin^2(2\theta_{13}) \\ &- 4c^2_{13}c_{23}s_{12}s_{13}(\alpha\Delta_3)\left[2c_{12}s_{23}\sin(\Delta_3)\cos(\delta_2 - \Delta_3) + c_{23}s_{12}s_{13}\sin(2\Delta_3)\right] \\ &+ \frac{1}{2}c^2_{13}s_{12}(\alpha^2\Delta^2)\{4s_{13}\cos^2(\Delta_3)\left[c_{12}\cos(\delta_2)\sin(2\theta_{23}) + 2c^2_{23}s_{12}s_{13}\right] \\ &- c_{12}s_{13}\sin(2\theta_{23})\left[2\cos(\delta_2)\cos(2\theta_{12}) - 3\cos(\delta_2 - 2\Delta_3) + \cos(\delta_2 + 2\Delta_3)\right] \\ &- 4c^3_{12}s_{13}\cos(\delta_2)\sin(2\theta_{23}) - 8c^2_{23}s_{12}s^2_{13}\sin^2(\Delta_3) + 8c^2_{12}s_{12}\left(s^2_{23} - c^2_{23}s^2_{13}\right)\} \end{aligned} \tag{2.38}$$

$$\begin{aligned}
\mathcal{P}_{\mu\tau} &= c_{13}^4 \sin^2(\Delta_3) \sin^2(2\theta_{23}) \\
&+ c_{13}^2(\alpha\Delta_3)\{\sin(2\theta_{23}) \left[\left(s_{12}^2 s_{13}^2 - c_{12}^2\right) \sin(2\Delta_3) \sin(2\theta_{23}) + 2s_{13} \sin(\delta_2) \sin^2(\Delta_3) \sin(2\theta_{12})\right] \\
&- \frac{1}{2} s_{13} \cos(\delta_2) \sin(2\Delta_3) \sin(2\theta_{12}) \sin(4\theta_{23})\} \\
&+ (\alpha^2\Delta_3^2)\{c_{13}^2 s_{13} (-\sin(\delta_2)) \sin(2\Delta_3) \sin(2\theta_{12}) \sin(2\theta_{23}) \\
&+ 2c_{23} c_{13}^2 s_{23} \cos(2\Delta_3) \left[\left(c_{12}^2 - s_{12}^2 s_{13}^2\right) \sin(2\theta_{23}) + s_{13} \cos(\delta_2) \sin(2\theta_{12}) \cos(2\theta_{23})\right] \\
&+ \frac{1}{16}[4c_{12}^2 s_{13}^2 [\cos(4\theta_{23}) - \cos(2\theta_{12})(3\cos(4\theta_{23}) + 5) + 7] \\
&- 4\sin^2(2\theta_{23}) \left[\sin^2(2\theta_{12}) \left(2s_{13}^2 \cos(2\delta_2) + s_{13}^4 + 1\right) - 4s_{12}^4 s_{13}^2\right] \\
&- \cos(\delta_2) \sin(4\theta_{12}) \sin(4\theta_{23}) (\sin(3\theta_{13}) - 7s_{13})]\}
\end{aligned} \tag{2.39}$$

$$\begin{aligned}
\mathcal{P}_{ee} &= 1 - \frac{1}{2} \sin^2(2\theta_{13}) + 2c_{13}^2 s_{13}^2 \cos(2\Delta_3) \\
&+ 4c_{13}^2 s_{12}^2 s_{13}^2 (\alpha\Delta_3) \sin(2\Delta_3) - 4c_{13}^2 s_{12}^2 (\alpha^2\Delta_3^2) \left[c_{12}^2 c_{13}^2 + s_{13}^2 \cos(2\Delta_3)\right]
\end{aligned} \tag{2.40}$$

$$\begin{aligned}
\mathcal{P}_{\mu\mu} &= 1 - c_{13}^2 s_{23}^2 \sin^2(\Delta_3) [3 - \cos(2\theta_{13}) + \cos(2\theta_{23}) + \cos(2\theta_{13}) \cos(2\theta_{23})] \\
&+ 4c_{13}^2 s_{23}^2 \alpha\Delta_3 \sin(\Delta_3) \cos(\Delta_3) \left(s_{13} \left(2s_{12}^2 s_{13} s_{23}^2 - \cos(\delta_2) \sin(2\theta_{12}) \sin(2\theta_{23})\right) + 2c_{12}^2 c_{23}^2\right) \\
&- (\alpha^2\Delta_3^2) \left[2s_{12}^2 s_{13}^2 s_{23}^2 - s_{13} \cos(\delta_2) \sin(2\theta_{12}) \sin(2\theta_{23}) + 2c_{12}^2 c_{23}^2\right] \\
&\times \left[s_{13} \cos(\delta_2) \sin(2\theta_{12}) \sin(2\theta_{23}) + 2c_{13}^2 s_{23}^2 \cos(2\Delta_3) + 2c_{23}^2 s_{12}^2 + 2c_{12}^2 s_{13}^2 s_{23}^2\right]
\end{aligned} \tag{2.41}$$

It is easy to reproduce (3.9)–(3.13) in [56] if we take further series expansions in terms of $s_{13} \ll 1$. In addition, the expanded oscillation probabilities help us check the results obtained in matter perfectly, as we can see later.

What happens if three neutrinos pass through constant matter? First, we can write down the effective Hamiltonian with the help of effective potential in matter in the flavor basis:

$$\mathcal{H}_m = \frac{1}{2E} \left(U\mathbf{M^2}U^\dagger + \mathcal{A}\right) \tag{2.42}$$

without terms contributing to global phases and

$$\mathbf{M^2} = \mathrm{diag}\{0\,, \Delta m_{21}^2\,, \Delta m_{31}^2\} \tag{2.43}$$

$$\mathcal{A} = \mathrm{diag}\{2EV_{CC}\,, 0\,, 0\} \tag{2.44}$$

Similarly, we could correlate it with the effective masses in matter by definitions of the Hamiltonian:

$$\mathcal{H}_m = \frac{1}{2E} \mathrm{diag}\{\widetilde{m}_1^2\,, \widetilde{m}_2^2\,, \widetilde{m}_3^2\} \tag{2.45}$$

2.2.1 Time-independent perturbative expansions I

Assuming $\Delta m_{21}^2 \ll \Delta m_{31}^2$ and the matter induced term $a \equiv 2EV_{CC} \ll \Delta m_{31}^2$, we could separate the effective Hamiltonian:

$$\mathcal{H}_0 = \tfrac{1}{2E} U \mathrm{diag}\{0, 0, \Delta m_{31}^2\} U^\dagger \tag{2.46}$$

$$\mathcal{H}_I = \tfrac{1}{2E} \left[U \mathrm{diag}\{0\,, \Delta m_{21}^2\,, 0\} U^\dagger + \mathrm{diag}\{2EV_{CC}\,, 0\,, 0\}\right] \tag{2.47}$$

In terms of the neutrino evolutions in the flavor space $\nu(x) = S(x)\nu(0)$ with $S(x) \equiv Te^{-i\int_0^x dtH(t)}$, we take $\mathcal{H}_I$ as a perturbation:

$$\Omega(x) = e^{i\mathcal{H}_0 x} S(x) = e^{-i\mathcal{H}_I x} \approx 1 - i\int_0^x dt\mathcal{H}_I(t) \tag{2.48}$$

which is valid under the conditions of $V_{CC} \cdot x \ll 1$ and $\Delta m_{21}^2 \cdot x/(2E) \ll 1$. Therefore, the evolution matrix $S(x) = e^{-i\mathcal{H}_0 x}\Omega(x) \equiv S_0(x) + S_1(x)$ and

$$S_0(x) = \quad e^{-i\mathcal{H}_0 x} \tag{2.49}$$

$$S_1(x) = \quad e^{-i\mathcal{H}_0 x}(-i)\int_0^x dt\mathcal{H}_I(t) \tag{2.50}$$

Explicitly, they are simplified as follows[§]:

$$S_0(x)_{\beta\alpha} = \quad \delta_{\beta\alpha} + (-2i)U_{\beta 3}U_{\alpha 3}^* \sin\frac{\Delta m_{31}^2 \cdot x}{4E} \cdot e^{-i\frac{\Delta m_{31}^2 \cdot x}{4E}} \tag{2.51}$$

$$\begin{aligned} S_1(x)_{\beta\alpha} = \quad & (-2i) \cdot \sin\frac{\Delta m_{31}^2 \cdot x}{4E} \cdot e^{-i\frac{\Delta m_{31}^2 \cdot x}{4E}} \cdot U_{\beta 3}U_{\alpha 3}^* \left[\frac{a}{\Delta m_{31}^2}(\delta_{\alpha e} + \delta_{\beta e} - 2|U_{e3}|^2) - i\frac{a \cdot x}{2E}|U_{e3}|^2\right] \\ & -i\frac{\Delta m_{31}^2 \cdot x}{2E}\left\{\delta_{\alpha e}\delta_{\beta e} + U_{\beta 3}U_{\alpha 3}^*(2|U_{e3}|^2 - \delta_{\alpha e} - \delta_{\beta e})\right\} \end{aligned} \tag{2.52}$$

The oscillation probability can be expressed as:

$$P_{\nu_\alpha \to \nu_\beta}(L) = \quad |S_{\beta\alpha}(L)|^2 = \delta_{\beta\alpha} - 2\mathrm{Im}(T_{\alpha\alpha})\delta_{\beta\alpha} + T_{\beta\alpha}(L)T_{\beta\alpha}^*(L) \tag{2.53}$$

with the definition of $T_{\beta\alpha}(x)$

$$\begin{aligned} iT_{\beta\alpha}(x) = \quad & (-2i) \cdot \sin\frac{\Delta m_{31}^2 \cdot x}{4E} \cdot e^{-i\frac{\Delta m_{31}^2 \cdot x}{4E}} \cdot U_{\beta 3}U_{\alpha 3}^* \left[1 - \frac{a}{\Delta m_{31}^2}(\delta_{\alpha e} + \delta_{\beta e} - 2|U_{e3}|^2) - i\frac{a \cdot x}{2E}|U_{e3}|^2\right] \\ & -i\frac{\Delta m_{31}^2 \cdot x}{2E}\left\{\delta_{\alpha e}\delta_{\beta e} + U_{\beta 3}U_{\alpha 3}^*(2|U_{e3}|^2 - \delta_{\alpha e} - \delta_{\beta e})\right\} \end{aligned} \tag{2.54}$$

Finally, we have the perturbative flavor oscillation probability:

$$\begin{aligned} P_{\nu_\alpha \to \nu_\beta}(L) = \quad & \delta_{\beta\alpha}\left\{1 - 4|U_{\alpha 3}|^2 \sin^2(\Delta_3)\left[1 - \frac{2a}{\Delta m_{31}^2}(|U_{e3}|^2 - \delta_{\alpha e})\right] - \frac{a \cdot L}{E}\sin(2\Delta_3)|U_{\alpha 3}|^2|U_{e3}|^2\right\} \\ & +4\sin^2(\Delta_3)|U_{\beta 3}|^2|U_{\alpha 3}|^2\left[1 - \frac{2a}{\Delta m_{31}^2}(2|U_{e3}|^2 - \delta_{\alpha e} - \delta_{\beta e})\right] \\ & +4\Delta_3\sin(2\Delta_3)\left\{\frac{a}{\Delta m_{31}^2}\left[|U_{e3}|^2\delta_{\alpha e}\delta_{\beta e} + |U_{\beta 3}|^2|U_{\alpha 3}|^2(2|U_{e3}|^2 - \delta_{\alpha e} - \delta_{\beta e})\right]\right. \\ & \left.+\alpha\mathrm{Re}(U_{\beta 3}U_{\alpha 3}^*U_{\beta 2}^*U_{\alpha 2})\right\} - 8(\alpha\Delta_3)\sin^2(\Delta_3)\mathrm{Im}(U_{\beta 3}U_{\alpha 3}^*U_{\beta 2}^*U_{\alpha 2}) \end{aligned} \tag{2.55}$$

[§] See derivations of $S_0(x)$ and $S_1(x)$ in the Appendix 11.1.

After plugging in the mixing matrix elements, we obtain the explicit oscillation channels in the below:

$$\begin{aligned}\mathcal{P}_{ee} &= 1 - \left(1 + \frac{4a}{\Delta m_{31}^2} c_{13}^2\right) \sin^2(2\theta_{13}) \sin^2(\Delta_3) - \frac{aL}{E} s_{13}^4 \sin(2\Delta_3) \\ &+ 4\Delta_3 \sin(2\Delta_3) \left[\frac{a}{\Delta m_{31}^2} s_{13}^2 (1 - c_{13}^2 s_{13}^2) + \alpha s_{12}^2 c_{13}^2 s_{13}^2\right]\end{aligned} \tag{2.56}$$

$$\begin{aligned}\mathcal{P}_{e\mu} &= s_{23}^2 \sin^2(2\theta_{13}) \sin^2(\Delta_3) \left[1 + \frac{2a}{\Delta m_{31}^2} \cos(2\theta_{13})\right] + 8(\alpha\Delta_3) c_{12} c_{13}^2 c_{23} s_{12} s_{13} s_{23} \sin\delta \sin^2(\Delta_3) \\ &+ 4\Delta_3 \sin(2\Delta_3) \left[-c_{13}^2 s_{13}^2 s_{23}^2 \frac{a}{\Delta m_{31}^2} \cos(2\theta_{13}) + \alpha c_{13}^2 s_{12} s_{13} s_{23} \left(c_{12} c_{23} \cos\delta - s_{12} s_{13} s_{23}\right)\right]\end{aligned} \tag{2.57}$$

$$\begin{aligned}\mathcal{P}_{e\tau} &= c_{23}^2 \sin^2(2\theta_{13}) \sin^2(\Delta_3) \left[1 + \frac{2a}{\Delta m_{31}^2} \cos(2\theta_{13})\right] - 8(\alpha\Delta_3) c_{12} c_{13}^2 c_{23} s_{12} s_{13} s_{23} \sin\delta \sin^2(\Delta_3) \\ &+ 4\Delta_3 \sin(2\Delta_3) \left[-c_{13}^2 s_{13}^2 c_{23}^2 \frac{a}{\Delta m_{31}^2} \cos(2\theta_{13}) - \alpha c_{13}^2 c_{23} s_{12} s_{13} \left(c_{12} s_{23} \cos\delta + c_{23} s_{12} s_{13}\right)\right]\end{aligned} \tag{2.58}$$

$$\begin{aligned}\mathcal{P}_{\mu\mu} &= 1 - 4c_{13}^2 s_{23}^2 \left[\left(1 - \frac{2a}{\Delta m_{31}^2} s_{13}^2\right) - c_{13}^2 c_{23}^2 \left(1 - \frac{4a}{\Delta m_{31}^2} s_{13}^2\right)\right] \sin^2(\Delta_3) - \frac{a \cdot L}{E} c_{13}^2 s_{13}^2 s_{23}^2 \sin(2\Delta_3) \\ &+ 4\Delta_3 \sin(2\Delta_3) c_{13}^2 s_{23}^2 \left\{\frac{2a}{\Delta m_{31}^2} c_{13}^2 s_{23}^2 s_{13}^2 + \alpha \left[c_{12}^2 c_{23}^2 + s_{12}^2 s_{13}^2 s_{23}^2 - 2c_{12} c_{23} s_{12} s_{13} s_{23} \cos\delta\right]\right\}\end{aligned} \tag{2.59}$$

$$\begin{aligned}\mathcal{P}_{\mu\tau} &= 4c_{13}^4 c_{23}^2 s_{23}^2 \left(1 - \frac{4a}{\Delta m_{31}^2} s_{13}^2\right) \sin^2(\Delta_3) + 8(\alpha\Delta_3) \sin^2(\Delta_3) c_{12} c_{13}^2 c_{23} s_{12} s_{13} s_{23} \sin\delta \\ &+ 4\Delta_3 \sin(2\Delta_3) \left\{\frac{2a}{\Delta m_{31}^2} c_{13}^4 c_{23}^2 s_{23}^2 + \alpha c_{13}^2 c_{23} s_{23} \left[c_{23} s_{12}^2 s_{13}^2 s_{23} - c_{12}^2 c_{23} s_{23} - c_{12} s_{12} s_{13} \cos(2\theta_{23}) \cos\delta\right]\right\}\end{aligned} \tag{2.60}$$

Switching off the matter effects by $a \rightarrow 0$, we could recover the results in the vacuum. It is a perfect cross check. Now we list the useful remarks in order:

- It should be highlighted that the validity of perturbation requires two conditions: $\frac{a \cdot L}{2E} \ll 1$ and $\frac{\Delta m_{21}^2 \cdot L}{2E} \ll 1$. We take a step further in the quantitative analysis:

  $$\frac{a \cdot L}{2E} = V_{CC} \cdot L \approx 0.50 \left[\frac{\rho}{2.6\mathrm{g/cm}^3}\right] \left[\frac{L}{1000\ \mathrm{km}}\right] \ll 1$$

  $$\frac{\Delta m_{21}^2 \cdot L}{2E} \approx 0.25 \left[\frac{\Delta m_{21}^2}{10^{-5}\mathrm{eV}^2}\right] \left[\frac{L}{1000\ \mathrm{km}}\right] \left[\frac{0.1\ \mathrm{GeV}}{E}\right] \ll 1$$

  The first condition immediately gives the maxmum baseline to be considered while the second one provides the energy threshold allowing us a qualitative discussions based on the above probabilities.

- In the $\mathcal{P}_{ee}$ channel, the dependence of $\sin\theta_{13}$ is universal while there is no dependence of θ_{23}. This explains why we could gain the current knowledge of $\sin^2 2\theta_{13} \leq 0.1$ from reactor neutrino experiments which are sensitive to this channel. Apart from this fact, we could claim that it is extremely hard to make use of this channel in the precision measurements if θ_{13} is too small, irrespective of electron identification difficulties in experimental techniques. However, the channel $\mathcal{P}_{\mu\mu}$ has different features. Even when θ_{13} becomes zero, the dependence on θ_{23} can survive. This implies that this channel is able to provide good measurements of θ_{23}. In turn, it may distinguish the octant degeneracy ($\theta_{23} \neq \pi/4$) in a combination of other channels.
- The CP violation sensitive term $\sin\delta$ is included in the channel $\mathcal{P}_{e\mu}$, $\mathcal{P}_{e\tau}$ and $\mathcal{P}_{\mu\tau}$. They share the same magnitude for $\sin\delta$. It confirms that the T-odd terms in all three transition probabilities must be the same.

2.2.2 Time-independent perturbative expansions II

In the previous section, two conditions have to be satisfied. How can we develop the perturbative expansions of neutrino oscillation probabilities with $\Delta m^2_{21} \ll \Delta m^2_{31}$ but $2E \cdot V_{CC} \sim \Delta m^2_{31}$? At this point, one of the previous conditions is not valid any more. This is an opportunity to explain how to overcome this problem and how to do the time-independent perturbative expansions in a second way. This time, we could rewrite the effective Hamiltonian:

$$\mathcal{H}_m = \frac{\Delta m^2_{31}}{2E}\left\{\hat{R}_{23}(\theta_{23})U_\delta \hat{R}_{13}(\theta_{13})\hat{R}_{12}(\theta_{12})\begin{bmatrix} 0 & 0 & 0 \\ 0 & \alpha & 0 \\ 0 & 0 & 1 \end{bmatrix}\hat{R}^T_{12}(\theta_{12})\hat{R}^T_{13}(\theta_{13})U^\dagger_\delta \hat{R}^T_{23}(\theta_{23}) + \frac{1}{\Delta m^2_{31}}\mathcal{A}\right\}$$

Here $U_\delta = \mathrm{diag}(1, 1, e^{i\delta})$. Since the matter potential matrix $\mathcal{A}$ has no elements at the $2-3$ sector, the rotation matrix $\hat{R}_{23}(\theta_{23})$ commutes with this matrix in the Hamiltonian. It is always convenient to rotate it out before the perturbations so that:

$$\mathcal{H}_m = \frac{\Delta m^2_{31}}{2E}\left\{\hat{R}_{23}(\theta_{23})U_\delta \cdot M \cdot U^\dagger_\delta \hat{R}^T_{23}(\theta_{23})\right\}, \tag{2.61}$$

with

$$M = \hat{R}_{13}(\theta_{13})\hat{R}_{12}(\theta_{12})\begin{bmatrix} 0 & 0 & 0 \\ 0 & \alpha & 0 \\ 0 & 0 & 1 \end{bmatrix}\hat{R}^T_{12}(\theta_{12})\hat{R}^T_{13}(\theta_{13}) + \begin{bmatrix} \frac{a}{\Delta m^2_{31}} & 0 & 0 \\ 0 & 0 & 0 \\ 0 & 0 & 0 \end{bmatrix}.$$

Further, the effective masses in matter can follow as:

$$\mathcal{H}_m = \frac{\Delta m^2_{31}}{2E}\hat{R}_{23}(\theta_{23})U_\delta\left(V\begin{bmatrix} \lambda_1 & 0 & 0 \\ 0 & \lambda_2 & 0 \\ 0 & 0 & \lambda_3 \end{bmatrix}V^\dagger\right)U^\dagger_\delta \hat{R}^T_{23}(\theta_{23}) = \frac{1}{2E}\mathrm{diag}\{\widetilde{m}^2_1, \widetilde{m}^2_2, \widetilde{m}^2_3\}$$

Then it is V that diagonalizes the new matrix M after suppressing the real rotation matrix $\hat{R}_{23}(\theta_{23})$ by $M = V\Lambda V^{\dagger}$ with $\Lambda \equiv \mathrm{diag}(\lambda_1, \lambda_2, \lambda_3)$. It simplifies the diagonalization of original Hamiltonian in mathematics. We follow the standard perturbation theory to expand M:

$$\begin{aligned} M = & \quad M^{(0)} + M^{(1)} + M^{(2)} + \cdots \\ V = & \quad V^{(0)} + V^{(1)} + V^{(2)} + \cdots \end{aligned} \tag{2.62}$$

where $i(i = 0\,, 1\,, 2\,, \cdots)$ in the brackets is the order of the small parameters α and s_{13}. It is easy to show that:

$$\begin{aligned} M^{(0)} = & \begin{bmatrix} \frac{a}{\Delta m^2_{31}} & 0 & 0 \\ 0 & 0 & 0 \\ 0 & 0 & 1 \end{bmatrix}, M^{(1)} = \begin{bmatrix} \alpha s^2_{12} & \alpha c_{12} s_{12} & s_{13} \\ \alpha c_{12} s_{12} & \alpha c^2_{12} & 0 \\ s_{13} & 0 & 0 \end{bmatrix}, \\ M^{(2)} = & \begin{bmatrix} s^2_{13} & 0 & -\alpha s^2_{12} s_{13} \\ 0 & 0 & -\alpha c_{12} s_{12} s_{13} \\ -\alpha s^2_{12} s_{13} & -\alpha c_{12} s_{12} s_{13} & -s^2_{13} \end{bmatrix}. \end{aligned} \tag{2.63}$$

Obviously, $\Lambda^{(0)} = M^{(0)}$. The first order eigenvalues have the form $\Lambda^{(1)}_{ii} = M^{(1)}_{ii}$:

$$\Lambda^{(1)} = \begin{bmatrix} \alpha s^2_{12} & 0 & 0 \\ 0 & \alpha c^2_{12} & 0 \\ 0 & 0 & 0 \end{bmatrix}. \tag{2.64}$$

As for the second order eigenvalues, they meet the requirements $\Lambda^{(2)}_{ii} = M^{(2)}_{ii} + \sum_{i \neq j} \frac{\left[M^{(1)}_{ij}\right]^2}{\lambda^{(0)}_i - \lambda^{(0)}_j}$ in the perturbation such that:

$$\begin{aligned} \lambda^{(2)}_1 = & s^2_{13}\left(1 + \frac{\Delta m^2_{31}}{a - \Delta m^2_{31}}\right) + \alpha^2 c^2_{12} s^2_{12} \frac{\Delta m^2_{31}}{a}, \\ \lambda^{(2)}_2 = & -\alpha^2 c^2_{12} s^2_{12} \frac{\Delta m^2_{31}}{a}, \\ \lambda^{(2)}_3 = & s^2_{13}\,. \end{aligned} \tag{2.65}$$

Therefore, we could have the effective mass eigenstates in matter:

$$\begin{aligned} \widetilde{m}_1 = & \Delta m^2_{31}\left[\frac{a}{\Delta m^2_{31}} + \alpha s^2_{12} + s^2_{13}\left(1 + \frac{\Delta m^2_{31}}{a - \Delta m^2_{31}}\right) + \alpha^2 c^2_{12} s^2_{12} \frac{\Delta m^2_{31}}{a}\right], \\ \widetilde{m}_2 = & \Delta m^2_{31}\left[\alpha c^2_{12} - \alpha^2 c^2_{12} s^2_{12} \frac{\Delta m^2_{31}}{a}\right], \\ \widetilde{m}_3 = & \Delta m^2_{31}\left[1 - s^2_{13} \cdot \frac{a}{a - \Delta m^2_{31}}\right] \end{aligned} \tag{2.66}$$

The illustrative example of effective masses are shown in the left panel of Fig. 2.3. There are two different matter resonance in the evolution of eigenstates. One is at $\mathcal{O}(1)$

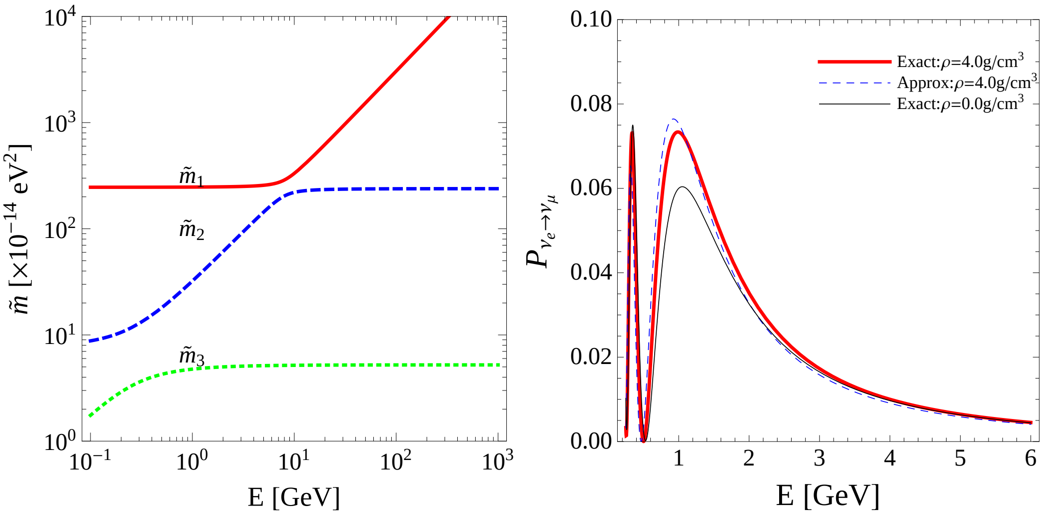

Figure 2.3: *The effective neutrino masses and oscillation probability in a homogeneous matter with a constant density ($\rho = 4.0$ g/cm^3 and $L = 500$ km). The true oscillation parameters are taken as follows: $\theta_{12} = 34°$, $\theta_{13} = 10°$, $\theta_{23} = 45°$, $\delta_{\rm CP} = 0°$, $\Delta m^2_{21} = 7.6 \times 10^{-5}$ eV^2 and $\Delta m^2_{31} = 2.46 \times 10^{-3}$ eV^2, otherwise expressed by legends. A normal mass hierarchy is assumed in the left-hand figure.*

GeV for $\Delta\widetilde{m}^2_{32}$ and the other between $\widetilde{m}_1$ and $\widetilde{m}_2$ is located at $\mathcal{O}(10)$ GeV. It has to be noted that no hierarchy is assumed for the effective masses. We could split V into three eigenvectors $(v_1\,, v_2\,, v_3)$ which correspond to each eigenvalues. The explicit eigenvectors will be calculated up to the second order by:

$$\begin{aligned}
V^{(0)} &= \begin{bmatrix} 1 & 0 & 0 \\ 0 & 1 & 0 \\ 0 & 0 & 1 \end{bmatrix} \\
v_i^{(1)} &= \sum_{i\neq j} \frac{M_{ij}^{(1)}}{\lambda_i^{(0)}-\lambda_j^{(0)}} v_j^{(0)} \\
v_i^{(2)} &= \sum_{i\neq j} \frac{1}{\lambda_i^{(0)}-\lambda_j^{(0)}} \left\{ M_{ij}^{(2)} + \left[M^{(1)} v_i^{(1)}\right]_j - \lambda_i^{(1)} \left[v_i^{(1)}\right]_j \right\} v_j^{(0)}\,.
\end{aligned} \tag{2.67}$$

The details of V up to the second order are given in the Appendix 11.1. The effective mixing matrix in matter is obtained by $\widetilde{U} = \hat{R}_{23}(\theta_{23}) U_\delta V$ with $A \equiv \frac{a}{\Delta m^2_{31}}$ to the first order:

$$\widetilde{U} = \begin{bmatrix} 1 & -\frac{c_{12}s_{12}\alpha}{A} & \frac{s_{13}}{1-A} \\ \frac{c_{12}c_{23}s_{12}\alpha}{A} + \frac{s_{13}s_{23}e^{i\delta}}{A-1} & c_{23} & s_{23}e^{i\delta} \\ -\frac{c_{12}s_{12}s_{23}\alpha}{A} + \frac{c_{23}s_{13}e^{i\delta}}{A-1} & -s_{23} & c_{23}e^{i\delta} \end{bmatrix} \tag{2.68}$$

For the sake of comparison with the standard parametrization of mixing matrices in the vacuum, we could make a one-to-one correspondence of mixing angles at this order:

$$\begin{aligned}\widetilde{s}_{13} =&\frac{s_{13}}{A-1}\\ \widetilde{s}_{12} =&c_{12}s_{12}\frac{\alpha}{A}\\ \widetilde{s}_{23} =&s_{23}\end{aligned}\tag{2.69}$$

The second-order effective mixing matrix is shown in the appendices. We could obtain the oscillation probabilities using the Eqn.(2.36) in replace of the new mixing matrix and new mass eigenstates.

$$\mathcal{P}_{ee} = 1 - \frac{4c_{12}^2 s_{12}^2 \alpha^2 \sin^2(A\Delta_3)}{A^2} - \frac{4s_{13}^2\sin^2[(1-A)\Delta_3]}{(A-1)^2}\tag{2.70}$$

$$\begin{aligned}\mathcal{P}_{\mu e} =& \frac{4c_{12}^2 c_{23}^2 s_{12}^2 \alpha^2 \sin^2(A\Delta_3)}{A^2} - \frac{8c_{12}c_{23}s_{13}s_{23}s_{12}\alpha\sin(A\Delta_3)\sin[(1-A)\Delta_3)]\cos(\delta+\Delta_3)}{(A-1)A}\\ &+\frac{4s_{13}^2 s_{23}^2\sin^2[(1-A)\Delta_3]}{(A-1)^2}\end{aligned}\tag{2.71}$$

$$\begin{aligned}\mathcal{P}_{\tau e} =& \frac{4c_{12}^2 s_{12}^2 s_{23}^2 \alpha^2 \sin^2(A\Delta_3)}{A^2} + \frac{8c_{12}c_{23}s_{12}s_{23}s_{13}\alpha\sin(A\Delta_3)\sin[(1-A)\Delta_3]\cos(\delta+\Delta_3)}{(A-1)A}\\ &+\frac{4c_{23}^2 s_{13}^2\sin^2[(1-A)\Delta_3]}{(A-1)^2}\end{aligned}\tag{2.72}$$

$$\begin{aligned}\mathcal{P}_{\mu\mu} =& 1 - 4c_{23}^2 s_{23}^2\sin^2(\Delta_3) + 4c_{23}^2 c_{12}^2 s_{23}^2(\alpha\Delta_3)\sin(2\Delta_3) - 4c_{23}^2 c_{12}^4 s_{23}^2\left(\alpha^2\Delta_3^2\right)\cos(2\Delta_3)\\ &-\frac{4c_{23}^2 c_{12}^2 s_{12}^2 s_{23}^2(\alpha^2\Delta_3)\sin(2\Delta_3)}{A} + \frac{4(A\Delta_3)c_{23}^2 s_{13}^2 s_{23}^2\sin(2\Delta_3)}{A-1}\\ &+\frac{2c_{12}^2 c_{23}^2 s_{12}^2\alpha^2\left\{c_{23}^2\cos(2A\Delta_3)+s_{23}^2\cos[2(A-1)\Delta_3]\right\}}{A^2} + \frac{2s_{13}^2 s_{23}^2\left\{c_{23}^2\cos(2A\Delta_3)+s_{23}^2\cos[2(A-1)\Delta_3]\right\}}{(A-1)^2}\\ &+\frac{4c_{12}c_{23}s_{12}s_{13}s_{23}\alpha\cos(\delta)}{(A-1)A}\{c_{23}^2\left[\left(A^2-1\right)-A^2\cos(2\Delta_3)+\cos(2A\Delta_3)\right]\\ &+s_{23}^2\left[-A^2+(A^2-1)\cos(2\Delta_3)+\cos(2(A-1)\Delta_3)\right]\}\end{aligned}\tag{2.73}$$

$$\begin{aligned}\mathcal{P}_{\tau\mu} =& 4c_{23}^2 s_{23}^2\sin^2(\Delta_3) - 4c_{23}^2 s_{23}^2 c_{12}^2(\alpha\Delta_3)\sin(2\Delta_3) + 4c_{23}^2 s_{23}^2 c_{12}^4(\alpha^2\Delta_3^2)\cos(2\Delta_3)\\ &+\frac{4c_{23}^2 s_{23}^2 c_{12}^2 s_{12}^2(\alpha^2\Delta_3)\sin(2\Delta_3)}{A} - \frac{4(A\Delta_3)c_{23}^2 s_{13}^2 s_{23}^2\sin(2\Delta_3)}{A-1}\\ &-\frac{4c_{23}^2 s_{13}^2 s_{23}^2\sin(\Delta_3)\sin[(1-2A)\Delta_3]}{(A-1)^2} + \frac{4c_{12}^2 c_{23}^2 s_{12}^2 s_{23}^2\alpha^2\sin(\Delta_3)\sin[(1-2A)\Delta_3]}{A^2}\\ &+\frac{4c_{12}c_{23}s_{12}s_{13}s_{23}\alpha\sin(\Delta_3)}{(A-1)A}\{c_{23}^2\left[-A^2\sin(\delta+\Delta_3)+\left(A^2-1\right)\sin(\delta-\Delta_3)+\sin((2A-1)\Delta_3+\delta)\right]\\ &+s_{23}^2\left[-A^2\sin(\delta-\Delta_3)+\left(A^2-1\right)\sin(\delta+\Delta_3)+\sin((1-2A)\Delta_3+\delta)\right]\}\end{aligned}\tag{2.74}$$

As for the rest T-conjugate formulae, we can always obtain them by changing the sign of δ. For antineutrinos, the sign of the matter potential should be reversed. In turn, we have

$$\mathcal{P}_{\beta\alpha} = \mathcal{P}_{\alpha\beta}(\delta\to-\delta)\quad \mathcal{P}_{\bar{\alpha}\bar{\beta}} = \mathcal{P}_{\alpha\beta}(A\to-A\,,\delta\to-\delta)\tag{2.75}$$

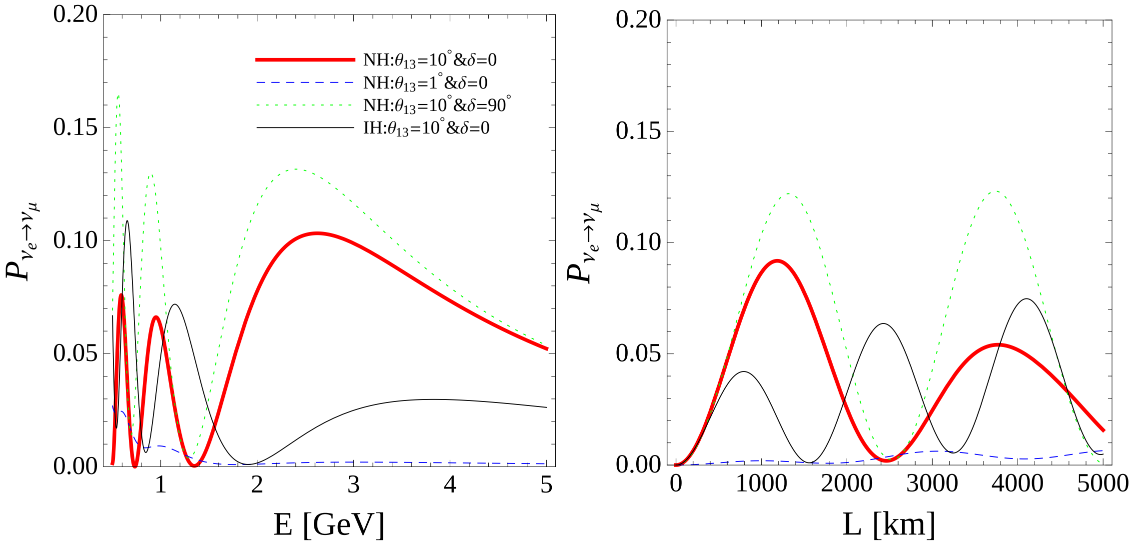

Figure 2.4: *The oscillation probability in a homogeneous matter with a constant density ($\rho = 4.0$ g/cm^3) as a dependence of the mass hierarchy, θ_{13} and $\delta_{\rm CP}$. We assume $L = 1500$ km in the left-hand side and $E = 2$ GeV in the right-hand side. The true oscillation parameters are taken as follows: $\theta_{12} = 34°$, $\theta_{13} = 10°$, $\theta_{23} = 45°$, $\delta_{\rm CP} = 0°$, $\Delta m^2_{21} = 7.6 \times 10^{-5}$ eV^2 and $\Delta m^2_{31} = 2.46 \times 10^{-3}$ eV^2, otherwise expressed by legends.*

In fact, we could use these formulas to predict qualitative behaviors of event rates, propose new experiments by different channels and understand simulation results[¶]. In addition, are the physics arguments changed after we relax one of conditions in the time-independent perturbative expansions in the first method? As usual, we have comments in order:

- Why are there many divergent terms in the formulae if the matter term A goes to zero (return to the vacuum case) or one (at the atmospheric resonance). However, these terms are convergent if we take the limits of $A \to 0$ and $A \to 1$. This can be explained by the cancellation between the eigenvalues and eigenvectors of the effective hamiltonian in matter. It also provides a cross check with the vacuum expansion of oscillation probilities.

- As mentioned at the very beginning, we derive the oscillation probabilities generally with the only assumption $\Delta m^2_{21} \ll \Delta m^2_{31}$ and that θ_{13} is not so large. Apart from these, attention should be paid to the term $\alpha\Delta_3$ at $\mathcal{O}(1)$, which breaks down our expansions. In this case, the solar oscillatory behaviour is involved while the basic assumption is its smallness so that we can ignore it.

- The "golden" channel $\mathcal{P}_{e\mu}$ is sensitive to θ_{13} and δ. As shown in the right panel of Fig. 2.4, we could know that θ_{13} controls the magnitude of the oscillation probability, the mass hierarchy is more obvious in the high energy regime in which matter

---

[¶] It should be noted that the simulation is done without approximations.

resonance is possible and the difference between the CP conserving and violating cases is large in the low energy range. All these features can be read from our approximate probability. The leading order term is governed by the third term with the magnitude controlled by $c_{23}^2 s_{13}^2$. The mass hierarchy sensitivity is provided by the $\mathcal{O}(\alpha)$ term, parts of which changes the sign with Δ_3. In addition, we are required to split the compact format of the second term into CP-even and CP-odd terms in order to analyze the sensitivity of CP violation.

- The disappearance channel $\mathcal{P}_{\mu\mu}$ has the best sensitivity to θ_{23} and is blind to the mass hierarchy. Why is it like this? Because it has the leading dependence of θ_{23} as given in the second term of $\mathcal{P}_{\mu\mu}$. Meanwhile, all terms are proportional to the quadratic terms of Δ_3. This also explains why the atmospheric neutrino experiments sensitive to this channel provide the good constraints on θ_{23} and the absolute value of Δm_{31}^2.
- The "silver" channel $\mathcal{P}_{e\tau}$ is a good compensation to $\mathcal{P}_{e\mu}$, especially when no disappearance channels are involved. Up to the second order, $\mathcal{P}_{e\tau}$ differs from $\mathcal{P}_{e\mu}$ only by a sign of the second term. If both appearance channels are included in an experiment, they could provide a CP-odd term by combinations so that it has a compensating sensitivity to CP violation. However, it is challenging to detect ν_τ and ν_μ simultaneously with the same type of neutrino detectors. For this reason, either a hybrid neutrino detector for ν_τ and ν_μ detections is requested, or two detectors sharing the same L/E might be needed.

2.3 Degeneracies and correlations

Note that we want to pursue unknown problems in the neutrino oscillation experiments: $\Delta m_{31}^2 > 0$ (normal ordering) or $\Delta m_{31}^2 < 0$ (inverted ordering); the value of θ_{13}, and whether there is any CP violation (CPV) in the lepton sector.

As we can see from the previous sections, on one hand, all terms in probabilities are combinations of sine and cosine functions. In mathematics, sine and cosine functions are cyclic and they will have the same value after a certain shift of phase. For example, $\sin x = \sin(\pi - x)$. If they were not treated properly, the fake results denoted by symbols with a "$^-$", such as the fake mixing angle $\bar{\theta}_{13}$, could not be avoided or the complete expressions as follows:

$$P(\bar{\theta}_{13}, \bar{\delta}, |\Delta m_{31}^2|, \theta_{23}) = P(\theta_{13}, \delta, |\Delta m_{31}^2|, \theta_{23}) \tag{2.76}$$

$$P(\bar{\theta}_{13}, \bar{\delta}, -|\Delta m_{31}^2|, \theta_{23}) = P(\theta_{13}, \delta, |\Delta m_{31}^2|, \theta_{23}) \tag{2.77}$$

$$P(\bar{\theta}_{13}, \bar{\delta}, |\Delta m_{31}^2|, \pi/2 - \theta_{23}) = P(\theta_{13}, \delta, |\Delta m_{31}^2|, \theta_{23}) \tag{2.78}$$

$$P(\bar{\theta}_{13}, \bar{\delta}, -|\Delta m_{31}^2|, \pi/2 - \theta_{23}) = P(\theta_{13}, \delta, |\Delta m_{31}^2|, \theta_{23}) \tag{2.79}$$

The first equation (2.76) gives us the so-called intrinsic degeneracy while the second one (2.77) shows the sign degeneracy. The third equation (2.78) provides an octant clone,

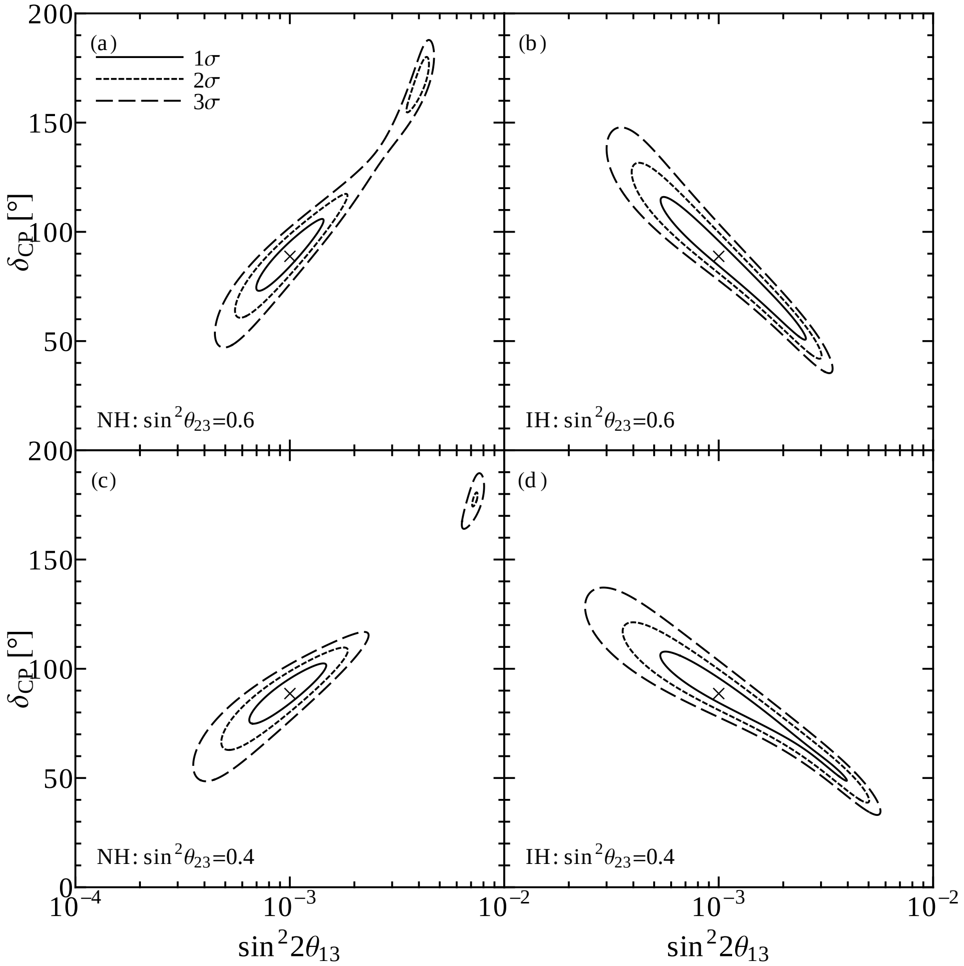

Figure 2.5: *The degeneracy of* θ_{13} *and* δ_{CP} *is shown for different hierarchies (NH: normal hierarchy; IH: inverted hierarchy) and* $\sin^2\theta_{23}$*. The crossed point gives the true values of* $\sin^2 2\theta_{13}$ *and* δ_{CP}*. The experimental configurations are assumed to be the baseline setup in [57]*

since the current experiments constrain θ_{23} around $\pi/4$. The last equation (2.79) involves a mixture of the octant and sign degeneracies. Therefore, eight solutions are allowed to fit the data from experiments. This is also called eight-fold degeneracy, as is well explained in [58]. In experiments, it leads to degeneracy of data fits by different oscillation parameters. In order to make it clear, we show an example of data fits in the degeneracy of $\sin^2 2\theta_{13}$ and δ_{CP} together with $\sin^2 2\theta_{13}$ and $\sin^2\theta_{23}$ in the Fig. 2.5 and Fig. 2.6. As provided in the Fig. 2.5, first of all, the panel (a) has two egg-shape contours and includes a possible clone of $\sin^2 2\theta_{13}$ and δ_{CP}. It points at the degeneracy case of Eqn. (2.76). Second, we can keep the same value of θ_{23} but change the fitted mass hierarchy into the inverted hierarchy, which is given in the panel (b). We could easily identify a change of shape in the direction of the fitted egg. This is exactly what we discuss in the Eqn. (2.77). Finally, the octant degeneracy of $\pi/2 - \theta_{23}$ and θ_{23} is offered in the panels (c) and (d), as they are discussed in the Eqn.(2.78) and Eqn.(2.79). Similary, we plot the degeneracy of $\sin^2 2\theta_{13}$ and $\sin^2\theta_{23}$ in the Fig. 2.6. In order to do the precise measurements, from physics point of view, we have to break these clones.

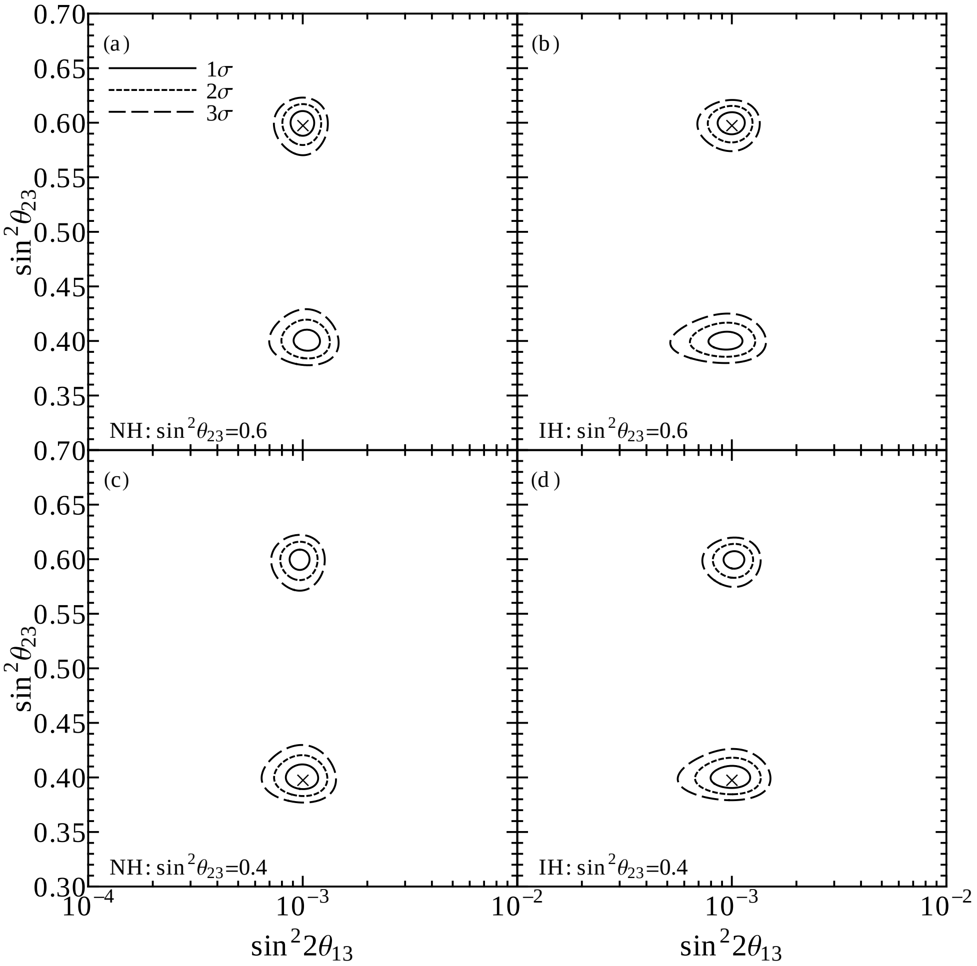

Figure 2.6: *The degeneracy of* $\sin^2 2\theta_{13}$ *and* θ_{23} *is shown for different hierarchies (NH: normal hierarchy; IH: inverted hierarchy). The crossed point gives the true values of* $\sin^2 2\theta_{13}$ *and* $\sin^2\theta_{23}$. *The experimental configurations are assumed to be the baseline setup in [57]*

On the other hand, the combination of different mixing angles including the CP violation phases results in the correlations. A slight shift at one of the coupled mixing angles in a channel will change the precision determination of the other one. As we always measure a mixing angle such as θ_{23} and θ_{12} in the $\mathcal{P}_{\mu\mu}$ at a certain confidence level, it is important to marginalize over the uncertainties from them to avoid a bias during further statistical analysis. The constrained inputs of well measured solar and atmospheric parameters come into the game. Hence more ambiguities are involved in the precision measurements.

In order to illustrate the potential failure in parameter determinations, we plot the correlation and intrinsic degeneracy of θ_{13} and δ_{CP} at the iso-probability plane as an

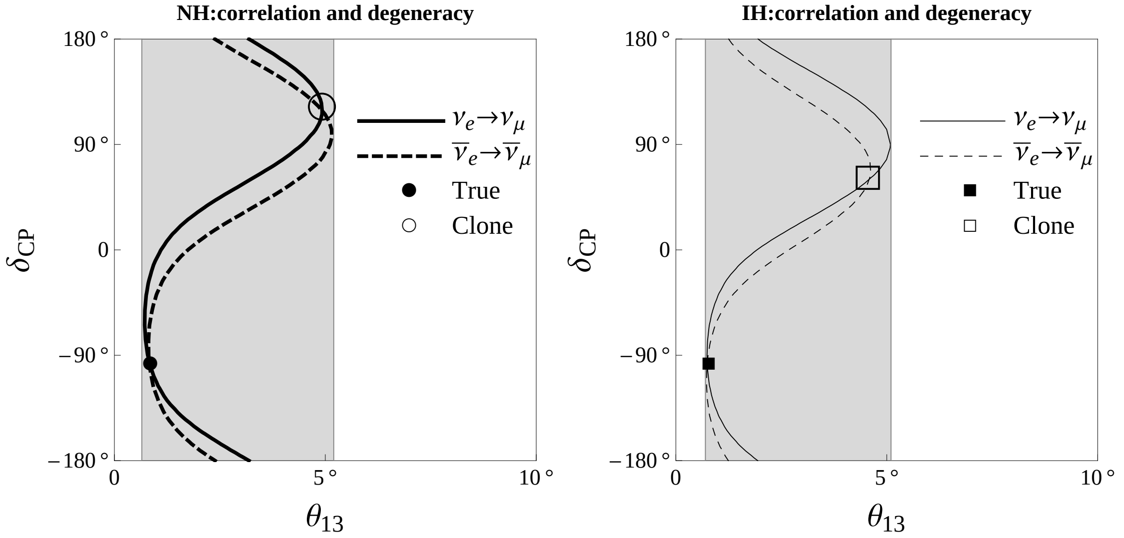

Figure 2.7: *The degeneracy and correlation of* θ_{13} *and* $\delta_{\rm CP}$ *is shown for different hierarchies by iso-probability contours in the figure.*

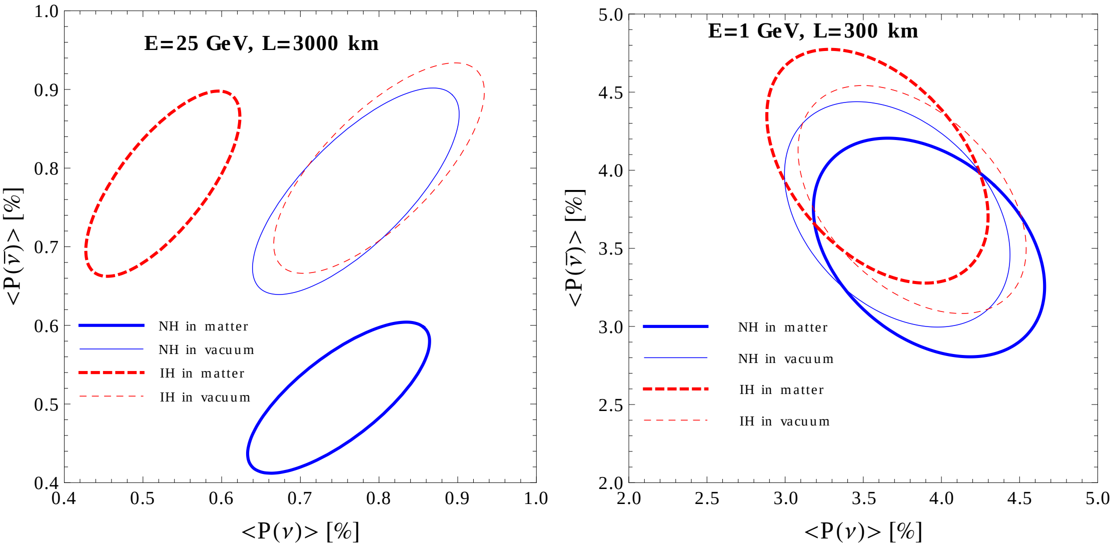

Figure 2.8: *The CP trajectory in the bi-probability with* $\theta_{12} = 34.5°$, $\theta_{13} = 10°$, $\theta_{23} = 45°$, $\Delta m^2_{21} = 7.6 \times 10^{-5}$ eV^2 *and* $\Delta m^2_{31} = 2.46 \times 10^{-3}$ eV^2.

example in Fig. 2.7. Obviously, their continuous dependence provides the correlation of their trigonometric expressions in the probability, which can be understood based on the analytical expansions in the previous section. At first glance, one would make use of neutrino and antineutrino oscillation channels to extract the true values. Indeed we show the case including a combination of $\mathcal{P}_{\nu_e\to\nu_\mu}$ and $\mathcal{P}_{\bar\nu_e\to\bar\nu_\mu}$. However, two cross points are allowed in the same plane, which we call the true and fake values of θ_{13} and $\delta_{\rm CP}$, respectively. It tells us that a degenerate fit is still possible in θ_{13} and $\delta_{\rm CP}$. Meanwhile, we never mention the other complicated situations such as changing the sign of Δm^2_{31} and whether θ_{23} deviates from 45°. Interestingly, we could plot a bi-probability figure as shown in Fig. 2.8 to see how the combination of $\mathcal{P}_{\nu_e\to\nu_\mu}$ and $\mathcal{P}_{\bar{\nu}_e\to\bar{\nu}_\mu}$ evolve in terms of oscillation parameter $\delta_{\rm CP}$. In the vacuum case, we could claim that a deviation from the diagonal line or explicitly a difference between neutrino and antineutrino oscillations would confirm a discovery of CP violation in the lepton sector. However, this connection will be polluted by considering matter effects. As given in Fig. 2.8, a normal hierarchy of neutrino oscillation will lead to the enhancement of $\mathcal{P}_{\nu_e\to\nu_\mu}$. It is the opposite shift for the inverted hierarchy. On one hand, this feature will make the discovery reach of CP violation ambiguous. On the other hand, it provides a clue for a determination of mass hierarchy. With a different L/E or the shape of energy spectra for a fixed baseline experiment, we have a chance to find both CP violations and the mass orderings clearly.

In experiment, we only count event rates and reconstruct the histograms in energy bins. After comparing the histograms from experiments with predictions from neutrino oscillation theory, we hope to answer these questions by statistical confidence level which is expressed by χ^2. Obviously, χ^2 is a function of all the mixing parameters. Even if neutrino oscillations in matter include more complicated terms, the formulas for physics descriptions can still be replaced by the effective mass-squared splittings and effective mixing angles. In principle, the same problem happens in the same way. Finally, we analyse the correlations and degeneracies at the probability level instead of studying the event rates observed in the detectors, but this phenomenon at the probability level represents the most important points. Therefore, more efforts are certainly needed towards this issue. Usually people would make use of either channel combinations, combinations of different experiments in the same channel, different L/E setups or spectra reconstructions to diminish the fake possibilities.

Chapter 3

Status of neutrino oscillation experiments

After we introduce the theoretical discussions of neutrino oscillations, we are well motivated to do experiments to understand such a physics phenomenon. On the one hand, we have to find good neutrino sources and produce the focused neutrino beams. On the other hand, a relatively long distance should allow the initial flavor of neutrinos oscillating into the other flavors or simply count the defict events from the initial flavor of neutrinos. However, neutrinos take part in weak interactions only. In such a situation, it is not a easy task to conduct neutrino detections. We need very large detectors to accumulate enough statistic events and finally extract useful information from the reconstructed events.

3.1 Neutrino sources

Whether we notice it or not, there are weakly interacting neutrinos crossing our bodies and global environment. To make it clear, first of all, let us list different kinds of neutrino sources in nature [59].

- Solar neutrinos:
  There are $2 \times 10^{28} \nu_e$ produced every second in the sun. The neutrino flux at the surface of the earth is approximately given by [60]:

  $$6 \times 10^{10}\ \mathrm{cm}^{-2}\mathrm{s}^{-1}, E \leq 0.42\ \mathrm{MeV};$$
  $$5 \times 10^{6}\ \mathrm{cm}^{-2}\mathrm{s}^{-1}, 0.8\ \mathrm{MeV} \leq E \leq 15\ \mathrm{MeV}.$$

- Reactor neutrinos:
  Nuclear reactor can generate anti-neutrinos by the beta-decay of neutron-rich daughter fragments in the fission. For example, most of contributions come from ^{235}U, ^{238}U, ^{239}Pu and ^{241}Pu in a thermal power plant. It contains the fission processes such as:

  $$^{235}U + \mathrm{n}_{\mathrm{thermal}} \rightarrow ^{236}_{92} U^{*} \rightarrow ^{A_1}_{Z_1} X + ^{A_2}_{Z_2} X + 2\mathrm{n}_{\mathrm{fast}}\,. \tag{3.1}$$

In total, there are more than 500 fission products. Fortunately, we know the highest fission yields are ${}^{94}_{40}\mathrm{Zn}$ and ${}^{140}_{58}\mathrm{Ce}$. Then the total atomic number is 98 while the total nucleon number is 234. The beta decays can be generalized in the following way:

$$ {}^{A}_{z}X \rightarrow^{A}_{z+1} Y + e^{-} + \bar{\nu}_{e} \, . \tag{3.2}$$

To balance the charge of between ${}_{92}U$ and ${}^{94}_{40}\mathrm{Zn}$ plus ${}^{140}_{58}\mathrm{Ce}$, beta decays have to provide 6 electrons and 6 electron antineutrino in each fission process. The energy release of each fission process approximates to 200 MeV. Therefore, a 3 GW plant emits about 10^{21} $\bar{\nu}_e$ per second with the energy around a few MeV and creates a flux of 10^{12} cm^{-2} s^{-1} at 100 m.

- Relic neutrinos:
  Neutrinos left over from the early epoches of the evolution of the universe to date with the number density about 110 cm^{-3} for each species related to a black-body spectrum with the average energy of about 5×10^{-4} eV.

- Geoneutrinos:
  In our earth, there are antineutrinos produced by natural radioactive materials. The luminosity of neutrino flux is around $\sim 6 \times 10^{6}$ cm^{-2} s^{-1} with a number density of $\sim 6 \times 10^{6}$ cm^{-3} and the energy of geoneutrinos is less than MeV.

- Atmospheric neutrinos:
  Around the earth, every day cosmic rays from the universe collide with nucleus in the atmosphere to generate mesons. Later these mesons will immediately decay to neutrinos. Most of the mesons are pions. For example, it is a chain like this $\pi^{+} \rightarrow \mu^{+} + \nu_{\mu}$ and $\mu^{+} \rightarrow e^{+} + \nu_{e} + \bar{\nu}_{\mu}$. The general flux is around $\sim 10^{-1}$ cm^{-2} s^{-1}. The neutrino energy is around $\mathcal{O}(1)$ GeV. For more details of neutrino fluxes, we could refer to [61].

- Accelerator neutrinos:
  According to the current accelerator technology, it is interesting to see that we could prepare a neutrino beam (mainly ν_{μ} or $\bar{\nu}_{\mu}$) with an energy range of 30 MeV $\leq$ E $\leq$ 30 GeV. It depends on the neutrino production mechanism. The heavier the parental materials are, the harder to get high energy neutrinos.

- Supernovae neutrinos:
  These neutrinos come from core-collapse supernovae, which happens rarely in our galaxy. The neutrino energy is a few tens of MeV. It is hardly observed on the earth. An exception is the explosion of Supernovae 1987A, few events of which are observed by water-based detector Kamiokande II [62] and IMB [63] as well as scintillator-based Baksan detector [64].

- High energy cosmic ray neutrinos:
  Their energies are large than a few GeVs. Neutrinos are produced by cosmic rays of the shock wave acceleration after the explosion of the proton-neutron stars.

Why are we so interested in listing the energy range of each neutrino source? This is because the important characteristics of neutrinos and sources of neutrinos that we want to detect affect the design of neutrino detectors. Below we will also learn the lesson from the energy-dependent cross section for neutrino weak interactions.

3.2 Neutrino detections

As we know in the standard model of particle physics, neutrinos can participate both charged-current and neutral-current interactions. For example,

$$\nu_e + e^- \to \nu_e + e^- \,, \tag{3.3}$$

$$\nu_\mu + e^- \to \nu_e + \mu^- \,, \tag{3.4}$$

$$\nu_e + p \quad \to e^- + n \,. \tag{3.5}$$

In the center of mass framework, the cross sections of elastic interactions are proportional to s^2 with $s \equiv (E_{\nu_i} + E_{e^-/p})^2$. Assuming 1 GeV incoming neutrinos, we can estimate the order of magnitude for the cross sections easily. $\sigma \propto \mathrm{G}_\mathrm{F}^2 s \approx 10^{-38}$ cm^2. Now it gives us some clues about the neutrino weak interactions and find the best way to do neutrino detections. Depending on the incoming neutrino energy, it is a tradition to separate the charged-current interactions into the Quasi-Elastic Scatterings (QES), Deep-Inelastic Scatterings (DIS) and Multi-Resonance Scatterings (MRS) in order to signify their different contributions, even though they have overlapped ranges to the total cross section. To have a quantitative impression, we present a list of the rough estimate of the peak for the ν_μ cross sections with free nucleons [65]:

QES The incoming neutrino energy E_ν between $\mathcal{O}(100)$ MeV and $\mathcal{O}(10)$ GeV provides the peak of the factorized cross sections σ/E_ν at $E_\text{peak} \approx 400$ MeV.

MRS The neutrino energy is located between $\mathcal{O}(100)$ MeV and $\mathcal{O}(10)$ GeV but the peak of σ/E_ν is shifted to $E_\text{peak} \approx 1$ GeV.

DIS The neutrino energy is usally counted from $\mathcal{O}(1)$ GeV to $\mathcal{O}(10^3)$ GeV. It becomes relatively flat for σ/E_ν after $E \geq 10^2$ GeV.

Here the typical value of $\sigma/E \approx 10^{-38}$ cm^2 GeV^{-1} matches the pure estimate done before. Neutrino detectors are built to detect particles produced when neutrinos interact with nuclei or the electrons bound to the nuclei. Due to such a small cross section, we demand a large size (or fiducial volume) of the neutrino detectors to accumulate enough event rates. Usually neutrino detectors are homogenous, where either consists of segmented sections with active target elements or contains a whole instrument with active elements. The segmented detector is able to resolve neutrino interactions from multiple sources while the unsgemented one prefers to the unique neutrino source. In addition, the segmented detector can stand on the surface to record events because of its capability of multiple neutrino source detections. It is impossible to select enough signals without good shielding from cosmic-ray incidents for unsegmented detector. This is why such a kind of neutrino detectors are either put underground like the MINOS detector [66] or in the tunnel of a mountain like the OPERA detector [10]. We successfully construct various neutrino detectors: magnetized iron calorimeter in MINOS, the water Cherenkov detector in Super Kamiokande [67] and in IceCube [68], the liquid scintillator detector in Borexino [69], the liquid Argon detector in ICARUS [70] and the emulsion chamber detector [10]. The current neutrino detection technology covers the neutrino energy from $\mathcal{O}(1)$ MeV to $\mathcal{O}(10^9)$ GeV. With these detectors and keeping the neutrino fluxes proportional to $1/L^2$ where L is the distance of the neutrino source and the detector, we can identify the most realistic neutrino sources for oscillation analysis are solar neutrinos, atmospheric neutrinos, accelerator neutrinos and reactor neutrinos compared with the rest types of neutrino sources in the previous section. In fact, neutrino experiments are nothing else but designed to measure neutrino events from the corresponding source types by neutrino detectors so that we can extract information of neutrino oscillations. Indeed, they are carried on in the world to study the properties of neutrinos. Here we only review some neutrino experiments aiming at detections of neutrino oscillation.

3.3 Basics of statistical analysis

What can we learn from observed neutrino oscillation events? It is a statistical comparison of predicted events in theory and observed events in experiment. In the final presentation of results, the fit values always come together with a confidence level. Then we can say neutrino oscillations are allowed at a certain Confidence Level (C.L.). In the previous chapter, we have known a lot about neutrino oscillation probabilities in theory. Here we can extend it to discuss the oscillated event rates in theory. The event rates can be described by the formulae:

$$\frac{dN}{dE} \equiv \frac{d^2N_{in}}{dEdA} \times \sigma \times N_{target} \tag{3.6}$$

With taking into considerations of neutrino oscillations, we have to multiply the appearance probability of each flavor. For example,

$$\frac{dN(\nu_\mu \to \nu_e)}{dE} = \frac{d^2N_{in}}{dEdA} \times \sigma \times N_{target} \times P_{\nu_\mu \to \nu_e}(E) \tag{3.7}$$

When the cross section for a nucleon $\nu_\mu + N \to \mu + X$, it is calculated to be

$$\frac{dN}{dE} = \frac{N_\mu}{L^2[\mathrm{km}^2] \times 10^{10}[\mathrm{cm}^2/\mathrm{km}^2]} \frac{d^2\Phi}{dEd\Omega} \times \sigma[\mathrm{cm}^2] \times M_{\mathrm{det}}[\mathrm{kton}] \times 10^9[\mathrm{g} \cdot \mathrm{kton}^{-1}] \times N_{\mathrm{A}}[\mathrm{g}^{-1}]. \tag{3.8}$$

where $N_{\mathrm{A}} = 6.02 \times 10^{23}[\mathrm{mol}^{-1}]$ is the Avogadro constant. Since a mol of nucleon has one gram mass, N_{A} also means the number of nucleon per mass of the material $[\mathrm{g}^{-1}]$. It should be noted that this is a rough expression. In a simulation of the wrong sign muons by the channel $\mathcal{P}_{\nu_e\to\nu_\mu}$ and counting the same-sign muons in $\mathcal{P}_{\nu_\mu\to\nu_\mu}$ where ν_e and ν_μ are produced by muon decays, the event rates are separated into different parts like this:

$$\frac{dn_i}{dE} = \underbrace{\left[N_{\mu^i} N_{\mathrm{kT}} \epsilon_\mu \, \frac{10^9 N_{\mathrm{A}}}{m_\mu^2 \pi}\right]}_{normalization} \underbrace{\left[\frac{E_\mu}{L^2} \, g_i(E/E_\mu)\sigma_i(E)\right]}_{flux} \underbrace{\left[P_i(E)\right]}_{oscillation} \tag{3.9}$$

where N_{kT} is the fudicial mass of the detector, ϵ_μ is the muon detection efficiency (default value $\epsilon_\mu = 1$), N_{μ^i} is the stored muons and the rest are listed in the following [71]:

$$\sigma_{\nu_\mu}(E) = 0.67 \cdot 10^{-38} E\,\mathrm{cm}^2/\mathrm{GeV}\ , \qquad \sigma_{\bar{\nu}_\mu}(E) = 0.34 \cdot 10^{-38} E\,\mathrm{cm}^2/\mathrm{GeV}\ , \tag{3.10}$$

$$g_{\nu_e}(x) = g_{\bar{\nu}_e}(x) = 12x^2(1-x)\ , \qquad g_{\nu_\mu}(x) = g_{\bar{\nu}_\mu}(x) = 2x^2(3-2x)\ , \tag{3.11}$$

In reality, we would consider the flux spectra including the flux normalization errors and the cross section with its uncertainties. Of course, the oscillation probability depends on the oscillation parameters, neutrino energy and baseline. Meanwhile, a neutrino experiment is sensitive to a certain channel which studies an incomplete list of corresponding oscillation parameters so that other inputs as mixing angles and mass squared differences are taken from the global fit values at a statistical level, we have to include a systematic uncertainty to each of them in addition. For example, a typical reactor neutrino oscillation experiment is sensitive to $\mathcal{P}_{ee}$ driven by θ_{13} and Δm^2_{21} in terms of three-generation neutrino oscillations. If we perform a comparison of observed event rates and predictions, the inputs of Δm^2_{31} and θ_{12} are unavoidable. According to propagations of uncertainties in statistic analysis, the external uncertainties of these inputs which is often named as "priors" should also be taken into account. To make it clear, we can show a binned χ^2 as a function of the related factors with n bins:

$$\chi^2 = \sum_{A=N,F} \sum_{i=1}^{n} \frac{1}{N_i^A}[T_i^A(\theta_{13}\,, \cdots ; a_{\mathrm{norm}}, a^A_{\mathrm{det}}\,, \cdots) - N_i^A]^2 + \frac{a^2_{\mathrm{norm}}}{\sigma^2_{\mathrm{norm}}} + \frac{(a^N_{\mathrm{det}})^2}{\sigma^2_{\mathrm{det}}} + \frac{(a^F_{\mathrm{det}})^2}{\sigma^2_{\mathrm{det}}} + \cdots\ , \tag{3.12}$$

where N_i^N and N_i^F are the observed event rates without any oscillations in the i-th energy bin at the near and far detector, respectively. In addition, T_i^A is the predicted event rates for a certain oscillation channel with systematical errors such as the normalization uncertainty by a_{norm} which is correlated between the near and far detector as well as the uncorrelated detection uncertainties a^N_{det} and a^F_{det}. The dots denote other related factors and their priors which should be included in the data analysis. In this way, it guarantees that the minimal bias is involved in statistics and the uncertainties are propagated correctly. After marginalizations over the nuisance variables, we minimize the χ^2 to describe the sensitivities or constraints of parameters in which we are interested at the confidence levels immediately.

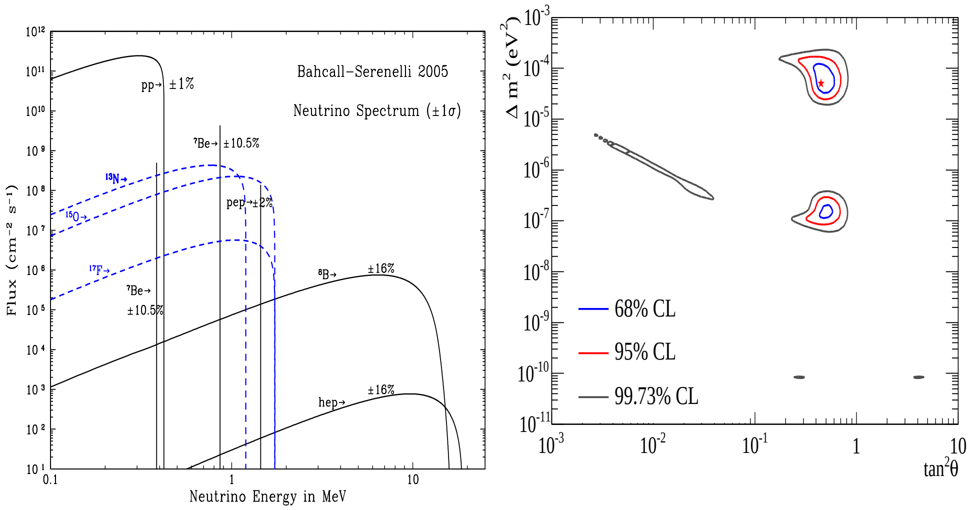

Figure 3.1: *The left panel is neutrino energy spectra in the sun predicted by the Solar Standard Model [72]. In the right panel, SNO neutrino oscillation analysis, including pure* D_2O *phase day and night spectra, and salt extracted CC spectra, NC and ES fluxes, day and night. The star is plotted at the best-fit parameters. This figure is extracted from [73].*

3.4 Current status of experiments

During the past decades, it was full of progress in this field. Neutrino deficits from the Sun have been successfully explained by neutrino oscillations. Meanwhile, solar neutrino experiments has provided a very good measurement of mixing parameters. In addition, neutrino detections from the atmosphere in the Earth also stand as an evidence of neutrino oscillations. In the Olympic games of θ_{13} coverage, there are three on-going reactor neutrino experiments Daya Bay, Double CHOOZ and RENO by the $\bar{\nu}_e$ disappearance channel. Meanwhile, accelerator-driven experiments like T2K will also contribute to them by using the channel of $\nu_\mu \to \nu_e$. Recently there is a piece of exciting news from T2K [8], where they claimed a 2.5σ discovery of non-zero θ_{13}. In addition, the collaboration group at MINOS shows us results which disfavors the zero θ_{13} hypothesis at 89% confidence level [9]. We are looking forward to the on-going reactor neutrino experiments like Double CHOOZ to confirm them. Here comes a short report of different neutrino oscillation experiments. Before we propose new experiments and perform a systematic comparison of physic reaches of them, we have to know what happens so far in neutrino oscillation experiments.

3.4.1 Solar neutrino experiments

A series of solar neutrino experiments include SNO, Homestake, SAGE, GNO, Kamiokande and Super-Kamiokande, Borexino. According to the Standard Solar Model, the energy spectrum of solar neutrino flux in the Earth are presented in Figure 3.1.

SNO experiment, taken as an example, is sensitive to all active neutrino flavors through the charged current and the neutral current on the Deuteron and the elastic scattering reactions on electrons:

$$\begin{aligned} \nu_e + d &\rightarrow e^- + p + p \qquad (\mathrm{CC}) \\ \nu_\alpha + d &\rightarrow \nu_\alpha + p + n \qquad (\mathrm{NC}) \\ \nu_\alpha + e^- &\rightarrow \nu_\alpha + e^- \qquad (\mathrm{ES})\,, \end{aligned}$$

with $\alpha = e, \mu, \tau$. The NC channel has equal sensitivity to all active neutrinos, while the ES channel is sensitive primarily to electron-neutrinos. Hence, the NC measurement can determine the total active solar neutrino flux even if electron-neutrinos transform to another active flavor. In units of 10^6 cm^{-2} s^{-1}, the total flux of active-flavor neutrinos from ^{8}Be decay in the Sun is found to be $4.94^{+0.21}_{-0.21}(\mathrm{stat})^{+0.38}_{-0.34}(\mathrm{syst})$ and the integral flux of electron neutrinos for an undistorted ^{8}Be spectrum is $1.68^{+0.06}_{-0.06}(\mathrm{stat})^{+0.08}_{-0.09}(\mathrm{syst})$; the signal from ($\nu_\alpha$,e) elastic scattering is equivalent to an electron-neutrino flux of $2.35^{+0.22}_{-0.22}(\mathrm{stat})^{+0.15}_{-0.15}(\mathrm{syst})$. These results are consistent with those expected for neutrino oscillations with the so-called Large Mixing Angle parameters, and also with an undistorted spectrum in the Solar Standard Model [73]. Results based on two neutrino oscillations are depicted in the right side of Fig. 3.1.

3.4.2 Atmospheric neutrino experiments

Atmospheric neutrinos are produced in the atmosphere as the primary cosmic rays, typically protons, collide with the air nuclei. The collision creates a shower of hadrons, most of which are pions. Then one pion decays to a muon and a muon-neutrino which subsequently decays to an electron, a muon-neutrino and an electron-neutrino:

$$\begin{aligned} \pi^-(\pi^+) \quad &\longrightarrow \quad \bar{\nu}_\mu(\nu_\mu) + \mu^-(\mu^+) \\ &\qquad\qquad \mu^-(\mu^+) \rightarrow e^-(e^+) + \nu_\mu(\bar{\nu}_\mu) + \bar{\nu}_e(\nu_e) \end{aligned} \tag{3.13}$$

Therefore, the initial atmospheric neutrino flux consists of ν_e, $\bar{\nu}_e$, ν_μ and $\bar{\nu}_\mu$ with a ratio of $\Phi = \frac{\nu_\mu + \bar{\nu}_\mu}{\nu_e + \bar{\nu}_e} \simeq 2$. The ratio $\mathbf{R} \equiv (\mu/e)_{\mathrm{DATA}}/(\mu/e)_{\mathrm{MC}}$ has been measured to study the atmospheric neutrino flavor ratio Φ, where the ratio of data to Monte Carlo is taken into account for both the neutrino flux and cross sections within this scheme. It should be noted that this case holds true actually only at relatively small energies less than a few GeV; otherwise there is no time for the high-energy muons to decay in the atmosphere and they are stopped in the earth instead. In calculations one has to notice that other particles such as kaons are also produced in hadronic showers. Besides, solar neutrinos can contribute to parts of total neutrino events which should be subtracted from data. Anyway, if the final neutrinos are different from their initial flavors before arriving at the earth, there must be deficits or said deviation from flux ratio 2 in atmospheric neutrinos after removing all contaminations. In other words, the expected value for $\mathbf{R}$ is unity if there is agreement between the experiment and the theoretical prediction. The small

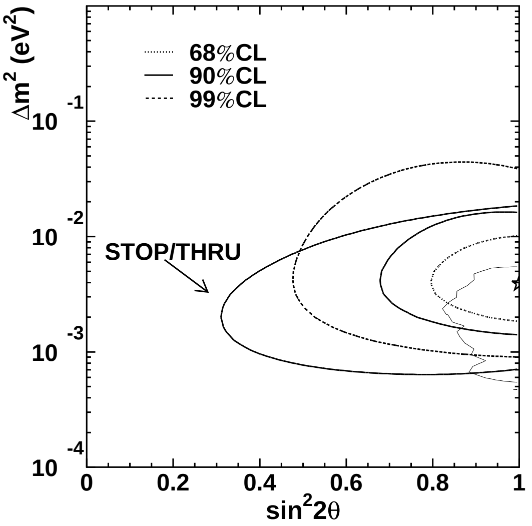

Figure 3.2: *The allowed region contours at 68% (dotted contour), 90% (thick solid), and 99% (dashed) C.L. obtained by the combined analysis of Super-K upward stopping and through-going muons drawn on the (*$\sin^2 2\theta$*,*Δm^2*) plane for* $\nu_\mu \leftrightarrow \nu_\tau$ *oscillations. The star indicates the best fit point at* $(\sin^2 2\theta, \Delta m^2) = (1.0, 3.9 \times 10^{-3}\text{eV}^2)$ *in the physical region. The allowed region contour indicated by solid thick labelled line with "STOP/THRU" is made based on the Super-K stopping/through-going muon ratio alone at 90% C.L. Plot is taken from ref. [67].*

value of the ratio and the zenith angle dependence suggest that neutrino oscillations may be responsible for these results.

The most compelling evidence for atmospheric neutrino deficits comes from the measurements at Super-Kamiokande experiment [67] since 1998. They first announced the strong evidence for ν_μ oscillations. The ratio **R** was measured to be $0.61 \pm 0.03(stat.) \pm 0.05(sys.)$ and smaller than expected from theoretical models of atmospheric neutrino production. Figure 3.2 offers the results of data analysis based on neutrino oscillation.

3.4.3 Accelerator and reactor neutrino experiments

In addition to the experiments measuring solar and atmospheric neutrinos, there are several terrestrial laboratory experiments for neutrino oscillation study in which neutrinos are produced either in accelerators or in nuclear reactors. These experiments have the advantage of better control of the neutrino flux compared with the solar and atmospheric neutrinos and therefore they will play an essential role in precision determination of neutrino oscillation parameters.

Oscillation experiments can be divided into two groups based on how they look for the neutrino oscillation signals. In a disappearance experiment one looks for attenuation of neutrino beam composed of a certain neutrino flavor and in an appearance experiment one

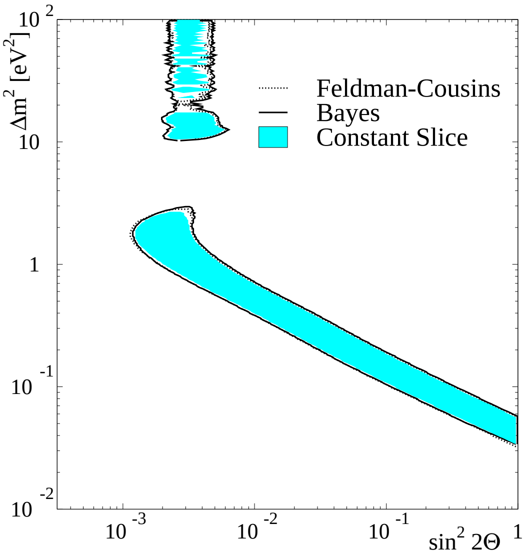

Figure 3.3: *Favored regions in the* $(\sin^2 2\theta, \Delta m^2)$ *plane at* 90% *CL. The Feldman-Cousins, Bayesian, and constant-slice methods all give about the same result [11].*

looks for appearance of neutrinos of different flavor not presented in the beam initially.

In the following a short description of some of the most important accelerator and reactor experiments is given.

Short-baseline accelerator experiments

The only appearance laboratory experiment that has been a positive oscillation signal is the LSND experiment. It claimed its first evidence for $\bar{\nu}_\mu \rightarrow \bar{\nu}_e$ oscillation in 1995.

Neutrinos in the LSND experiment are produced with an intense 800 MeV proton beam. The beam hits the target and creates positive pions which decay mainly at rest to a muon and a muon-neutrino that subsequently decays to an electron, a muon-neutrino and an electron-neutrino as described in (3.13). The experiment investigates whether the resulting $\bar{\nu}_\mu$ whether oscillate into $\bar{\nu}_e$ detected about 30 m away from the neutrino source. As the final result, LSND collaboration has reported that an oscillation probability of $(0.264 \pm 0.067 \pm 0.045)\%$ is observed, corresponding to $0.2 - 10$ eV^2/c^4 Δm^2 range which is greater than that of other experiments. The data analysis based on neutrino oscillation is presented in Figure 3.3.

Long-baseline accelerator experiments

The KEK to Kamioka(K2K) is the first working accelerator long-baseline experiment. Neutrino beam is produced by a 12 GeV proton beam from the synchrotron accelerator at the High Energy Accelerator research Organization(KEK) and detected by the Super-K detector, 250 km away from the KEK. The Δm^2_{31} region at $\sin^2 2\theta_{23}$ is between 1.9 and 3.5×10^{-3} eV^2 at the 90 % C.L. with a best-fit value of 2.8×10^{-3} eV^2 [74]. Data

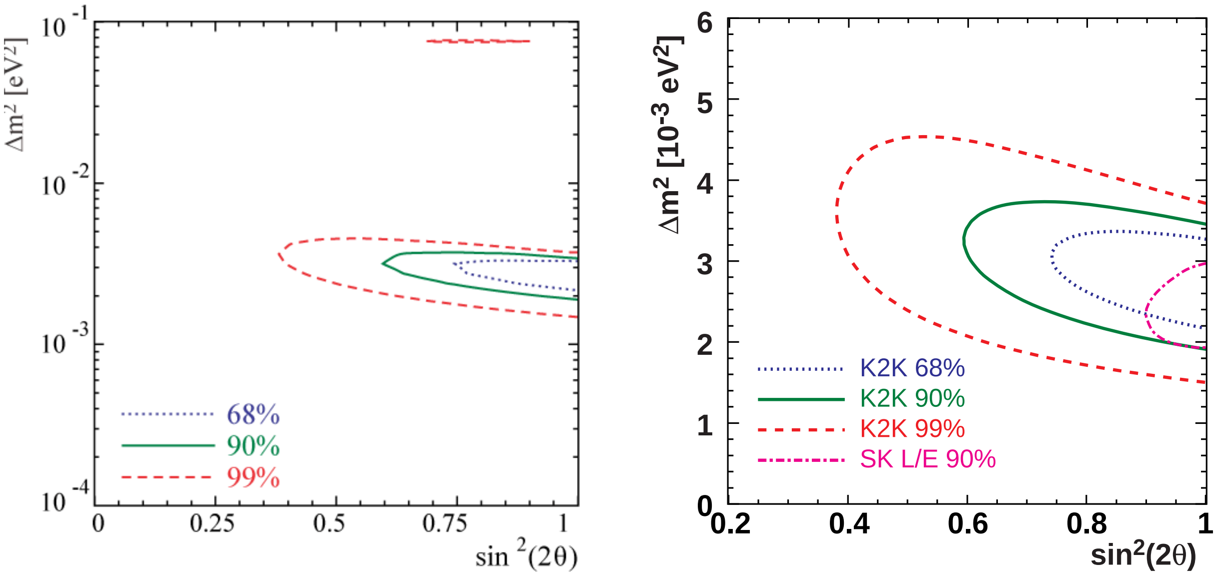

Figure 3.4: *The left plot is the full data analysis in K2K experiment only. The right one is the comparison of between K2K results and the SK atmospheric neutrino measurements [67]. Dotted, solid, dashed and dash-dotted lines represent 68%, 90%, 99% C.L. allowed regions of K2K and 90% C.L. allowed region from SK atmospheric neutrino, respectively [74].*

Analysis based on neutrino oscillation in Figure K2K only and its comparison with Super-K experiment is given in Figure 3.4.

Reactor disappearance experiments

The CHOOZ experiment looked for disapearance of $\bar{\nu}_e \longrightarrow \bar{\nu}_x$ oscillations. Electron antineutrinos with a mean energy of a few MeV are produced in two nuclear reactors at the power station and detected about 1 km away from the neutrino source via the inverse beta decay reaction. Due to its relatively long baseline, the experiment was sensitive to Δm^2 value down to atmospheric neutrino range.

The CHOOZ experiments found no evidence of neutrino oscillations for the parameters region $\Delta m^2 \geq 7 \times 10^{-4} eV^2$ at maximal mixing and $\sin^2 2\theta > 0.1$ at a 90% confidence level. The excluded region is shown in Figure 3.5. As already mentioned, the CHOOZ results rule out the possibility of $\nu_\mu \longrightarrow \nu_e$ oscillation to explain the atmospheric neutrino problem.

The other latest reactor disappearance experiment is KamLAND with the longest baseline about 180 km. The methods of production and detection are similar to CHOOZ. Due to the long baseline, KamLAND can be sensitive to small Δm^2 values up to a solar model independent test for the Large Mixing Angle(LMA) solution of solar neutrino problem. According to their results [75], the ratio of the number of observed events to the expected number of events in the absence of neutrino oscillations is $0.601 \pm 0.069(\text{stat}) \pm 0.042(\text{syst})$ for neutrino energy above 2.6 MeV. This rules out the no-oscillation hypothesis at 99.6%

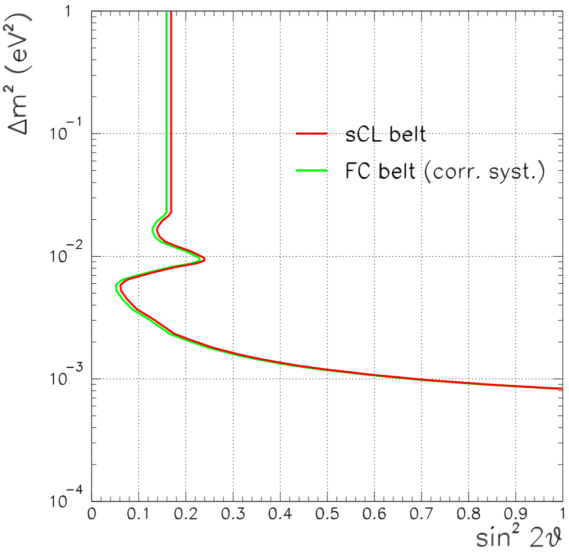

Figure 3.5: *The excluded region of* $(\sin^2 2\theta, \Delta m^2)$ *at 90% C.L in CHOOZ. "sCL" in red line makes use of the spectrum information while the "FC belt" in green line considers the correct systematic treatments. This figure is taken from [6].*

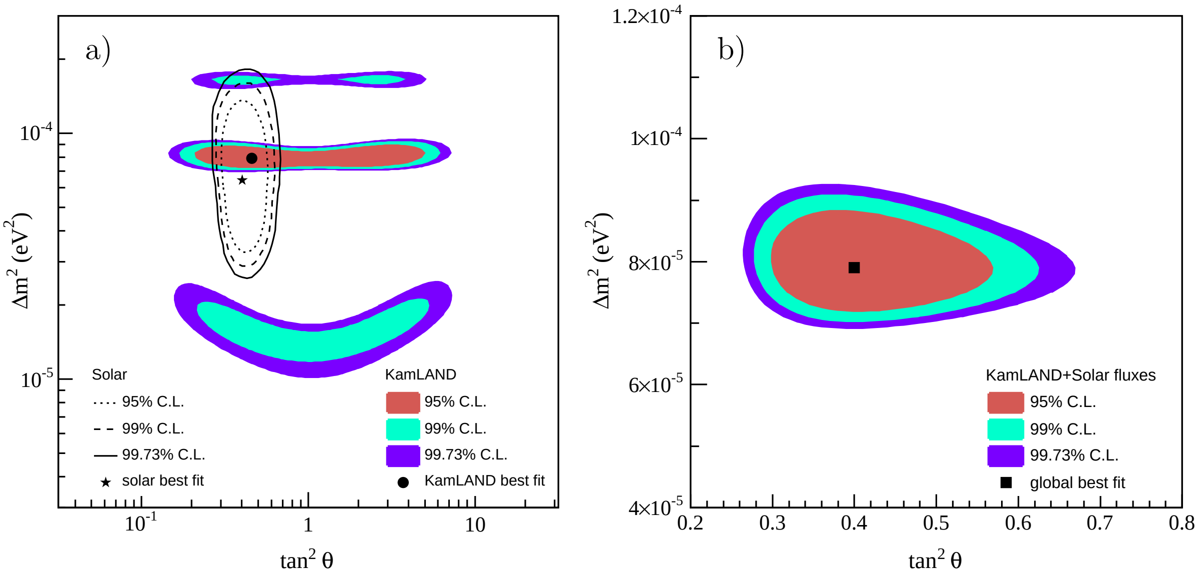

Figure 3.6: *(a) Neutrino oscillation parameter allowed region from KamLAND anti-neutrino data (shaded regions) and solar neutrino experiments (lines). (b) Result of a combined two-neutrino oscillation analysis of KamLAND and the observed solar neutrino fluxes. The plot is extracted from [75].*

C.L. and prefers the distortion expected from $\overline{\nu}_e$ oscillation effects. A two-neutrino oscillation analysis of the KamLAND data gives $\Delta m^2 = 7.9^{+0.6}_{-0.5}\times10^{-5}\,\mathrm{eV}^2$. A global analysis of data from KamLAND and solar neutrino experiments in Figure 3.6 yields $\Delta m^2 = 7.9^{+0.6}_{-0.5}\times10^{-5}\,\mathrm{eV}^2$ and $\tan^2\theta = 0.40^{+0.10}_{-0.07}$, the most precise determination to date.

parameter	best fit	2σ	3σ
Δm^2_{21} [10^{-5}eV^2]	7.59	7.24–7.99	7.09–8.19
Δm^2_{31} [10^{-3}eV^2]	2.5	2.25–2.68	2.14–2.76
$\sin^2\theta_{12}$	0.312	0.28–0.35	0.27–0.36
$\sin^2\theta_{23}$	0.52	0.41–0.61	0.39–0.64
$\sin^2\theta_{13}$	0.013	0.004–0.028	0.001–0.035

Table 3.1: *Best-fit values, 2σ and 3σ intervals (1 d.o.f.) for the three–flavor neutrino oscillation parameters from global data including solar, atmospheric, reactor (KamLAND and CHOOZ) and accelerator (T2K and MINOS) experiments [77].*

3.4.4 Global results from 3-neutrino analysis

To make use of all existing experimental bounds in the new model, it is necessary to take correlations of them into accounts by global analysis. Under the assumption of three neutrino mixing and based on the conventions $\Delta m^2_{\mathrm{SOL}} \equiv \Delta m^2_{21} \equiv m^2_2 - m^2_1$, $\Delta m^2_{\mathrm{ATM}} \equiv \Delta m^2_{31} \equiv m^2_3 - m^2_1$, $\theta_{12} \equiv \theta_{\mathrm{SOL}}$ and $\theta_{23} \equiv \theta_{\mathrm{ATM}}$, results about Best-fit values 2σ and 3σ intervals (1 d.o.f.) for the neutrino oscillation parameters are presented in the table 3.1 by [76]. The PMNS mixing matrix [55] is defined as the following:

$$U = \begin{pmatrix} c_{13}c_{12} & s_{12}c_{13} & s_{13} \\ -s_{12}c_{23} - s_{23}s_{13}c_{12} & c_{23}c_{12} - s_{23}s_{13}s_{12} & s_{23}c_{13} \\ s_{23}s_{12} - s_{13}c_{23}c_{12} & -s_{23}c_{12} - s_{13}s_{12}c_{23} & c_{23}c_{13} \end{pmatrix}, \tag{3.14}$$

with $c_{ij} \equiv \cos\theta_{ij}$ and $s_{ij} \equiv \sin\theta_{ij}$ and without considerations of CP violation.

3.5 Progress of future's accelerator neutrino experiments

Due to these unknown oscillation parameters, the next generation neutrino experiments are proposed. Nevertheless, a good discovery reach of non-conserving δ_{CP} is still far out of reach even when θ_{13} is large enough. Neither does they can perform a good precision measurement of mass hierarchy if $\sin^2 2\theta_{13} \leq 10^{-2}$. As we understand from the theoretical discriptions of neutrino oscillations in matter, a good measurement of mass ordering needs large matter effects in a high energy neutrino source. In addition, the form of L/E in the oscillation probability asks for a match of a long baseline. From this point of view, a further step to conduct a good discovery reach of CP violation, mass hierarchy and θ_{13} requests an exsitence of neutrino factory with better precisions. Originally, two neutrino sources are suggested. One is β decays of the radioactive ions and the other is three-body decays of pure muons. Of course, both of them should be accelerated into a high enough beam energy.

Ion	τ (s)	E_0 (MeV)	f	Decay fraction	Beam
$^{18}_{10}$Ne	2.41	3.92	820.37	92.1%	ν_e
$^{6}_{2}$He	1.17	4.02	934.53	100%	$\bar{\nu}_e$
$^{8}_{5}$B	1.11	14.43	600872.07	100%	ν_e
$^{8}_{3}$Li	1.20	13.47	425355.16	100%	$\bar{\nu}_e$

Table 3.2: Beta decay parameters: lifetime τ, electron total end-point energy E_0, f-value and decay fraction for various ions [79].

3.5.1 Superbeam experiments

Up to now, all the traditional accelerator neutrino experiments adopt the charged pion decays to produce neutrino wide-band beams. For example, a proposal LBNE [78] in US is actively discussed. They accelerate protons to a relatively high energy. Then protons collide with a target, for instance carbon in MINOS, and generate a large numbe of charged pions. If necessary, we can select by magnetic field charged pions according to their curve routines. After these pions pass through a focusing horn and further acceleartions in the storage rings, intense neutrino beams will be obtained by pion decays. The whole chain can be described by the following:

$$\begin{aligned}
\pi^+ &\rightarrow \quad \mu^+ + \nu_\mu \\
\pi^- &\rightarrow \quad \mu^- + \bar{\nu}_\mu \\
\mu^+ &\rightarrow \quad e^+ + \nu_e + \bar{\nu}_\mu \\
\mu^- &\rightarrow \quad e^- + \bar{\nu}_e + \nu_\mu \,.
\end{aligned}$$

It is worth noticing that the intrisic electron type neutrinos will be produced simultaneously. If we assume the parental decay particles of π^+ and one would expect observing the ν_μ disappearance channel in neutrino oscillations, the intrisic ν_e coming from μ^+ decays as by-products will oscillate into ν_μ so that they will create charge-current backgrounds. Since the intrinsic pollutions are large only at the forward direction, people develope the off-axis beam to suppress this type of CC backgrounds at a price of flux drops. NOvA is one of the examples. It is quite sophisticated now to use this superbeam technology. However, statistics are constrained in a comparison with the pure neutrino beam by nucleu beta decays or muon decays.

3.5.2 Beta beam experiments

Two different types of production schemes provide electron neutrinos (anti-neutrinos). One is assumed to originate from beta decays of ^{18}Ne (for ν_e) and ^{6}He (for $\bar{\nu}_e$). The second scheme make good use of beta decays of ^{8}B (for ν_e) and ^{8}Li (for $\bar{\nu}_e$). For the details of their beta decay parameters, take a look at Tab. 3.2. Both should certainly be accelerated and transferred into a storage ring in an experiment. It is usually assumed with the same relativistic booster γ but not necessarily. Currently discussed configurations of a beta beam produce a neutrino beam by beta decays of the following proposed isotopes:

$$\begin{aligned} {}^{18}_{10}\mathrm{Ne} &\rightarrow {}^{18}_{9}\mathrm{F} + e^{+} + \nu_e\,, && (3.15)\\ {}^{6}_{4}\mathrm{He} &\rightarrow {}^{6}_{3}\mathrm{Li} + e^{-} + \bar{\nu}_e\,, && (3.16)\\ {}^{8}_{5}\mathrm{B} &\rightarrow {}^{8}_{4}\mathrm{Be} + e^{+} + \nu_e && (3.17)\\ {}^{8}_{3}\mathrm{Li} &\rightarrow {}^{8}_{4}\mathrm{Be} + e^{-} + \bar{\nu}_e\,, && (3.18) \end{aligned}$$

The oscillation channels of interest are:

$$\begin{aligned} \nu_\mu \text{ appearance: } \nu_e \rightarrow \nu_\mu \text{ for } {}^{18}\mathrm{Ne} \text{ or } {}^{8}\mathrm{B} \text{ stored}\,, && (3.19)\\ \bar{\nu}_\mu \text{ appearance: } \bar{\nu}_e \rightarrow \bar{\nu}_\mu \text{ for } {}^{18}\mathrm{He} \text{ or } {}^{8}\mathrm{Li} \text{ stored}\,. && (3.20) \end{aligned}$$

Since the beam is flavor-clean, there are no special requirements to the detector, other than ν_μ ($\bar{\nu}_\mu$) flavor identification. The chosen detector technology for a beta beam typically depends on the neutrino energies: whereas below 1 GeV a good separation between the quasi-elastic event from electron and muon neutrinos and an efficient background reduction can be reached in a water Cherenkov detector, a (possibly magnetized) iron calorimeter can better identify muon tracks at energies above 1 GeV.

3.5.3 Neutrino factory experiments

The neutrino factory beam comes from muon decays (muon energy E_μ) in straight sections of a storage ring. Depending on the parent muon, the decay will lead to

$$\begin{aligned} + &: \mu^{-} \rightarrow e^{-} + \bar{\nu}_e + \nu_\mu && (3.21)\\ - &: \mu^{+} \rightarrow e^{+} + \nu_e + \bar{\nu}_\mu && (3.22) \end{aligned}$$

The following oscillation signal channels are used:

$$\begin{aligned} \nu_\mu \text{ appearance: } &\nu_e \rightarrow \nu_\mu \text{ for } \mu^{+} \text{ stored}\,, && (3.23)\\ \bar{\nu}_\mu \text{ appearance: } &\bar{\nu}_e \rightarrow \bar{\nu}_\mu \text{ for } \mu^{-} \text{ stored}\,, && (3.24)\\ \nu_\mu \text{ disappearance: } &\nu_\mu \rightarrow \nu_\mu \text{ for } \mu^{-} \text{ stored}\,, && (3.25)\\ \bar{\nu}_\mu \text{ disappearance: } &\bar{\nu}_\mu \rightarrow \bar{\nu}_\mu \text{ for } \mu^{+} \text{ stored}\,. && (3.26) \end{aligned}$$

For the backgrounds, neutral currents are included for all channels, and mis-identified charged current events are included for the appearance channels. Since there are two racetrack-shaped storage rings targeted towards two far detectors, there are altogether eight oscillation channels. Since the neutrino factory proposal is the main concern in the thesis, we will pay a little more attention to it in the next chapter.

Chapter 4

Current design study of a neutrino factory

The concept of a neutrino factory is to accelerate muons which will later decay in the straight storage ring to produce high energy neutrinos by the processes:

$$\mu^+ \to e^+ + \nu_e + \bar{\nu}_\mu\,, \quad \mu^- \to e^- + \bar{\nu}_e + \nu_\mu \tag{4.1}$$

The layout of the accelerator complex at the neutrino factory is shown in Fig. 4.1. Muon beams are produced from the decays of pions which come from the collision of a target by a high-energy proton beam, as is shown by the proton driver in the figure. The driver might be implemented by the developing infrastructure at the current accelerator laboratories (CERN, FNAL and RAL). The target is chosen as a liquid mercury jet which avoids the structural damage from the beam. Further, the pion beam will have a long channel to decay into muons. Due to the fact of three-body decays, the resulting muon beam is largely spreaded. Therefore, a sequence of radio-frequency cavities should be used to turn the distribution of muons into bunches with almost the same energy. It is followed by the phase rotation, ionization cooling processes to reduce the transverse emittance of bunches. Finally, the almost uniformly energetic muon beam with a rather forward momentum will be pumped into the linac system for accelerations. Later neutrinos are produced from the straight section of race-shape storage ring. The number of storage rings depends on how many detectors or baselines we use for neutrino oscillation detections.

Neutrinos travel through a long distance with a phenomenon of flavor oscillations as we described in the previous chapter. A detector with charge identifications could observe opposite-sign muons the charge of which is different from the neutrino source. It is then an ideal place to discover Dirac-type CP violation phase, the hierarchy of mass orderings and the high precision measurements of θ_{13}. The design of a neutrino factory has already been put forward and discussed in international studies, such as in Refs. [16–18]. Especially the most recent study, the International Neutrino Factory and Superbeam Scoping Study [18–20], has laid the foundations for the currently ongoing Design Study for the Neutrino Factory (IDS-NF) [21]. This initiative from about 2007 to 2012 is aiming to present a design report, schedule, cost estimate, and risk assessment for a neutrino factory. It defines a baseline setup of a high energy neutrino factory with two baselines $L_1 \simeq 4\,000\,\mathrm{km}$ and $L_2 \simeq 7\,500\,\mathrm{km}$ (the "magic" baseline) operated by two racetrack-shaped storage rings, where the muon energy is 25 GeV (for optimization questions, see Refs. [28, 29]).

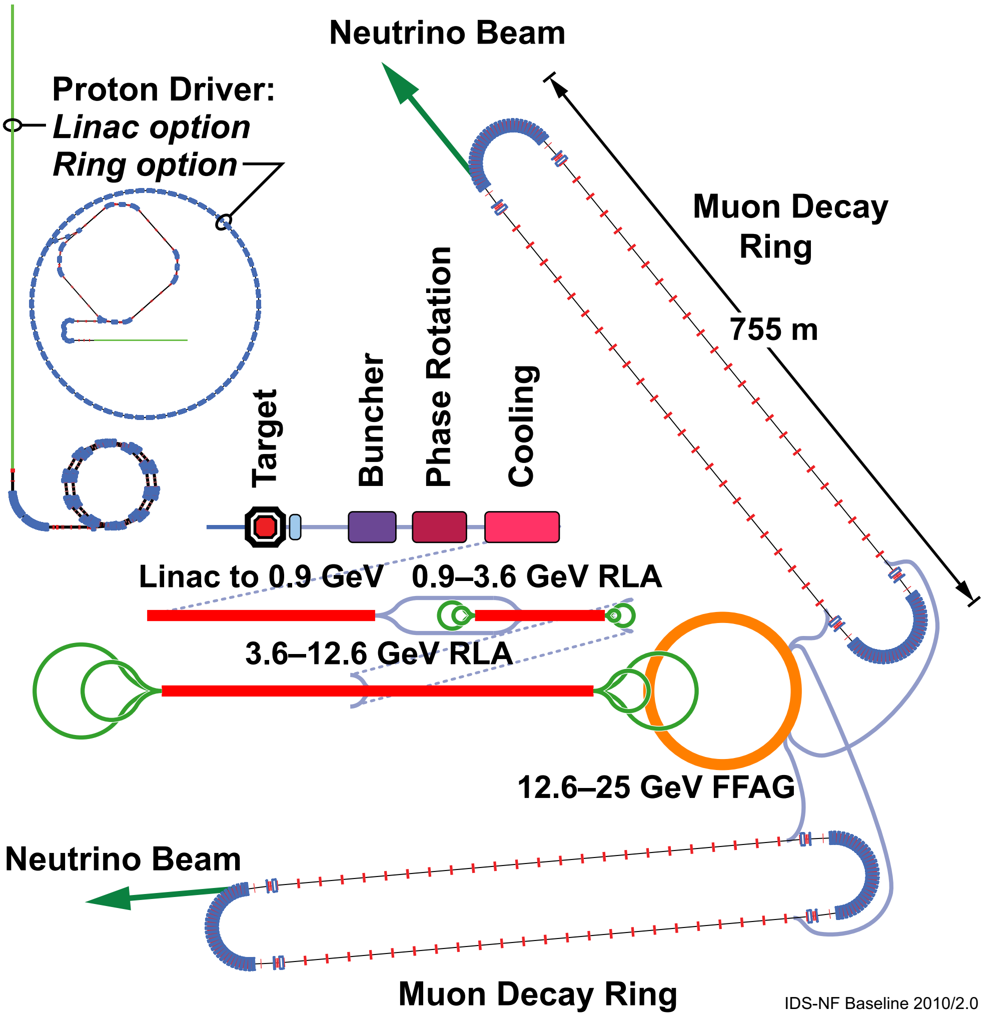

Figure 4.1: *The design of accelerator complex for the neutrino factory. The plot is taken from [21].*

If the neutrino sources come from pure muon decays, both appearance and disappearance channels for neutrinos and antineutrinos are involved. We have to take good charge identifications to reconstruct the oscillation patterns. The Magnetized Iron Detector (MIND) is among the best options. MIND is a MINOS-like iron-scintillator sandwich calorimeter with a sampling fraction optimized for the neutrino factory beam. The schematic layout of MIND is shown in left-hand side of Fig. 4.1. The $1T$ dipole magnetic field is employed for charge identifications. The planes of scintillator and layers of iron are stacked until the ideal fiducial mass is reached. Recently, there is a release of migration matrix relating the neutrino detecting efficiencis to the reconstruced neutrino energy in each bin in detector simulations. It certainly accelerates the progress of the final decision of detector selections. We will take them into considerations at this issue in physics performance discussions.

Apart from that, a low energy neutrino factory (LENF) with $E_\mu \simeq 4\,\text{GeV}$ to $5\,\text{GeV}$ [45–48] has been proposed as an alternative to the high energy neutrino factory (HENF) with a beam energy of 25 GeV. One of the purposes of this alternative has been the reduction of accelerator cost in the case of large θ_{13}. A second aim is to achieve a good discovery reach of CP violations. While the high energy neutrino factory relies on the MIND, the low energy neutrino factory has been proposed with a magnetized Totally Active Scintillator Detector (TASD), which allows for a lower threshold, better energy resolution, and (possibly) electron charge identification, which is required for the so-called "platinum" ($\nu_\mu \rightarrow \nu_e$ and $\bar{\nu}_\mu \rightarrow \bar{\nu}_e$) channels. These channels are the T-inverted channels of the muon neutrino appearance channels. Because of the same matter effects in the $\nu_\mu \rightarrow \nu_e$ and $\nu_e \rightarrow \nu_\mu$ (or $\bar{\nu}_\mu \rightarrow \bar{\nu}_e$ and $\bar{\nu}_e \rightarrow \bar{\nu}_\mu$) channels, CP violation can, in principle, be extracted without convolution with the matter effects.* For the LENF, the useful number of muon decays may be increased by about 40% by an optimization of the neutrino factory frontend for low energies [48]. The schematic desigh of TASD detector is shown in the right-hand side of Fig. 4.2.

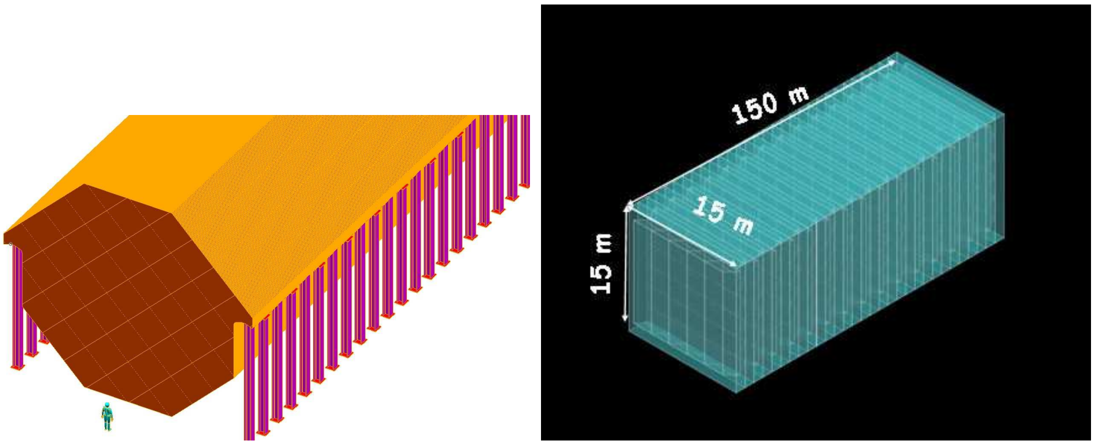

Figure 4.2: *The schematic design of MIND in the left and TASD detectors in the right side for the neutrino factory. The plot is taken from [21].*

In terms of MIND, on one hand, the detector description of this setup is based on [19], which has been updated in [80, 81]. We implement the latest migration matrices (see ref. [81] for details), mapping the incident to the reconstructed neutrino energies for all individual signal and background channels, into later's simulations. Note that charge mis-identification, (electron) flavor mis-identification and neutral current backgrounds are included. For the binning, we then follow [80, 81], where the migration matrices for the appearance channels are given. For the disappearance channels, we assume they share the

---

*In the CP-conjugate channel, the matter effects are different, which means that the fundamental CP violation has to be disentangled from the Earth matter effects, which violate CP extrinsically (Earth matter does not contain any antimatter); see, *e.g.*, Ref. [56].

same matrices with appearance channels. In addition, we have to increase the number of sampling points for high energies to avoid aliasing. it must be possible to hypothesize the signal uncertainties at the level of 2.5% and the background uncertainties at the level of 20%, where they are uncorrelated among all oscillation channels. For the two racetrack-shaped storage rings pointing towards these detectors, we set up the inputs of a luminosity of 2.5×10^{20} useful muon decays per polarity, decay straight, and year, *i.e.*, 10^{21} useful muon decays per year with the running time of 10 years, *i.e.*, 10^{22} useful muon decay in total.

On the other hand, there is also a second type of detector the magnetized Totally Actively liquid Scitillator Detector (TASD). We also consider TASD in the neutrino factory. We assume a 25 kt fiducial mass of TASD with a threshold of 1 GeV and a 94% flat detection efficiency with the energy resolution $\sigma = 10\% \times \sqrt{E/\text{GeV}}$ for muon and antimuon detections. Only neutral current background has to be included but has a suppression factor of 10^{-3}. Without mentioning them directly, we use the beam energy $E = 5$ GeV and the baseline $L = 2540$ km. In addition, we assume the positive polarity of muons in the storage ring with the luminosity of 5×10^{21} useful muon decays per year. By default, 2.5 running years are considered. Finally, we consider 2.5% normalization errors for signals and 0.01% calibration errors for backgrounds.

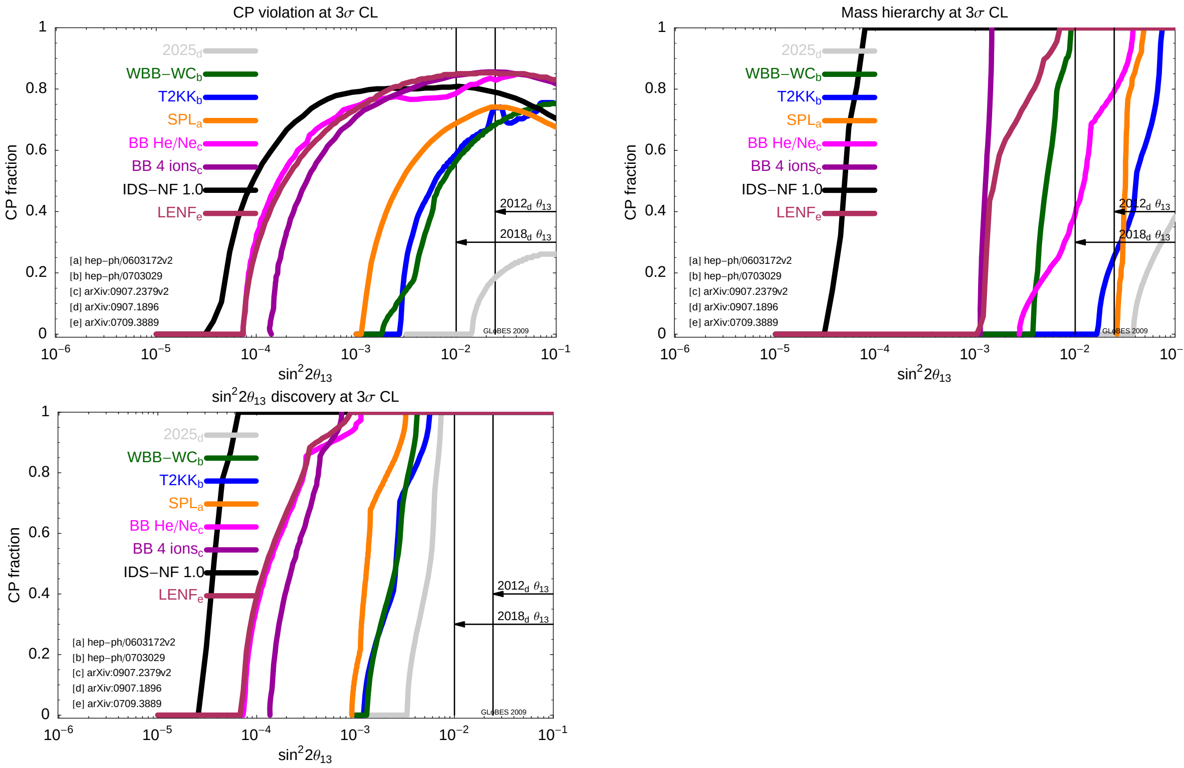

Figure 4.3: *A comparison of the discovery reach of CP violation, mass hierarchy and* θ_{13} *for different proposals of neutrino oscillation experiments. The plot is taken from [82].*

To quantify how to answer the aforementioned questions, we define the following physics performance indicators:

- The establishment of CP violation (**CPV**):
  the hypothesis with CP conserved angles like $\delta_{\rm CP} = 0$ and $\delta_{\rm CP} = \pi$ should be excluded at a given confidence level. It is done with simulating event rates by choosing true values of $\delta_{\rm CP}$ in the $(\sin^2 2\theta_{13}, \delta_{\rm CP})$ plane. Then these events must be fitted with such CP converved values as $\delta_{\rm CP} = 0\,,\pi$, marginalizing over other degrees of freedom including $\sin^2 2\theta_{13}$. It means ruling out of $\delta_{\rm CP} = 0\,,\pi$. For a 3σ confidence level, χ^2 should be 9 for one degree of freedom.

- The determination of Mass Hierarchy (**MH**):
  the hypothesis with a wrong hierarchy should be excluded at a given confidence level. Usually one can assume a normal hierarchy to simulate event rates. Then data can can be fitted with the opposite hierarchy, marginalizing over other degrees of freedom. It is similar to the case where an inverted hierarchy is assumed at the beginning. For a 3σ confidence level, χ^2 should be 9 for one degree of freedom. Since there are two unknow parameters θ_{13} and $\delta_{\rm CP}$, it is convenient to show results in this two-parameter spanned plane.

- The discovery reach of $\sin^2 2\theta_{13}$ ($\boldsymbol{\theta_{13}}$):
  the hypothesis with $\theta_{13} = 0$ should be excluded at a given confidence level. Therefore, we could simulate even rates for an experiment by taking true values of θ_{13} in a non-zero range. Then these data must be fitted with the assumption $\theta_{13} = 0$ and meanwhile marginalize over other parameters. It directly tells us to which extent we can distinguish a positive θ_{13}-driven oscillation from a $\theta_{13} = 0$ prediction. For a 3σ confidence level, χ^2 should be 9 for one degree of freedom.

In order to show why the neutrino factory is one of the most powerful tools for neutrino oscillation physics, we make a comparison of the discovery reach of CP violation, mass hierarchy and non-zero θ_{13} at the 3σ confidence level in Fig. 4.3, where the CP fraction is defined to be the coverage of CP violating points for each true value of θ_{13} in the range from 0 to 2π. The IDS-NF 1.0 is the current benchmark configuration of neutrino factory. As shown in the Fig. 4.3, we find the neutrino factory will be the best facility sensitive to the mass hierarchy and non-zero θ_{13} no matter which true value of θ_{13} is taken while in the discovery of CP violation the neutrino factory is essentially preferred to the circumstance with $\sin^2 2\theta_{13} \leq 10^{-3}$.

Chapter 5

Near detectors at a neutrino factory

Up to now, there are no near detectors in the design study for the neutrino factory yet. In addition, the baseline setup ususally assumes the systematic errors coming from signal and background normalization errors uncorrelated among all channels and detectors. It is similar to the uncertainties for cross sections as well. With an introduction of near detectors, we could suppress the systematic errors for both the flux normalization and cross sections. In the previous chapter, we have known the oscillation channels of neutrino factory including $\nu_\mu \to \nu_\mu$ disappearance channel. We can take the $\nu_\mu \to \nu_\mu$ channel as an example to explain why we need near detectors. For a near detector for neutrino detections, the number of event rates correspond to the multiplication of the neutrino flux Φ scaled by $1/L^2$ and the cross section σ. Taking into account of the detection efficiency ϵ, we therefore have the following forms of events for near detector (ND) and far detector (FD):

$$\begin{aligned} n_{\nu_\mu}^{\mathrm{ND}} &= \tfrac{N_{\mathrm{ND}}}{L_{\mathrm{ND}}^2}\Phi_{\nu_\mu}\sigma_{\nu_\mu}\epsilon_{\nu_\mu} && (5.1) \\ n_{\nu_\mu}^{\mathrm{FD}} &= \tfrac{N_{\mathrm{FD}}}{L_{\mathrm{FD}}^2}\Phi_{\nu_\mu}P(\nu_\mu \to \nu_\mu)\sigma_{\nu_\mu}\epsilon_{\nu_\mu} && (5.2) \end{aligned}$$

We can immediately identify the dependence of $\sigma_{\nu_\mu}\epsilon_{\nu_\mu}$ cancels between near and far detectors after a combination of them:

$$n_{\nu_\mu}^{\mathrm{FD}} = n_{\nu_e}^{\mathrm{ND}} \frac{N_{\mathrm{FD}}}{N_{\mathrm{ND}}} \frac{L_{\mathrm{ND}}^2}{L_{\mathrm{FD}}^2} P(\nu_\mu \to \nu_\mu) \qquad (5.3)$$

It means that the uncertainty of cross section and detection efficiency will not take any effects assuming the same technology for ND and FD.

Therefore, we intend to propose near detector setups to study neutrino oscillation physics within the IDS-NF with the emphasis on:

- Study of the potential of near detectors to cancel systematical errors.
- Study of the characteristics of the near detectors, such as technology, number, $\cdots$.
- New physics searches.

For the near detectors at a neutrino factory, a summary of options can be found in [19]. The near detectors are supposed to measure the neutrino flux, the neutrino beam angle and its divergence, the neutrino energy, and the neutrino cross sections. For the detection technology, liquid argon time projection chambers, conventional liquid scintillators, scintillating fiber trackers, gas time projection chambers, silicon detectors, and emulsion detectors are mentioned as possible options. These technical details need a lot of research and design study in the testing facilities and certainly out of interests in physics study. From now on, we will assume a very general detector technology and postulate that the near detectors can at least measure the ν_μ (or $\bar{\nu}_\mu$) event rates with (at least) the same energy resolution as the identical far detectors. Whenever the detector is located near the neutrino source, the geometry between the neutrino source and the detector has to be considered precisely. For this purpose, we examine qualitatively different locations of near detectors which in turn result in different characteristics of neutrino detections, such as near detectors covering the whole neutrino flux (near detector limit) and near detectors observing neutrino spectra similar to the far detector (far detector limit). Of course, the case between these two extreme limits is also considered without a loss of generality. In our assumptions, we do not add any additional properties like beam angle measurements in our discussions. The main purpose of this study is an estimate of whether and when near detectors are important for the analysis of neutrino oscillations at the neutrino factory, rather than an accurate description of the near detectors with all their properties, though.

Since it is a near detector, the beam has no time open a large divergent angle yet, the size of these multi-purpose detectors will typically be small. For a typical detector material, the fiducial mass approximates to $\mathcal{O}(100)$ kg. In the mean time, the event rates in the near detector must be extremely high compared to that in the far detector because there is no flux drops due to $1/L^2$. As a rough estimate of events, the near detector measures the multiplication of fluxes and cross sections. However, one can, in principle, discern the fluxes and cross sections in the near detector with the help of different properties of charged current interactions. For example, the purely leptonic inverse muon decay ($\nu_\mu + e^- \rightarrow \nu_e + \mu^-$) has a energy threshold of about 10.9 GeV. As we all know, neutrinos take part in weak interactions, the cross section of which are relatively small compared to other types of interactions. Thus a large fiducial mass of near detector is preferred. It is noted that this point is not the main focus of our study. Instead, we assume that the near detector is able to measure the charged current interactions inclusively. As for the sizes for the near detector, it ranges from a small scale (200 kg) or a "typical" (of the size of the SciBOONE, MINERνA, NOMAD, or the MINOS near detectors) to a large (hypothetical) detector to capture the whole beam. When we turn to the neutrino fluxes, we take rather conservative assumptions. The total number of muons circulating in a storage ring may be inferred from a Beam Current Transformer so that the flux is known to the level of 10^{-3}. However, if the muon beam divergence is too large (and not monitored), additional uncertainties are attached with the flux. For these reasons, we start with a much more conservative assumption (2.5%), and illustrate the improved flux

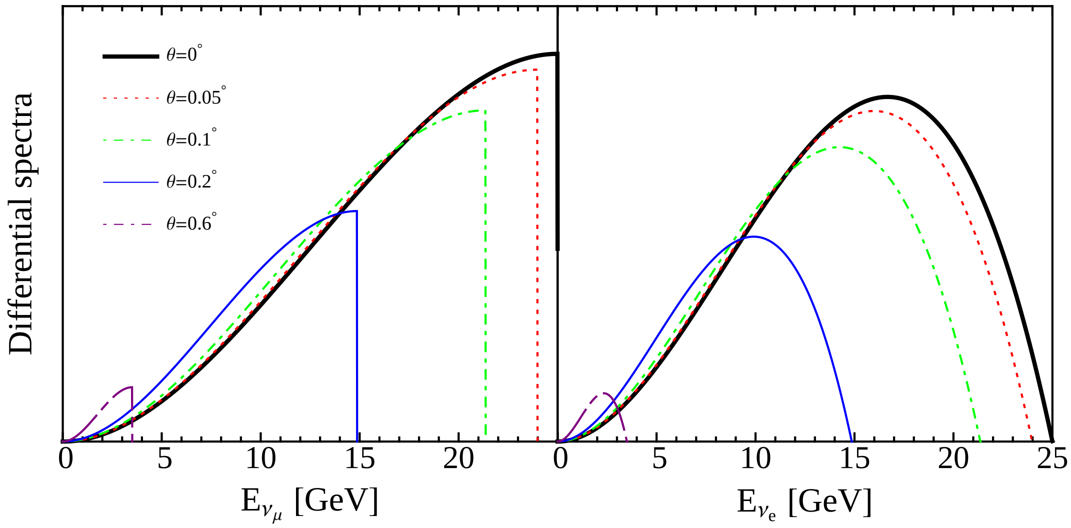

Figure 5.1: *The unpolarized differential neutrino spectra in the laboratory frame for* ν_μ *(left panel) and* ν_e *(right panel), where* $E_\mu = 25$ *GeV and different off-axis angles are used.*

knowledge from different interaction types in the near detectors and beam monitorings, respectively.

5.1 Neutrino factory flux

The (double) differential decay rates of an unpolarized muon in the laboratory frame are derived in the Appendix 11.1 and also given by [23, 24, 83, 84]:

$$\frac{d^2\Gamma}{dE_{\nu_\mu} d\cos\theta} = \frac{G_F^2 m_\mu}{24\pi^3}\gamma(1-\beta\cos\theta)E_{\nu_\mu}^2\left[3m_\mu - 4\gamma E_{\nu_\mu}(1-\beta\cos\theta)\right] , \tag{5.4}$$

$$\frac{d^2\Gamma}{dE_{\nu_e} d\cos\theta} = \frac{G_F^2 m_\mu}{4\pi^3}\gamma(1-\beta\cos\theta)E_{\nu_e}^2\left[m_\mu - 2\gamma E_{\nu_e}(1-\beta\cos\theta)\right] . \tag{5.5}$$

Here ν_α stands for both ν_α and $\bar{\nu}_\alpha$, $\gamma = E_\mu/m_\mu = 1/\sqrt{1-\beta^2}$ is the boost factor, and m_μ is the muon rest mass. The angle θ is the angle between the travel direction of the muon and the observer (in the laboratory frame, at the decay point), which we henceforth call **o**ff-axis angle. The current technology tells us that in a racetrack-shaped storage ring any muon polarization is averaged out with a high precision [19], so that we can use the above formulae to calculate neutrino fluxes in terms of unpolarized spectra. In addition, this is a pure theoretical calculation on these fluxes (the calculated spectrum can be trusted at the level to 10^{-3}), which is expected to be more precise than needed for this study. Especially, the off-axis angle has to satisfy the flavor-independent bounds

$$\theta \le \theta_{\text{cut}} \quad \text{with} \quad \theta_{\text{cut}}(E_\nu) \simeq \frac{1}{\gamma}\sqrt{\frac{E_\mu}{E_\nu} - 1}\,, \tag{5.6}$$

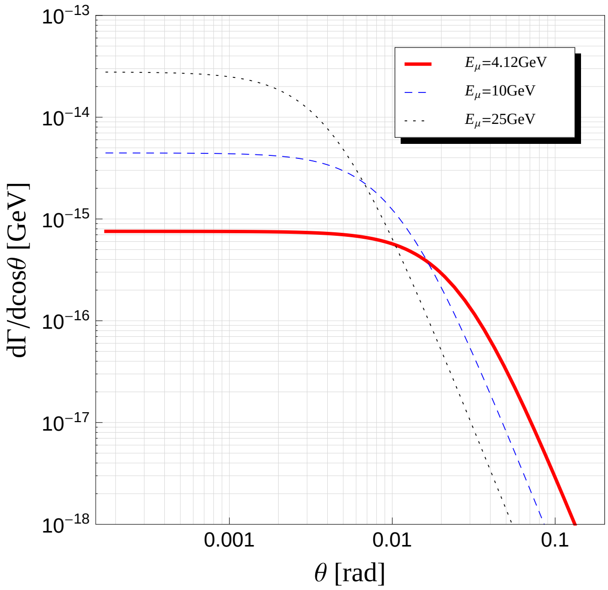

Figure 5.2: *The unpolarized single differential neutrino spectrum integrated over energy as a function of the off-axis angle θ for different values of E_μ. This figure is taken from [32].*

which is a relationship depending on the neutrino energy. In other words, the neutrino spectra are constrained by these bounds to a certain off-axis angle, where the flux approaches zero for $E_\nu > E_{\nu,\mathrm{cut}}(\theta) \simeq E_\mu/(1+(\gamma\theta)^2)$. It indicates that the off-axis angle θ determines the maximal available neutrino energy. Therefore, we have to calculate the spectra in light of any integration over off-axis angle either over the detector's surface area or the energy. We show the spectra after considering the constraints in Fig. 5.1, where the ν_μ spectrum has a sharp cutoff induced by the off-axis angle. Once $E_\nu > E_{\nu,\mathrm{cut}}(\theta)$, the flux becomes zero as anticipated. From Eqn. (5.6), we have the bound $\theta_{\mathrm{cut}} \simeq 0$ for $E_\nu = E_\mu$, which means that the higher the energy of the beam, the more focused the spectra is traveling in the forward direction. For $E_\nu = E_\mu/2$, we have $\theta_{\mathrm{cut}} \simeq 1/\gamma$, which is usually called the opening angle of the beam. However, we will define a different but energy independent spectrum below for the sake of clarity. For small neutrino energies, the beam is obviously expanded wider than that for high energies. It is very interesting because it provides a relative enhancement of the off-axis fluxes at low energies as one can see in Fig. 5.1.

In the following contexts, we intend to integrate over the energy to obtain the single differential decay rate in terms of Eqn. (5.6)

$$\frac{d\Gamma}{d\cos\theta} = \frac{G_F^2 m_\mu^5}{384\pi^3}\frac{1}{[\gamma(1-\beta\cos\theta)]^2}\,. \tag{5.7}$$

The single differential spectra are shown in Fig. 5.2. As we can see, there is a peak at $\theta = 0$ for the energy-integrated decay rate, but the spectrum drops monotoneously with

	Beam divergence $\hat{\theta}$		Beam opening angle $\tilde{\theta}$	
	$\wedge = 0.90$	$\wedge = 0.99$	$\wedge = 0.90$	$\wedge = 0.99$
$E_\mu = 25\,\text{GeV}$	0.0127	0.0420	0.000983	0.000300
$E_\mu = 4.12\,\text{GeV}$	0.0769	0.2538	0.005966	0.001821

Table 5.1: *The beam divergence $\hat{\theta}$ (as defined in Eqn. (5.8)) and the beam opening angle $\tilde{\theta}$ (as defined in Eqn. (5.9)) for two different muon energies and two different fractions $\wedge$. These numbers are obtained from Fig. 5.2.*

the off-axis angle. We could define the (neutrino) **beam divergence** $\hat{\theta}$ by the equation

$$\frac{1}{\Gamma_0}\int_0^{\hat{\theta}} \frac{d\Gamma}{d\cos\theta}\sin\theta d\theta = \frac{1}{2}\int_0^{\hat{\theta}} \frac{1}{\gamma^2(1-\beta\cos\theta)^2}\sin\theta d\theta = \wedge\,, \tag{5.8}$$

where Γ_0 is the total decay rate (integrated over angle and energy) $\Gamma_0 = \frac{G_F^2 m_\mu^5}{192\pi^3}$. The explanation for it is that the fraction $\wedge$ of the total flux is covered in a cone constrained by the angle $\hat{\theta}$. Therefore, the beam divergence helps to define a near detector which captures the total flux of the beam. It also implies that the muon beam divergence has to be much smaller than the neutrino beam divergence, otherwise a sizable amount of events will be lost [19].

In a similar way, we define the **b**eam opening angle $\tilde{\theta}$ as

$$\frac{d\Gamma}{d\cos\theta}|_{\theta=\tilde{\theta}} = \wedge\cdot\frac{d\Gamma}{d\cos\theta}|_{\theta=0}\,, \tag{5.9}$$

which quantifies the angle over which the flux stays almost constant. It defines a near detector which observes a neutrino flux similar to that of a far detector, where the flux at $\theta = 0$ is applied. It is noteworthy that the definition of the opening angle has no energy dependence, while Eqn. (5.6) keeps the dependence of neutrino energy.

To summarize it, we show a table (see Tab. 5.1) of $\hat{\theta}$ and $\tilde{\theta}$ for two different muon energies. As we can see, the larger $\wedge$ becomes, the larger is $\tilde{\theta}$, but the smaller is $\hat{\theta}$. The actual diameter of the beam for these two quantities is finally obtained based on the simple geometric relation:

$$D \simeq 2\times L\times\theta \tag{5.10}$$

where L (baseline) is the distance between production point and observer and D is the diameter of the cylindral detector.

5.2 Definition and spectra of the near detectors

Before we go to the simulations of impacts of near detectors, we define the basic framework for near detectors and calculate neutrino spectra for each case in this section.

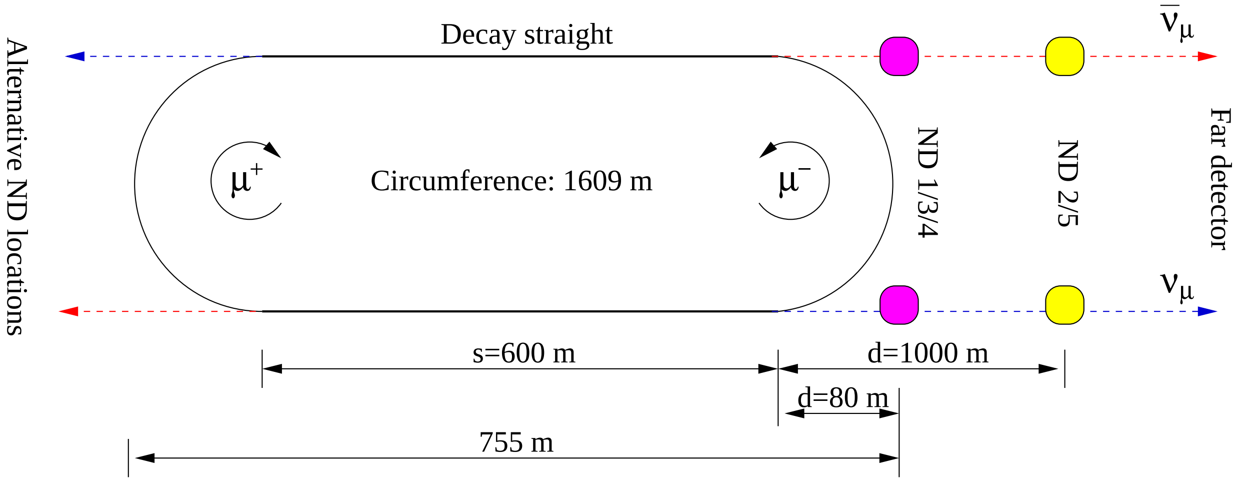

Figure 5.3: *Geometry of the muon storage ring and possible near detector (ND) locations (not to scale). The baseline* L *is the distance between production point and near detector, that is,* $d \leq L \leq d + s$*. This figure is taken from [32].*

5.2.1 Near detector definitions

As shown in the previous paragraphs, we are interested in the different detectors from the flux point of view, where the only purpose is the measurement of neutrino fluxes × the neutrino-interaction cross section. We follow the configuration in IDS-NF [21] to adopt the racetrack-shaped storage ring geometry to design a setup for high energy neutrino factory. The geometry of storage ring and possible near detector locations is plotted in Fig. 5.3 neglecting the scale. For the sake of comparison, we define the criteria for a near detector to break the approximation of two situations such as the far distance approximation and the point source approximation

$$\frac{d^2\Gamma}{dE_{\nu_\alpha} d\cos\theta}(\cos\theta) \simeq \frac{d^2\Gamma}{dE_{\nu_\alpha} d\cos\theta}|_{\theta=0}\,, \quad L \gg s \quad \text{(Size of source)} \tag{5.11}$$

do not hold, and the geometry cannot be neglected.

Our near detector definitions will be based on the following assumptions or observations:

- We operate the near detectors on-axis, because for an off-axis operation, the event rates at high energies will be suppressed according to Eqs. (5.4) and (5.5).

- The only purpose of the near detectors is the ν_μ (from μ^- decays) and the $\bar{\nu}_\mu$ (from μ^+ decays) event rate measurement using the inclusive charged current cross sections. Since the muons and anti-muons are assumed to circulate in different directions in the storage ring shown in Fig. 5.3, two near detectors are required.

- We do not measure the ν_e and $\bar{\nu}_e$ event rates, since we do not need the corresponding

Parameter	ND1	ND2	ND3	ND4	ND5
Diameter D	17 m	4 m	4 m	0.32 m	6.8 m
Distance d	80 m	1000 m	80 m	80 m	1000 m
Mass	450 t	25 t	25 t	0.2 t	2000 t

Table 5.2: *Definition of our near detector fiducial volumes in terms of diameter, distance d to the end of the decay straight (Fig. 5.3), and mass. The fiducial volumes are assumed to be cylindrical. If the density is about* $1\,\mathrm{g}\cdot\mathrm{cm}^{-3}$ *(such as for a liquid scintillator), the active detectors will be about 2 m long for ND1 to ND4. ND5 is assumed to be OPERA-like (with a cylindrical shape for the sake of simplicity). For the low energy neutrino factory, only ND3 is used. ND4 is a down-scale (tabletop) version of ND2 with the same ratio D/L. The ND mass of 25 t is at the upper limit of currently used near detectors. This table is taken from [32].*

cross sections in the neutrino factory far detector.[*] Therefore, we avoid to complicate the cross section discussion (such as to relate the muon neutrino and electron neutrino cross sections).

- We use the same characteristics as in the far detectors, such as energy resolution and binning, for the sake of simplicity.
- We do not extrapolate the backgrounds from the near to the far detector, but instead use relatively large background uncertainties uncorrelated among all channels.
- We assume the fiducial volume to be cylindrical. In addition, we assume that the detector only sees muon decays from the decay straight (denoted by s in Fig. 5.3).[†]

From the conceptual point of view, we postulate that the geometry determines the limiting cases:

Near detector limit In this case, the neutrino beam divergence given by Eqn. (5.8), applied to Eqn. (5.10), is smaller than the detector diameter for the farthest decay point of the decay straight $L = d + s$ so that the full flux (integrated over the angle) is seen by the detector from any decay point in the straight.

Far detector limit In this case, the beam diameter given by the opening angle in Eqn. (5.9) applied to Eqn. (5.10) is of the order of the detector diameter at the nearest decay point $L = d$, so that the far distance approximation in Eqn. (5.11) (first condition) is approximately fulfilled for any decay point in the straight.

---

[*] In fact, not even the dominating backgrounds (charge mis-identification and neutral currents) depend on the electron neutrino cross sections.

[†] The contributions from the curved sections can be estimated to be at the few percent level and can be easily computed once the final geometry is known.

Our near detector parameters are shown in Tab. 5.2. There we define a hypothetical ND1 as a detector operating in the near detector limit, and a ND2 as a detector operating close to the far detector limit. For example, we find from Eqn. (5.10) using $\hat{\theta}$ in Tab. 5.1 ($\wedge = 0.9$) that the beam diameter is about 17 m for $L = s + d = 680\,\mathrm{m}$, which explains the large diameter of ND1 to catch the whole flux. ND3 is an intermediate case between the near and far limits, as we will demonstrate later. The size of ND2 and ND3 is similar to conventional near detectors, such as SciBOONE, MINERνA, NOMAD or the MINOS near detector. ND4 is a smaller version of ND2 with the same ratio between detector diameter and distance d. If the source was a point source so that the straight would be a point, the event rate would be exactly the same as in ND2. Finally, ND5 is an OPERA-like near detector, which we will only use for non-standard physics tests. For a low energy, no storage ring is specified yet. Therefore, we assume the same geometry as in Fig. 5.3 (although a smaller storage ring could be sufficient). Since the beam is much wider because of the smaller boost factor (Tab. 5.1), ND3 will already perform similar to a far detector. Therefore, we only use ND3 for this option. Of course, one can always up-scale or down-scale the discussed detectors (to re-scale the event rate), or change the distance to the source. However, from this qualitative discussion, we have covered all relevant cases allowed by the source geometry. In fact, ND4 may come closest to a realistic near detector.

5.2.2 Near detector fluxes

In order to compute the fluxes for the near detectors, let us first of all look at the number of muon neutrino events produced in a near detector. From the very first principles, it is given by

$$\frac{dN}{dE} = \frac{\sigma}{A}\frac{dN_{\mathrm{Beam}}}{dE} N_{\mathrm{Det}} = \sigma \frac{1}{A_{\mathrm{Det}}} \int\limits_{A_{\mathrm{Det}}} \frac{d^2\Phi}{dEdA} dA \, \frac{M_{\mathrm{Det}}}{m_N} \,, \tag{5.12}$$

where N_{Beam} is the number of neutrinos in the beam (within the detector), N_{Det} is the number of target nucleons in the detector, σ is the cross section per nucleon, and m_N is the nucleon mass. The flux Φ is, for a cylindrical detector, related to the decay rate Γ by

$$\frac{d^2\Phi}{dEdA} = \frac{n_\mu}{\Gamma_0}\frac{d^2\Gamma}{dEd\cos\theta}\frac{1}{2\pi L^2} \tag{5.13}$$

with n_μ the number of useful muon decays, Γ_0 total decay rate, and L the baseline. Applying the far distance and point source approximations Eqn. (5.11) in Eqs. (5.12) and (5.13), we have for the "point source" (PS) event rate

$$\frac{dN_{\mathrm{PS}}}{dE} \simeq \frac{n_\mu}{\Gamma_0}\sigma\frac{1}{A_{\mathrm{Det}}}\int\limits_0^{\theta_{\mathrm{max}}} \frac{d^2\Gamma}{dEd\cos\theta}|_{\theta=0} \sin\theta \, d\theta \, \frac{M_{\mathrm{Det}}}{m_N} \simeq \frac{n_\mu}{\Gamma_0}\sigma \frac{d^2\Gamma}{dEd\cos\theta}|_{\theta=0}\frac{M_{\mathrm{Det}}}{m_N}\frac{1}{2\pi L^2} \,, \tag{5.14}$$

where $\theta_{\mathrm{max}} \simeq D/(2L)$ is related to the detector diameter D. Therefore, only the on-axis flux is needed, the event rate increases linearly with detector mass, and drops as

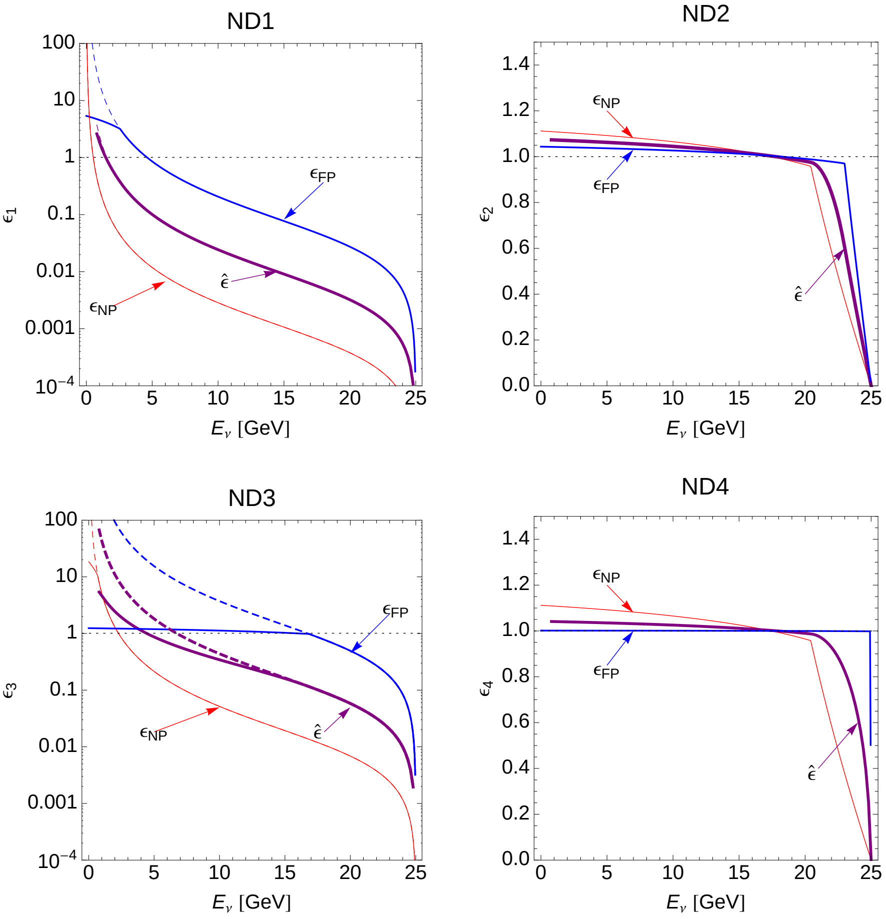

Figure 5.4: *The ν_μ efficiency ratios as a function of E_ν for ND1, ND2, ND3, and ND4. The curves for the farest point ($\varepsilon_{\mathrm{FP}}$) and the nearest point ($\varepsilon_{\mathrm{FP}}$) to the near detector, as well as for the averaged efficiency $\hat{\varepsilon}$ are shown. The horizontal dotted lines express the far detector limit (same spectrum as on-axis spectrum), and the dashed curves the near detector limit (whole flux captured). This figure is taken from [32].*

$1/L^2$. Such a flux is typically used for long-baseline experiment simulations, such as in GLoBES [85, 86].

In our case, we cannot use these approximations for the near detectors. Therefore, we proceed in two steps: first, we fix the production point and integrate over the surface area of the detector; second, we integrate over the decay straight. For a fixed production point in a distance L from the detector, we obtain similar to Eqn. (5.14)

$$\frac{dN}{dE} \simeq \frac{n_\mu}{\Gamma_0}\,\sigma\,\frac{1}{A_{\mathrm{Det}}}\int\limits_0^{\frac{D}{2L}} \frac{d^2\Gamma}{dE d\cos\theta}\,\sin\theta\, d\theta\,\frac{M_{\mathrm{Det}}}{m_N} = \frac{dN_{\mathrm{PS}}}{dE}\,\frac{A_{\mathrm{eff}}}{A_{\mathrm{Det}}} \equiv \frac{dN_{\mathrm{PS}}}{dE}\,\varepsilon(E,L) \qquad (5.15)$$

with the effective area A_{eff} and the efficiency ratio $\varepsilon(E,L)$ determined by

$$A_{\mathrm{eff}} = \frac{2\pi L^2}{\frac{d^2\Gamma}{dEd\cos\theta}|_{\theta=0}} \int\limits_0^{\frac{D}{2L}} \frac{d^2\Gamma}{dEd\cos\theta} \sin\theta \, d\theta \quad \text{and} \quad \varepsilon(E,L) = \frac{A_{\mathrm{eff}}}{A_{\mathrm{Det}}} \,, \tag{5.16}$$

respectively. Therefore, the event rate in an arbitrary near detector can be related to the point source event rate in Eqn. (5.14) with the same L. Then the efficiency ratio ε describes what fraction of the beam is captured compared to the on-axis flux. Note that the event rate is highest on-axis for high neutrino energies and off-axis for low neutrino energies, which means that ε can be larger than one for low neutrino energies, because the detector then captures some of the low energy part which is not present in the point source approximation (Fig. 5.1: for the off-axis spectra, the low energy part is enhanced). From Eqn. (5.16), one can read off that A_{eff} approaches A_{Det}, or ε goes to unity, if the far distance approximation in Eqn. (5.11) is applied.

As the next step, we average Eqn. (5.15) over the decay straight assuming that the probability for muon decay is the same everywhere in the straight (Fig. 5.3):

$$\frac{dN_{\mathrm{avg}}}{dE} = \frac{1}{s} \int\limits_d^{d+s} \frac{dN}{dE} dL = \frac{1}{s} \int\limits_d^{d+s} \frac{dN_{\mathrm{PS}}(L,E)}{dE} \varepsilon(L,E) dL \,. \tag{5.17}$$

From Eqn. 5.14, we find that $\frac{dN_{\mathrm{PS}}(L,E)}{dE} \propto 1/L^2$. Therefore, we can pull out $\frac{dN_{\mathrm{PS}}(L,E)}{dE}$ from the integral in order to obtain

$$\frac{dN_{\mathrm{avg}}}{dE} = \frac{dN_{\mathrm{PS}}(L_{\mathrm{eff}},E)}{dE} \frac{L_{\mathrm{eff}}^2}{s} \int\limits_d^{d+s} \frac{\varepsilon(L,E)}{L^2} dL = \frac{dN_{\mathrm{PS}}(L_{\mathrm{eff}},E)}{dE} \hat{\varepsilon}(E) \tag{5.18}$$

with the average efficiency ratio

$$\hat{\varepsilon}(E) \equiv \frac{L_{\mathrm{eff}}^2}{s} \int\limits_d^{d+s} \frac{\varepsilon(L,E)}{L^2} dL. \tag{5.19}$$

If we choose $L_{\mathrm{eff}} = \sqrt{d(d+s)}$ as the geometric mean between the farest and nearest point baselines of the production straight, we have that $\hat{\varepsilon}(E)$ approaches unity if $\varepsilon(L,E) \equiv 1$ or $L \gg s$ (far distance or point source approximation in Eqn. (5.11)). The meaning of Eqn. 5.18 is the following: Implementing a near detector, we can use the same flux as for a conventional far detector, but with an effective baseline $L_{\mathrm{eff}} = \sqrt{d(d+s)}$, multiplied by the energy-dependent efficiency ratio $\hat{\varepsilon}(E)$ to be computed from the geometry of the source and detector. Therefore, for instance, for an implementation in the GLoBES software, only the effective baseline and $\hat{\varepsilon}(E)$ is needed.

We show in Fig. 5.4 the efficiency ratio $\varepsilon(E)$ for the nearest point of the decay straight to the detector, the furthest point, and the average $\hat{\varepsilon}(E)$ for ND1 to 4 and for ν_μ (the

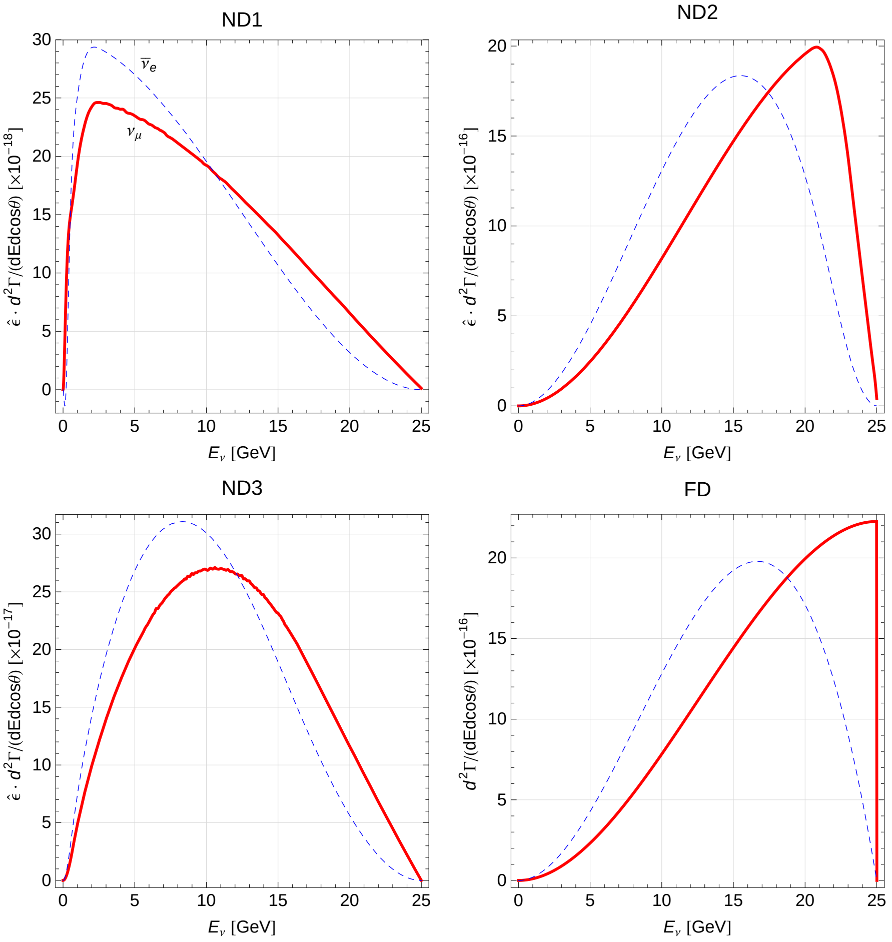

Figure 5.5: *The spectra (differential decay rates multiplied with $\hat{\varepsilon}$) for ND1, ND2, ND3, and the far detector (FD) limit, where the solid curves refer to the ν_μ flux and the dashed curves to the $\bar{\nu}_e$ flux. This figure is taken from [32].*

efficiencies are flavor dependent). Obviously, the efficiency ratios decrease with energy, since for large energies the beam is in most cases smaller than the detector. For low energies, however, a part of the off-axis flux can be captured, leading to an increase of events compared to the on-axis case. The discontinuities in Fig. 5.4 come from Eqn. (5.6): If the beam, which has an energy dependent spread, becomes smaller than the detector, the efficiency ratio (or effective area) strongly decreases. From Fig. 5.4, we can read off that ND2 and ND4 perform similar to the far detector limit, since the efficiency ratios are close to one (even in the high energy part, at least within the energy resolution of the detector). ND1 has efficiency ratios strongly decreasing with energy, which means that the low energy part of the spectrum becomes enhanced. It corresponds to the near detector limit (whole beam captured with dashed curves), as anticipated. ND3 is an intermediate case: The farthest part of the decay straight resembles to the far detector limit, the nearest part the near detector limit.

In Fig. 5.5 the double differential decay rates similar to Fig. 5.1 are shown, but multi-

	Neutrinos (ν_μ)	Antineutrinos ($\bar{\nu}_\mu$)
ND1	1.71×10^{10}	8.82×10^{9}
ND2	3.69×10^{9}	1.93×10^{9}
ND3	1.39×10^{10}	7.21×10^{9}
ND4	9.36×10^{8}	4.89×10^{8}

Table 5.3: *Total event rates for ND1 to 4 for a high neutrino factory with* $E_\mu = 25\,\mathrm{GeV}$ *in ten years.*

plied with the corresponding efficiency factors $\hat{\varepsilon}$. Obviously, compared to the far detector case, the fluxes peak at lower energies, and the low energy part may be enhanced. Again, ND2 performs close to a far detector, ND1 peaks at lower energies, and ND3 is an intermediate case. The event rates for ND1 to 4 are given in Tab. 5.3. Obviously, these rates are much higher than the ones in the far detector (a few hundred thousand in a distance $L = 4000\,\mathrm{km}$), which means that the detectors can in practice be built smaller (unless needed for other measurements, such as for particular cross section measurements).

5.3 Refined systematics treatment

We refine the IDS-NF systematics treatment by introducing the following systematical errors, focusing on the cross section measurement as main purpose of the near detectors:

Flux normalization errors, fully uncorrelated among the different polarities $+$, $-$ and storage rings $S1$, $S2$, but fully correlated among all bins and all channels operated with the same beam. For example, the flux normalizations in appearance and disappearance channels are treated fully correlated, since they come from the same μ^+ decay straight. Therefore, there are four independent errors (two storage rings times two polarities). We assume that the fluxes are known up to 2.5% without knowledge from the near detectors, which is a very conservative starting hypothesis from the current IDS-NF systematics assumptions. However, we also test the impact of an improved flux knowledge of 0.1%, which may be obtained by using various beam monitoring devices [19].

Cross section errors for the inclusive charged current cross sections, fully correlated among all signal and background channels measuring ν_μ or $\bar{\nu}_\mu$, but fully uncorrelated among all bins.[‡] We use bin widths of 1 GeV from 1 to 10 GeV, of 2 GeV from 10 to 20 GeV, and of 2.5 GeV from 20 to 25 GeV, that is, 16 bins in total. This means that we at least crudely follow the energy resolution of $\Delta E\,[\mathrm{GeV}] = 0.55\sqrt{E\,[\mathrm{GeV}]}$. Since we use 16 bins and ν_μ and $\bar{\nu}_\mu$ cross sections, there are 32 uncorrelated errors.

[‡] These errors are more accurately called “shape errors”, because they are practically introduced after energy smearing (whereas cross section errors in principle enter before energy smearing). If the binning reflects the energy smearing, the cross section errors directly correspond to the shape errors.

We adopt a conservative point of view and assumed that the cross section for each bin is externally known to about 30% (see a summary plot in [87]).

Background normalization errors, fully correlated among all bins, but fully uncorrelated among all channels, polarities, and detectors. In total, there are two (polarities) times two (baselines) times two (channels), making eight background errors in the far detectors. We assume a 20% error each, just as in the IDS-NF baseline setup.

Compared to the IDS-NF systematics, the different signal errors are correlated in a particular way. For instance, the cross section errors at the two far detectors are fully correlated, which will turn out to have interesting effects. For the efficiencies, however, we choose the IDS-NF numbers. Note that there might be some uncertainties coming from these efficiencies (such as a fiducial volume error), which we assume to be small and which we do not consider separately because they are not directly relevant for the near detector discussion. In addition, we neglect energy calibration errors.

For our near detectors ND1 to 4, we introduce the same systematics for the backgrounds as for the far detectors, which includes an uncorrelated 20% error for each polarity. For the sake of simplicity, our near detectors have the same energy resolution and binning as the far detector. However, as one important difference, we do not impose charge identification, since only the muon flavor is measured. Therefore, we assume 90% MINOS-like efficiency, starting at a threshold of 1 GeV. Only NC backgrounds are considered, at the level of the far detectors.

5.4 Measurement of the atmospheric parameters

As already discussed above, the near detectors are very important for the atmospheric parameter measurements, which are very sensitive to spectral effects. The impact of the near detectors is illustrated in Fig. 5.6 for a single baseline neutrino factory ($L = 4000\,\mathrm{km}$). The unfilled contours represent the far detector only, whereas the filled contours represent the far-near combination. In the right panel, the effect of the near detectors is very large for maximal mixing. Note that the unfilled contours depend on the knowledge of the cross sections, whereas the filled contours are limited by the statistics in the far detector. In the left panel, a non-maximal value of $\sin^2\theta_{23}$ is chosen. In this case, the effect is less dramatic than in the right panel for maximal mixing, but still substantial. Especially, the octant degeneracy can be excluded with the near detectors at a high confidence level (if $\sin^2 2\theta_{13}$ is large enough).

The results hardly depend on which of ND1 to ND4 is chosen, because they all have sufficient statistics in all bins. This is illustrated in Fig. 5.7, where the Δm^2_{31} allowed range is shown as a function of a luminosity scaling factor rescaling the near detector masses × operation time for two of the near detectors (ND3 and ND4). Comparing the large number of events in our near detectors in Tab. 5.3 with the few hundred thousand

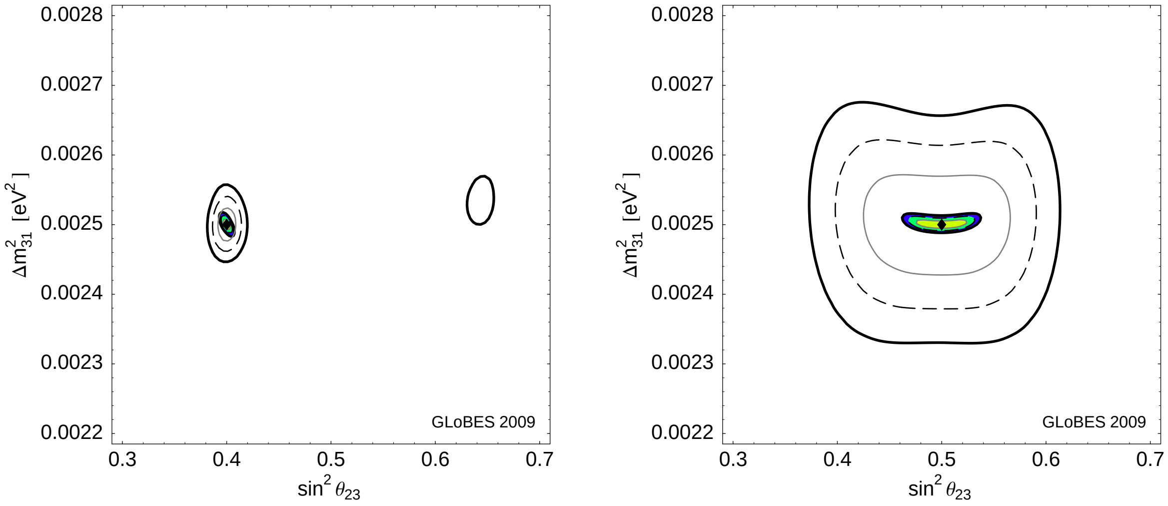

Figure 5.6: *The* $\sin^2\theta_{23}$-Δm^2_{31} *allowed region for a high energy neutrino factory at the* $L = 4000\,\text{km}$ *baseline only;* 1σ, 2σ, 3σ *CL (2 d.o.f.), best-fit points marked by diamonds. The filled contours correspond to our near detector-far detector simulation, whereas the unfilled contours represent the far detector only. Normal hierarchy only without a sign-degenerate solution. In the left panel,* $\sin^2 2\theta_{13} = 0.08$ *and* $\delta_{\rm CP} = 0$, *in the right panel,* $\sin^2 2\theta_{13} = 0$. *This figure is taken from [32].*

events in the far detector (disappearance channel), it is not surprising that even much smaller near detectors would do. Basically, the luminosity starts to become important at the point when the near detector rates are of the order of the far detector rate. From Fig. 5.7 and Tab. 5.2, we can read off at the example of ND4 that, in principle, near detectors with a fiducial mass below 1 kg are sufficient for the standard oscillation parameter measurements. In this case, the near detectors can be easily operated in the far distance limit, where the first part of Eqn.(5.11) applies. Because there is no significant difference among the different near detectors, we only refer to the "near detectors" in the following.

Very interestingly, if the neutrino factory is operated with two baselines at $L_1 = 4000\,\text{km}$ and $L_2 = 7500\,\text{km}$, there is no significant effect of the near detectors – despite the fact, that two additional flux normalization errors for the second storage ring are introduced. Obviously, the spectral errors can be resolved by measuring the same cross sections in two different far detectors similar to a near-far combination, and energy-independent normalization errors are of secondary importance.

5.5 CP violation measurement

We show in Fig. 5.8 the CP violation discovery reach as a function of true $\sin^2 2\theta_{13}$ and the fraction of (true) $\delta_{\rm CP}$ for one far detector (left) and two far detectors (right).

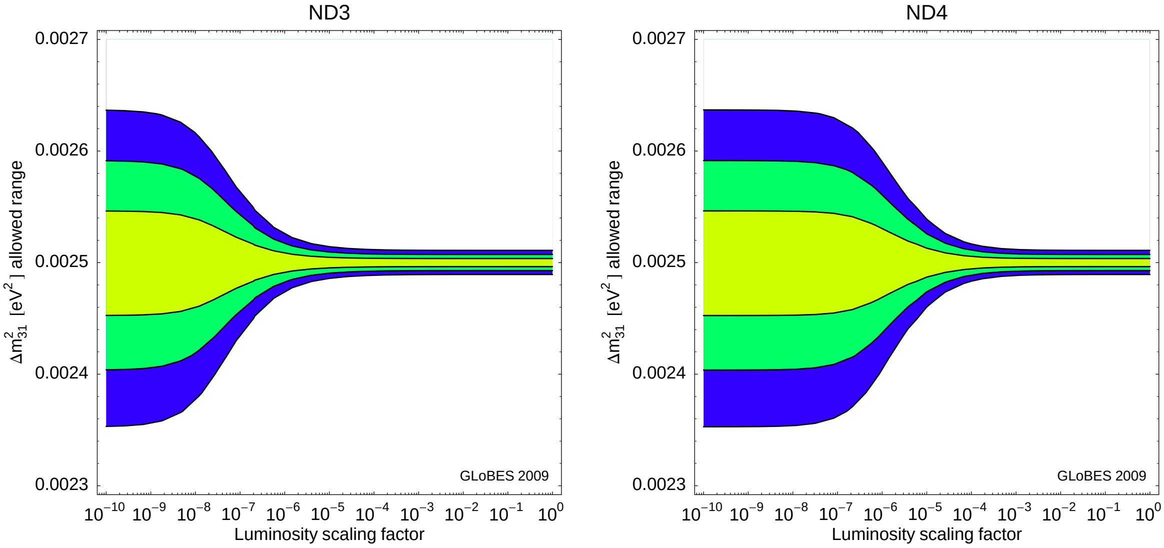

Figure 5.7: *The allowed range for* Δm^2_{31} *as a function of a luminosity scaling factor rescaling the near detector masses* × *operation time (for ND3 and ND4). The contours are shown for the* 1σ, 2σ, 3σ *CL (1 d.o.f.). For* $L_1 = 4000\,\mathrm{km}$ *and normal hierarchy only (no sign-degenerate solution shown), for maximal mixing and* $\sin^2 2\theta_{13} = 0$*. This figure is taken from [32].*

The dashed curves represent the IDS-NF baseline setup with the corresponding systematics treatment, the solid lower curves our systematics treatment without near detectors and flux uncertainties $\sigma_{\mathrm{Flux}} = 2.5\%$, and the solid (thick) upper curves our systematics treatment with near detectors. In the left plot, we include a curve with a better known flux, whereas in the right plot, this curve coincides with the thick curve. As first important observation, our systematics treatment (including near detectors) leads to a better sensitivity that the IDS-NF systematics, in spite of our conservative choices for the systematical uncertainties. The main difference between these two systematics treatments is that we assume the systematical errors to be correlated among different detectors, whereas the IDS-NF setup assumes fully uncorrelated errors. The practical realization will likely be somewhere in the middle (between the dashed and thick curves), since, for instance, cross sections are fully correlated among all detectors measuring the same flavor and polarity, whereas there may be other normalization and spectral errors which depend on the detector (such as fiducial volume errors leading to errors in the detector-dependent efficiencies). Similar to the atmospheric parameter measurement, the near detectors are important for one baseline only, whereas a two-baseline neutrino factory hardly benefits from the near detectors.

For one baseline (left plot), an improved flux knowledge only helps for large θ_{13} in the absence of the near detectors, because the correlation can be resolved and only the uncertainty of the atmospheric parameter measurements remains. We have also tested a

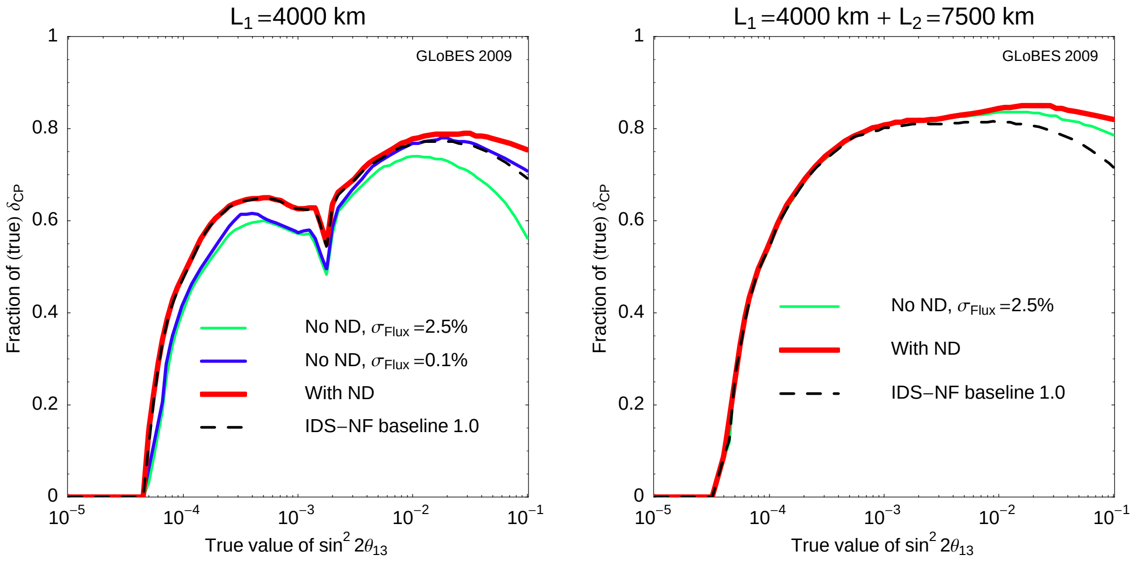

Figure 5.8: *CP violation discovery reach as a function of true* $\sin^2 2\theta_{13}$ *and the fraction of (true)* δ_{CP} *for one far detector (left) and two far detectors (right);* 3σ *CL. This figure is taken from [32].*

better matter density knowledge of 0.5% (compared to 2%), which slightly improves the measurement in all cases for large θ_{13}. In the case of two baselines with near detectors in the shorter baseline storage ring (thick curve in right plot), we have found no improvement from better known fluxes. Since the cross sections can in this case already be extracted by the two near detectors in the first storage ring, this implies that putting additional near detectors in front of the second storage ring, such as for flux monitoring, may not be required from the physics point of view. From the figure, neither a precise flux monitoring nor near detectors are mandatory for a successful CP violation measurement in a two baseline neutrino factory, if the far detectors are well enough understood.

Chapter 6

Optimization of a neutrino factory

The magnetized iron detector (MIND) as a generic neutrino factory detector has backgrounds (such as from neutral currents or charge mis-identification) at the level of about 10^{-3} to 10^{-4}, and the potential to measure the muon charges at relatively low energies down to a few GeV. The importance of the precise location of the detection threshold was discussed in detail in Refs. [28, 57]. As the design of the Neutrino Factory matures, more refined detector simulations have become available [80, 81], especially in comparison to the IDS-NF baseline 1.0 [21]. Compared to the older analyzes, these new simulations provide the detector response in terms of migration matrices mapping the incident to the reconstructed neutrino energy for all individual signal and background channels. An optimization of the cuts has lead to a lower threshold and higher signal efficiencies than in previous versions, while the background level has been maintained in the most recent analysis [81]. In addition, separate detector response functions for neutrinos and anti-neutrinos are available, and it turns out that the $\bar{\nu}_\mu$ detection efficiency is better than the ν_μ detection efficiency, which partially compensates for the different cross sections.[*] Most recently, the background from τ decays was discussed for disappearance [88] and appearance [89] channels. These taus arise from charged current interaction of ν_τ which are due to oscillation, *e.g.*, for μ^+ stored:

$$\text{App.: } \nu_e \to \nu_\tau \to \tau^- \overset{17\%}{\to} \mu^- \text{ (background) versus } \nu_e \to \nu_\mu \to \mu^- \text{ (signal)} \tag{6.1}$$

$$\text{Disapp.: } \bar{\nu}_\mu \to \bar{\nu}_\tau \to \tau^+ \overset{17\%}{\to} \mu^+ \text{ (background) versus } \bar{\nu}_\mu \to \bar{\nu}_\mu \to \mu^+ \text{ (signal)} \tag{6.2}$$

The reason for these muons to contribute to the background is that the MIND cannot resolve the second vertex from the τ decay, in contrast to OPERA-like emulsion cloud chamber (ECC) [90]. In principle, the muons from τ decays carry information which may be used for the standard oscillation [91, 92] or new physics [93] measurements.

---

[*] The difference in neutrino and anti-neutrino response is due to the different y-distributions [81].

6.1 Update of simulations with migration matrices

For the updated detector simulations, we use the migration matrices mapping the incident to the reconstructed neutrino energies for all individual signal and background channels, which can be directly implemented into GLoBES. Note that charge mis-identification, (electron) flavor mis-identification and neutral current backgrounds are included. For the binning, we then follow Ref. [80, 81], where the migration matrices for the appearance channels are given. For the disappearance channels, we use the same matrices.[†] In addition, we increase the number of sampling points for high energies to avoid aliasing. This implementation will be used throughout the remainder of this paper, unless indicated otherwise. It is denoted by the label "new-NF". Note that we also include signal (2.5%) and background (20%) normalization errors, uncorrelated among all oscillation channels.

For the ν_τ contamination, we use the migration matrix from Ref. [89] for both the $\nu_e \to \nu_\tau$ and $\nu_\mu \to \nu_\tau$ channels, since it only depends on characteristics of the τ decays. Note that, since the binning given in there is different from Refs. [80,81], we had to re-bin this matrix carefully. As an important consequence, all events below 2 GeV are collected in the lowest bin. We also apply the muon kinematic cuts for the muons from the τ decays as for the golden channel, following Ref. [89]. In a more refined approach, one may want to have the migration matrices from incident ν_τ energy to reconstructed ν_μ energy directly. This setup will be denoted as "new-NFτ" and it contains everything in new-NF plus the muons from τ decays. As we will show new-NFτ produces practically the same results as new-NF[‡].

The input oscillation parameters are taken as follows [94], unless noted otherwise:

$$\begin{aligned}&\theta_{12} = 34.4^\circ\,, \quad \theta_{13} = 5.6^\circ\,, \quad \theta_{23} = 42.8^\circ\\ &\Delta m_{21}^2 = 7.59 \times 10^{-5}\,\mathrm{eV}^2\,, \quad |\Delta m_{31}^2| = 2.46 \times 10^{-3}\,\mathrm{eV}^2\,.\end{aligned} \tag{6.3}$$

We impose external 1σ errors on Δm_{21}^2 (4%) and θ_{12} (4%) and on Δm_{31}^2 (10%) and θ_{23} (10%) as conservative estimates for the current measurement errors [94]. We also include a 2% matter density uncertainty [95, 96]. Unless noted otherwise, we simulate the normal hierarchy.

In Fig. 6.1, we compare the event rates of the latest detector simulation new-NF (thick solid curves) with IDS-NF 1.0 (thin solid curves) for the four different oscillation channels as given in the plot legend.

IDS-NF 1.0 (thin curves) did not use any migration matrices and this is reflected in the background shape, both neutral current (NC) and charged current (CC), which closely follows the signal shape. The signal shape of IDS-NF 1.0 is quite similar to the one of new-NF, indicating that migrations are not large for the signal, which is not surprising since

---

[†] That is somewhat on the conservative side, since we require charge identification and better results may be obtained with an event sample without charge identification [28].

[‡] This statement is true only for the performance indicators used in this paper, which all focus on the the appearance channel, and will most likely not apply to precision measurements of the atmospheric neutrino parameters in the disappearance channels as indicated in Ref. [88].

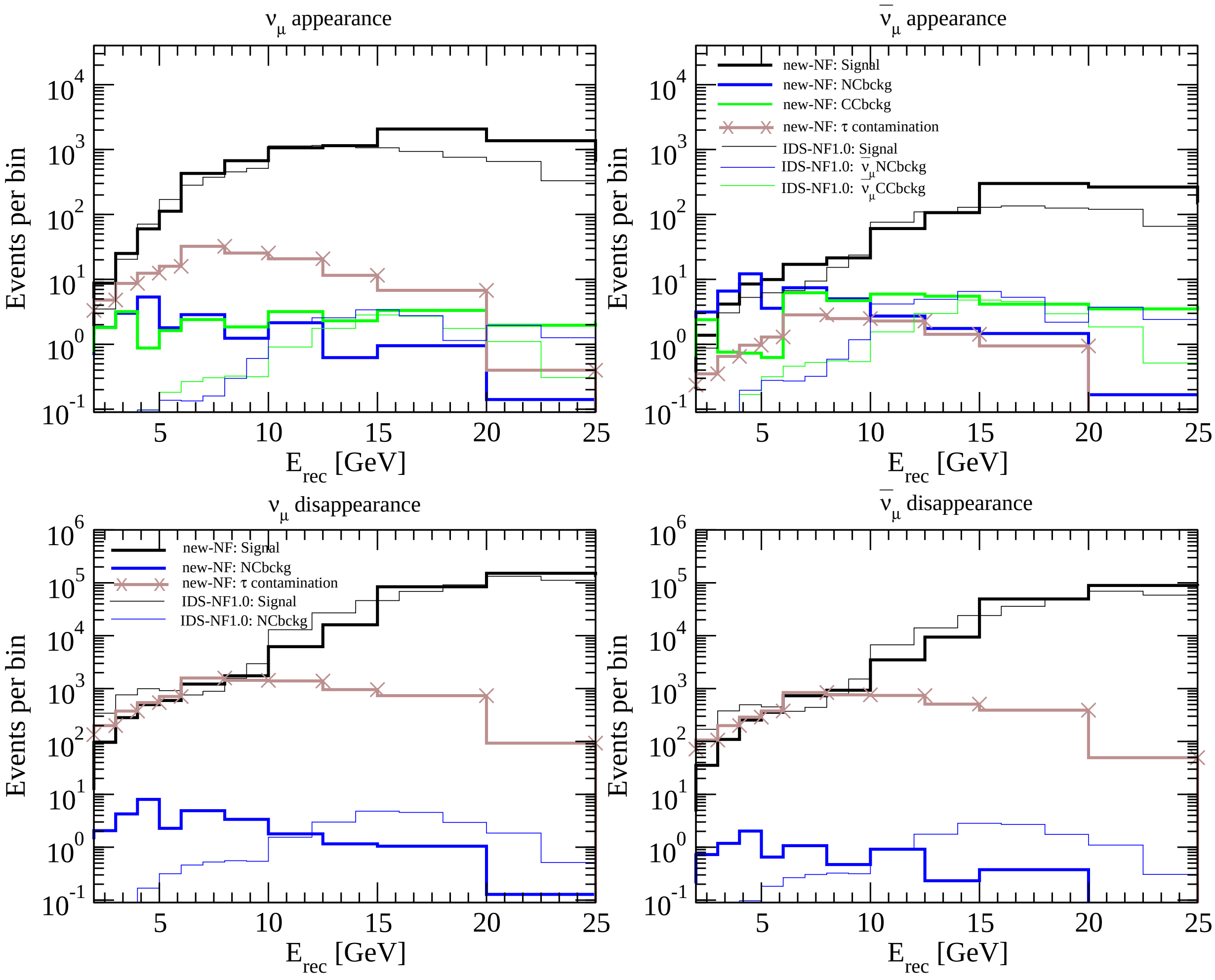

Figure 6.1: *A comparison of the event rate spectra between new-NF [81] (thick curves), including backgrounds from* ν_τ *[88, 89], and IDS-NF 1.0 (thin curves) for the different oscillation channels as given in the plot legend. The chosen oscillation parameters are taken from Eq. (6.3) with* $\delta_{\rm CP} = 0$*. The muon energy is* 25 *GeV and the detector mass is 50kt at a baseline of* 4000 *km. The figure is taken from [97].*

	Signal	NC bckg	CC bckg	ν_τ bckg
ν_μ (app)	7521	20	25	142
$\bar{\nu}_\mu$ (app)	924	45	39	13
ν_μ (disapp)	4.0×10^5	31	-	8154
$\bar{\nu}_\mu$ (disapp)	2.4×10^5	8	-	4337

Table 6.1: *The expected event rates for new-NF*τ *in a 50kt detector at a 4000 km baseline with a muon energy of* 25 *GeV. The chosen oscillation parameters are taken from Eq. (6.3) with* $\theta_{13} = 5.6^\circ$ *and* $\delta_{\rm CP} = 0$.

energy reconstruction works well for the signal events. The background shapes, on the other hand, differ substantially between IDS-NF 1.0 and new-NF, since here migrations are non-negligible. In particular for the NC background, we observe that for new-NF (thick curves) it is quite peaked at low energies. This phenomenon is known as “feed-down”: for a given incoming neutrino energy, there will be less energy deposited in the detector in a NC event than in a CC event, simply because a neutrino is leaving the detector carrying away a sizable fraction of the incoming energy. If a NC event is mis-identified as being a CC event[§], then the CC event kinematics will be used for energy reconstruction, which assumes that $E_\nu^{\mathrm{rec}} = E_{\mathrm{lepton}}^{\mathrm{rec}} + E_{\mathrm{hadrons}}^{\mathrm{rec}}$. This results in a systematic downward bias in the reconstructed energy for NC background events. This feed-down is the strongest effect of migration and thus has potential impact on the energy optimization, since it penalizes neutrino flux at high energies, where there is little oscillation but a large increase in fed-down background. Also, for muons from τ decays there is a strong feed-down for a similar reason: in the decay of a τ there will be two additional neutrinos which leave the detector. Here, the disruptive effect of high energies is even more pronounced, since the ν_τ CC cross section is a steeply increasing function of neutrino energy up to about 30 GeV.

In summary, the CC backgrounds in new-NF pile-up at lower energies. These low energy events are relevant for degeneracy resolution, especially for intermediate values of $\sin^2 2\theta_{13} \sim 10^{-4} - 10^{-2}$. However, the oscillation peak in vacuum would be at about 10 GeV, and matter effects are most important at about 8 GeV, which need to be covered especially for small $\sin^2 2\theta_{13}$, where the event rates otherwise rapidly decrease with distance. The backgrounds from τ decay in new-NFτ tend to collect around 8 GeV and may present an immediate problem for all values of $\sin^2 2\theta_{13}$. Therefore, it is not quite clear that high muon energies are preferred everywhere in the parameter space, and one may suspect that the baseline-muon energy optimization may be a complicated function of the detector response.

6.2 Energy and baseline dependence

Here we study the optimization of a green-field setup, which means that no particular accelerator and detector sites are chosen and that the baselines and muon energy are not constrained. The optimization is performed using the migration matrices from Ref. [81]. Now that the detection threshold has improved, we are especially interested if the new MIND detector can interpolate between low and high energy Neutrino Factory.

First of all, consider that $\sin^2 2\theta_{13}$ is not found before the Neutrino Factory operation. Assume that, in this case, one wanted to optimize for the reach in $\sin^2 2\theta_{13}$, *i.e.*, CPV, MH, and θ_{13} should be discovered for as small as possible true values of $\sin^2 2\theta_{13}$. For the sake of simplicity, we choose maximal CP violation $\delta_{\mathrm{CP}} = \pi/2$ for the true δ_{CP}.[¶] We show in Fig. 6.2 the discovery reach in $\sin^2 2\theta_{13}$ for maximal CP violation, MH, and θ_{13} as a

---

[§] Otherwise, it would not be a background event.

[¶] Other, more technical versions, are choosing the “typical value of δ_{CP}” (the median of the distribution in δ_{CP}), corresponding to a fraction of δ_{CP} of 50%, or a different certain fraction of δ_{CP}. At least for CPV, our choice corresponds to the most optimistic case.

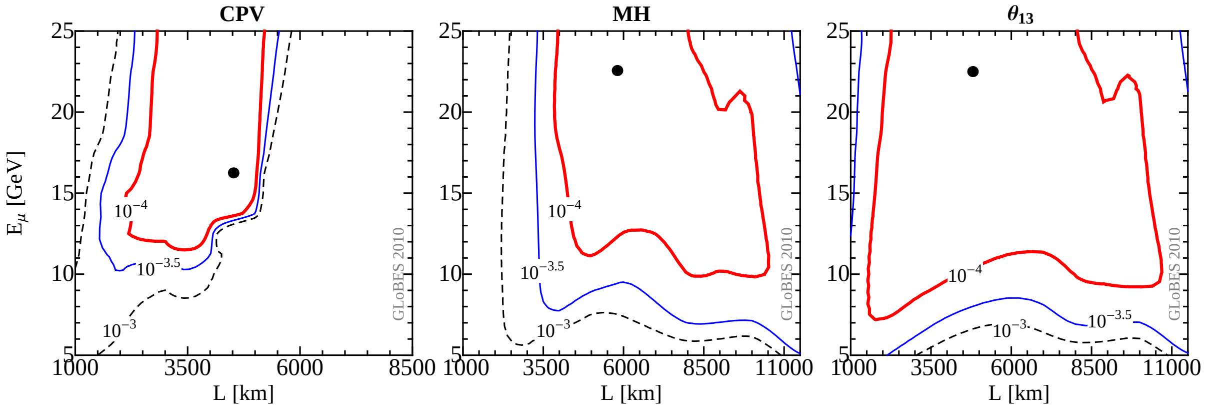

Figure 6.2: *Discovery reach in* $\sin^2 2\theta_{13}$ *for maximal CP violation, MH, and* θ_{13} *as a function of baseline and* E_μ*. The contours show for how small (true)* $\sin^2 2\theta_{13}$ *the different quantities will be discovered at the* 3σ *CL, where maximal CP violation* $\delta_{\mathrm{CP}} = \pi/2$ *is chosen as a true value in all cases. The best reaches for baseline and* E_μ *are marked by dots: (4519,16.25), (5805,22.57) and (4800,22.50) followed by their optimal sensitivity of* $\sin^2 2\theta_{13}$ *at* $10^{-4.8}$, $10^{-4.5}$ *and* $10^{-4.5}$*. Here SF=1 is used with one 50 kt detector. The figure is taken from [97].*

function of baseline and E_μ. The contours show the reach in (true) $\sin^2 2\theta_{13}$ for which the different quantities will be discovered at the 3σ CL. This figure is to be compared to Figs. 5 and 6 of Ref. [28] for the respective δ_{CP} and an older version of the detector simulation. Here the qualitative features are clearly recovered: The CPV discovery requires a 2 500 km to 5 000 km baseline and E_μ above about 12 GeV. Note that degeneracies are typically unproblematic for this choice of δ_{CP}, whereas for $\delta_{\mathrm{CP}} = 3\pi/2$, a second baseline may be required. In addition, note that relatively low E_μ are allowed because of the low detection threshold. For the MH discovery, baselines longer than 4 000 km and E_μ larger than about 10-12 GeV are needed, since the MSW resonance energy of about 8 GeV is to be covered. Here even longer baselines are preferred for different values of δ_{CP}. For the θ_{13} discovery, we find an extremely wide baseline and energy range, giving the least constraints. However, note again that this result depends on the choice of δ_{CP}. In summary, the result of this optimization, qualitatively, points towards one baseline between 2 500 and 5 000 km for the CPV measurement and one very long baseline for the MH measurement, such as the magic baseline at 7 500 km useful for degeneracy resolution (see Ref. [28] for a more detailed discussion). Because of the optimized detector, lower E_μ of down to 12 GeV may be possible. Below, we will discuss how this result changes for specific true values of $\sin^2 2\theta_{13}$ if all values of δ_{CP} are considered.

From a different perspective, consider that the value of $\sin^2 2\theta_{13}$ is known, either from an earlier stage experiment or an earlier stage of the Neutrino Factory. In this case, as we have seen in the previous section, the MH discovery is typically not a problem (at least in combination with a longer baseline if $\sin^2 2\theta_{13}$ is small), and the most interesting question is the optimization of the fraction of δ_{CP} for which CPV can be discovered. We first show

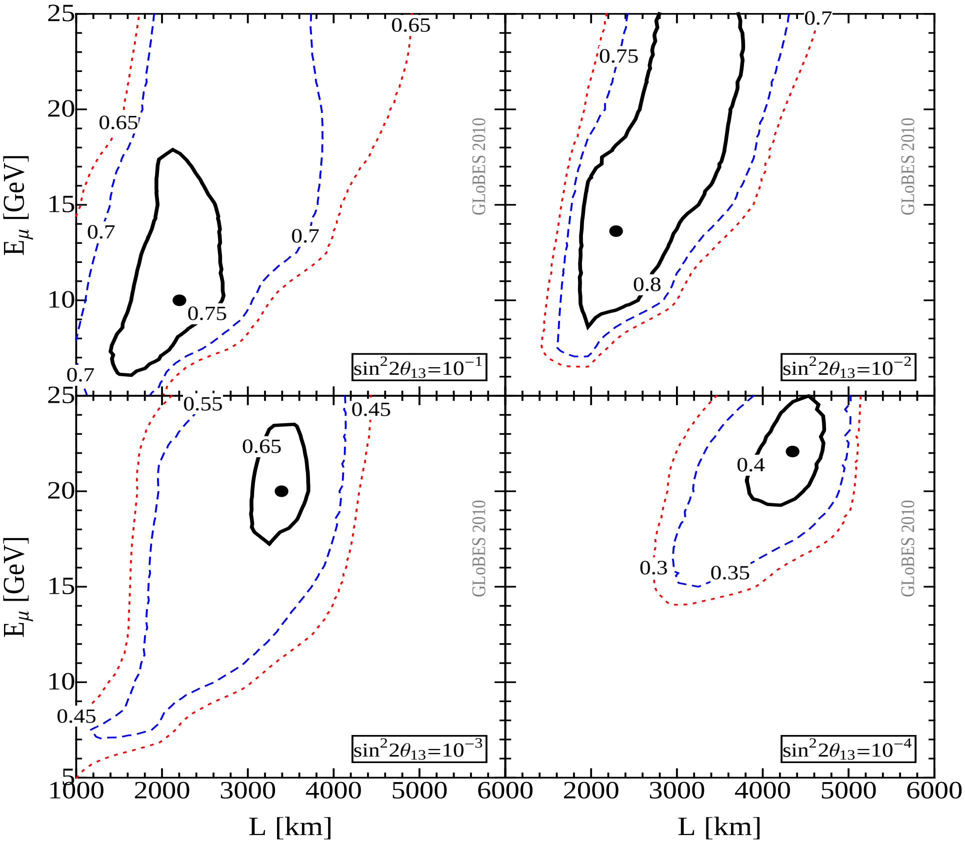

Figure 6.3: *Fraction of* $\delta_{\rm CP}$ *for which CPV will be discovered (*3σ *CL) as a function of* L *and* E_μ *for the single baseline Neutrino Factory. The different panels correspond to different true values of* $\sin^2 2\theta_{13}$*, as given there. Here SF=1 is used with a 50 kt detector. The optimal performance is marked by a dot: (2200,10.00), (2288,13.62), (3390,20.00) and (4345,22.08) with regard to their best reaches of the fraction of* $\delta_{\rm CP}$ *at: 0.77, 0.84, 0.67 and 0.42. The figure is taken from [97].*

in Fig. 6.3 the fraction of $\delta_{\rm CP}$ for which CPV will be discovered (3σ CL) as a function of L and E_μ for the single baseline Neutrino Factory. The different panels correspond to different true values of $\sin^2 2\theta_{13}$, as given there. From this figure, it is obvious that the optimization strongly depends on the value of $\sin^2 2\theta_{13}$ chosen. For large $\sin^2 2\theta_{13} \simeq 10^{-1}$, shorter baselines and lower energies are preferred. Even E_μ as low as 5 GeV at the FNAL-Homestake baseline of about 1 300 km is not far from optimal, which means that the MIND detector approaches the TASD performance of the low energy Neutrino Factory. Very interestingly, compared to earlier analyses without background migration, too high E_μ are in fact disfavored in the large $\sin^2 2\theta_{13}$ case. Note that for the considered detector, we do not find any evidence supporting the "bimagic baseline" argument in Ref. [49], *i.e.*, we do not find enhanced sensitivity for $E_\mu \simeq 5\,$GeV and $L \simeq 2\,540\,$km, no matter if one or two muon polarities are used. For the other extreme, $\sin^2 2\theta_{13} \simeq 10^{-4}$, baselines between 4 000 and 5 000 km are preferred with $E_\mu \simeq 20 - 25$ GeV, which corresponds more to

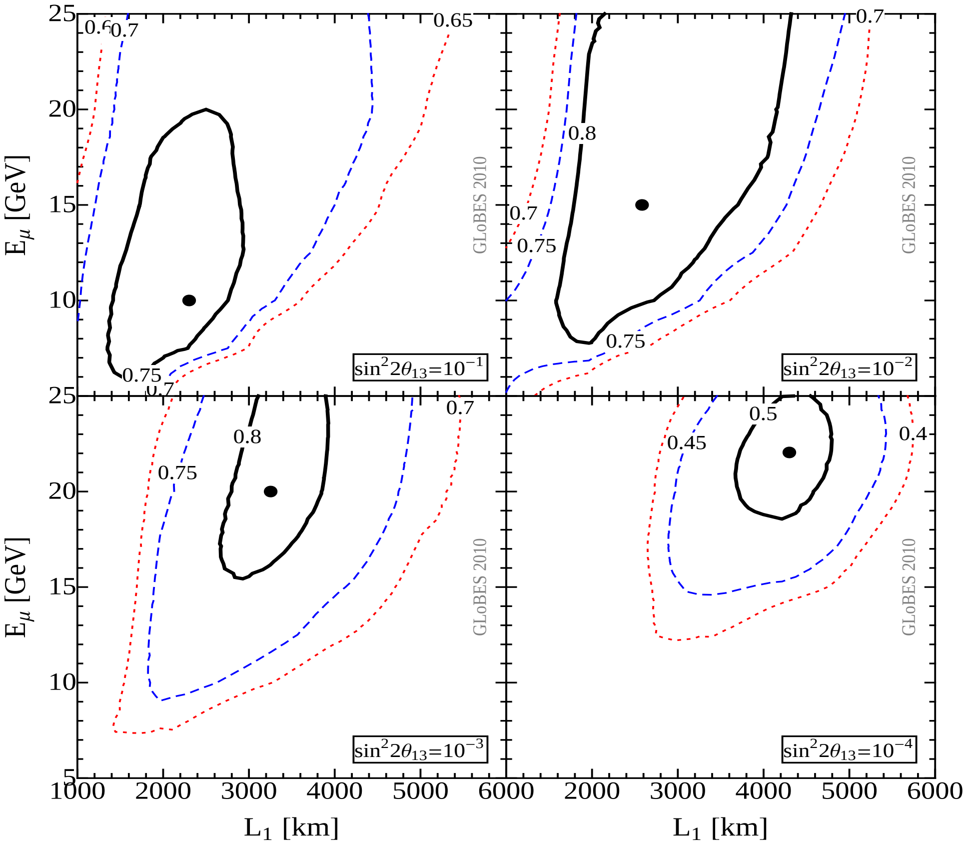

Figure 6.4: *Fraction of* $\delta_{\rm CP}$ *for which CPV will be discovered (*3σ *CL) as a function of* L_1 *and* E_μ *for the two-baseline Neutrino Factory, where* $L_2 = 7\,500\,\text{km}$ *fixed. The different panels correspond to different true values of* $\sin^2 2\theta_{13}$*, as given there. Here SF=1 is used and* E_μ *is assumed to be equal for both baselines. Two 50 kt detectors are used in the simulations. The optimal performance is marked by a dot: (2300,10.00), (2580,15.00), (3250,20.00) and (4297,22.05) followed by their best discovery reach of the fraction of* $\delta_{\rm CP}$ *at 0.77, 0.84, 0.81 and 0.51. The figure is taken from [97].*

the high energy Neutrino Factory, such as the IDS-NF baseline. Including the other two panels, the optimal region within each panel moves from the lower left on the plots to the upper right as the value of $\sin^2 2\theta_{13}$ decreases. This means that, depending on the choice of $\sin^2 2\theta_{13}$, the optimization results in the low energy Neutrino Factory, the high energy Neutrino Factory, or an intermediate scenario, and that the low and high energy Neutrino Factories are just two versions of the same experiment in different optimization regions. Of course, this discussion is somewhat hypothetical from the practical point of view, since either the next generation(s) of experiments will find $\sin^2 2\theta_{13}$ or not. If they find $\sin^2 2\theta_{13}$, the optimal parameters of the Neutrino Factory can be clearly predicted as a function of the detector response. The FNAL-Homestake low energy Neutrino Factory is one such possible setup for large enough $\sin^2 2\theta_{13}$ for the MIND detector. If they do not find $\sin^2 2\theta_{13}$, one may want to go for the IDS-NF high energy setup, which, in a way, represents the most aggressive but also inclusive option: This version of the Neutrino Factory is optimized for the worst case scenario.

Apart from the single baseline, we show in Fig. 6.4 the combination with another fixed baseline $L_2 = 7\,500\,\mathrm{km}$ (in fact, there is typically very little dependence on the exact choice of the second baseline [29]). Note that the muon energy is the same for both baselines. Comparing Fig. 6.4 with Fig. 6.3, we find that the optimization of the short baseline hardly changes for very small and very large $\sin^2 2\theta_{13}$, whereas the possible baseline windows for intermediate $\sin^2 2\theta_{13}$ (upper right and lower left panels) become somewhat broader. The energy optimization remains almost unaffected. As far as the absolute performance is concerned, especially for $\sin^2 2\theta_{13} = 10^{-3}$ and $\sin^2 2\theta_{13} = 10^{-4}$, the fraction of δ_{CP} increases because of the degeneracy resolution potential of the second baseline (which is not sensitive to δ_{CP} itself by choosing exactly the magic baseline). For large values of $\sin^2 2\theta_{13}$, the second baseline is not required. This again reflects the correspondence to low and high energy Neutrino Factory: the low energy version is typically proposed with one baseline, the high energy version with two baselines.

Chapter 7

Low-energy neutrino factory

For several reasons, such as external boundary conditions, a neutrino factory complex may not be built at once, but instead be regarded as a step-by-step program, perhaps, towards a muon collider. In this study, we discuss both the Low Energy Neutrino Factory (LENF) and High Energy Neutrino Factory (HENF), where we are particularly interested in upgrade scenarios. This means that we demonstrate how building a neutrino factory in stages makes sense physics-wise, and we illustrate how the knowledge from earlier data affects the optimization. As we know from the Chapter 5, LENF has a good advantage for the large θ_{13} case. We intend to discuss the minimal requirements for LENF to measure the yet unknown parameters, assuming the beam energy at 10 GeV. A scan of the baseline is also studied, since no specific site is chosen for LENF yet. In addition, we make a comparison of LENF by taking an illustrative baseline at 2000 km and HENF with a IDS-NF baseline setup. It is noted that they are using the same type of detector MIND, where the latest migration matrices are included. Finally, we propose an option to obtain the low-energy version of neutrino factory by off-axis technology. The physics study should repeat in the same way.

7.1 The minimal low-energy neutrino factory

Here we investigate the minimal requirements for a neutrino factory. In addition, we only consider one baseline. We assume that the measurement should be independent of that from other experiments, such as Daya Bay, and we do not consider any additions or upgrades.

Compared to the small $\sin^2 2\theta_{13}$ case, it is much easier to define a minimum wish list if $\sin^2 2\theta_{13}$ has already been observed. Here we follow the minimum wish list in [98] (which was discussed there in context of the beta beam):

1. 5σ independent confirmation of $\sin^2 2\theta_{13} > 0$ (for any δ_{CP}).

2. 3σ determination of the mass hierarchy (MH) for *any* (true) δ_{CP}.

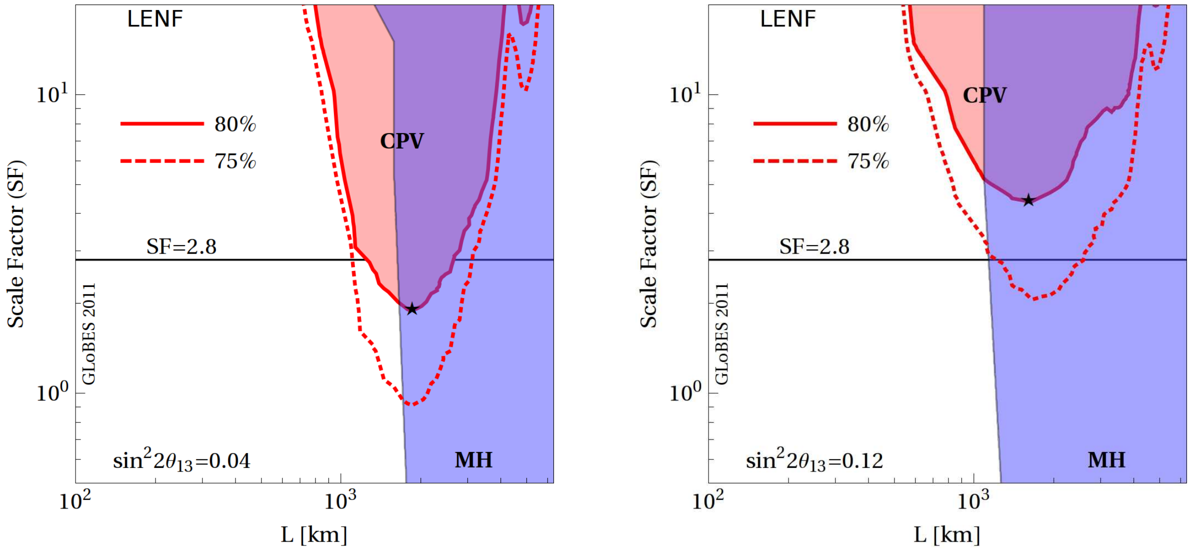

Figure 7.1: *Discovery of CPV (dark/red) and MH (medium gray/light blue) for the one baseline (minimal) LENF as a function of baseline and luminosity scale factor SF. Discovery reach is given within the shaded regions at the* 3σ *CL, where for CPV a fraction of* $\delta_{\rm CP}$ *of 75% or 80% is required (as indicated), and for the MH a fraction of* $\delta_{\rm CP}$ *of 100%. The stars show the baseline with the minimal SF: in the left panel* $(1850\,\mathrm{km}, 1.95)$ *and in the right panel* $(1600\,\mathrm{km}, 4.5)$*. The nominal luminosity is given by SF=2.8. Here the true value of* $\sin^2 2\theta_{13}$ *is chosen as given in the plot panels, and a normal hierarchy is assumed. The matter density uncertainty is assumed to be 2%.*

3. 3σ establishment of CP violation (CPV) for a certain fraction (such as 80%) of all (true) $\delta_{\rm CP}$.

The only “arbitrary” in this list is the fraction of $\delta_{\rm CP}$ for which CPV should be discovered. A fraction of 80% corresponds to Cabibbo-angle precision [55]. Alternatively, it corresponds to the precision of the CP phase in the quark sector is measured. In this wish list, point 1 is typically easy for most of the parameter space; therefore, we do not show it explicitely anymore. Point 2 typically requires a certain minimum baseline. Point 3 requires sufficient luminosity and an appropriate baseline window close to the oscillation maximum. Compared to [98], we simplify the analysis somewhat and show the results only for particular choices of (true) $\sin^2 2\theta_{13}$ (not ranges allowed by the next generation of experiments). Of course, the choice of $\sin^2 2\theta_{13}$ will be motivated by the results from preceding experiments. In addition, we show the normal hierarchy only.

In order to identify the minimal version of the neutrino factory, we re-optimize the baseline, and, at the same time, identify the minimum luminosity for the optimal baseline with respect to the above performance indicators. For the LENF, we show in Fig. 7.1 the discovery reach for CPV (dark/red) and MH (medium gray/light blue) as a function of baseline and luminosity scale factor SF. Discovery reach is given within the shaded regions at the 3σ CL, where for CPV a fraction of $\delta_{\rm CP}$ of 75% or 80% is required (as indicated), and for the MH a fraction of $\delta_{\rm CP}$ of 100%. Sensitivity to both performance indicators is given in the overlap region, where one typically also has θ_{13} discovery potential for all $\delta_{\rm CP}$. The stars mark the points with the minimal SF where *all* performance indicators can be measured; they therefore show the "minimal configurations". For the LENF, the minimal baseline is determined by the MH reach, and the minimal SF by the CPV reach. The nominal luminosity (SF=2.8) is sufficient for the CPV measurement for 80% of all true $\delta_{\rm CP}$ and for the MH measurement for all $\delta_{\rm CP}$ in the baseline window $1100\,\text{km} \lesssim L \lesssim 1400\,\text{km}$ for both values of $\sin^2 2\theta_{13}$ (left and right panel). One can read off these figures that luminosity is clearly an issue for large $\sin^2 2\theta_{13}$. If, for instance, only a lower SF can be achieved, the CPV discovery reach decreases accordingly. The "minimal" (optimal) LENF with the lowest SF is in both panels at about $L \simeq 1100\,\text{km}$. However, the FNAL-DUSEL baseline $L = 1290\,\text{km}$ is close enough to optimum.

7.2 High-energy v.s low-energy neutrino factory

It is then time to make a comparison between the low energy neutrino factory and high energy neutrino factory to see the advantages of them in parameter space. For the high energy neutrino factory, we employ the standard IDS-NF setup with $E_\mu = 25$ GeV, where two 50 kt MINDs are located at 4000 km and 7500 km. As for the low energy neutrino factory with $E_\mu = 10$ GeV, we perform an illustrative simulations for a 50 kt MINDs at 2000 km. All the latest migration matrices are included in the simulations. In Fig. 7.2, we depict the discovery reach of CPV, MH and non-zero $\sin^2 2\theta_{13}$ for them. We see a low energy neutrino factory is obviously better in the CPV plane when $\sin^2 2\theta_{13}$ is larger than 10^{-2}. It matches the pure theoretical discussions that CPV has a large chance in the low energy range in the previous section. Similarly, we could understand the significant loss of sensitivities in the MH plane by the matter effects. The discovery potential of MH is mainly driven by matter effects. The longer the baseline, the larger the matter effects. Meanwhile, the chosen baseline should match the neutrino energy since neutrino flavor evolutions change with L/E. Finally, the non-zero $sin^2 2\theta_{13}$ is mostly limited in statistics so that more event rates are preferred at this issue. As we know from the neutrino spectra by muon decays, a higher muon beam always helps at this point. This explains the slightly better discovery reach of $\sin^2\theta_{13}$ in Fig. 7.2.

7.3 Off-axis neutrino fluxes

We use the TASD as off-axis detector in the HENF with $E_\mu = 25\,\text{GeV}$ with an off-axis angle of 0.3°. The considered spectrum of this off-axis neutrino factory detector (OAD) is practically identical to that of the LENF for this off-axis angle, which is a feature of the neutrino factory flux (see [32]). Since the similar simulations can be performed the same to the low energy neutrino factory, we suppress the further discussions here and keep open in mind the possibility to use off-axis technology to build a neutrino factory in

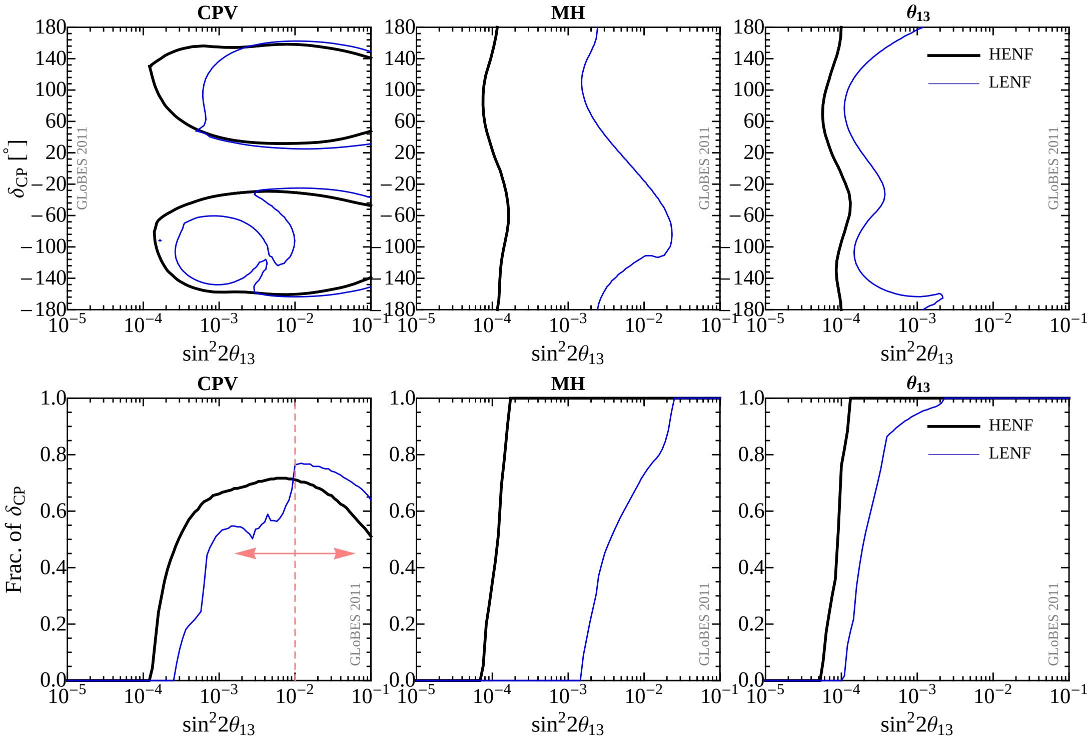

Figure 7.2: *A comparison of discovery reach of CPV, MH and non-zero* $\sin^2 2\theta_{13}$ *between a high energy neutrino factory (HENF) and a low energy neutrino factory (LENF) at* 5σ *C.L. Here a normal mass hierarchy is assumed.*

stages.

In a short summary, we concentrate on the low energy neutrino factory. The minimal requirements of low energy neutrino factory are listed in order and the relevant luminosity is also scanned. In addition, it is fair to make a comparison between HENF and LENF with the same detector. We find that they are just two different versions of the same experiment optimized for different parts of the parameter space. The low energy neutrin factory has a better chance to perform a CPV discovery if the $\sin^2 2\theta_{13}$ is larger than 10^{-2} and to be discovered by the next generation neutrino experiment. Otherwises, a staging scenario towards high energy neutrino factory is preferred based on the demands of discovery potentials of MH and an extremely small θ_{13}. Finally, we briefly argue that it migth be an option to make use of low energy advantages towards CPV discovery in light of the off-axis technology, since the low energy beam can be obtained automatically with $E_\mu = 25$ GeV and an off-axis angle of 0.3°.

Chapter 8

Comments on the bimagic baseline setup at a neutrino factory

Recently it is proposed to use a so-called bimagic baseline at a low energy neutrino factory in [49], which discusses the effect that the dependence on $\delta_{\rm CP}$ at a particular baseline and energy disappears ("bimagic baseline") for a chosen mass hierarchy. It has been studied in the context of a low energy neutrino factory together with a magnetized totally active scintillator detector (TASD). It was concluded that the "bimagic baseline seems like an optimal one to probe the three most important unknown parameters of the leptonic mixing matrix: θ_{13}, $\delta_{\rm CP}$, and the sign of Δm^2_{31}". See also Ref. [99] for the bimagic baseline in terms of a superbeam, and Ref. [100] for its baseline optimization. Here comes a few questions in mind.

- Why is there a so-called bimagic baseline at 2540 km in theory?
- Is it important for the low-energy neutrino factory to use the bimagic baseline in practice?
- What is the essential point in experimental setups to make the bimagic baseline visible in the simulation results?

The ν_μ appearance probability in the constant density matter can be expanded to the second order in $\sin 2\theta_{13}$ and the hierarchy parameter $\alpha \equiv \Delta m^2_{21}/\Delta m^2_{31} \simeq 0.03$, as already derived in Eqn. (2.71):

$$
\begin{aligned}
P_{e\mu} &\simeq \sin^2 2\theta_{13} \sin^2\theta_{23} \frac{\sin^2[(1-\hat{A})\Delta_{31}]}{(1-\hat{A})^2} \\
&\pm \alpha \sin 2\theta_{13} \sin\delta_{\rm CP} \sin 2\theta_{12} \sin 2\theta_{23} \sin(\Delta_{31}) \frac{\sin(\hat{A}\Delta_{31})}{\hat{A}} \frac{\sin[(1-\hat{A})\Delta_{31}]}{(1-\hat{A})} \\
&+ \alpha \sin 2\theta_{13} \cos\delta_{\rm CP} \sin 2\theta_{12} \sin 2\theta_{23} \cos(\Delta_{31}) \frac{\sin(\hat{A}\Delta_{31})}{\hat{A}} \frac{\sin[(1-\hat{A})\Delta_{31}]}{(1-\hat{A})} \\
&+ \alpha^2 \cos^2\theta_{23} \sin^2 2\theta_{12} \frac{\sin^2(\hat{A}\Delta_{31})}{\hat{A}^2} \qquad (8.1)
\end{aligned}
$$

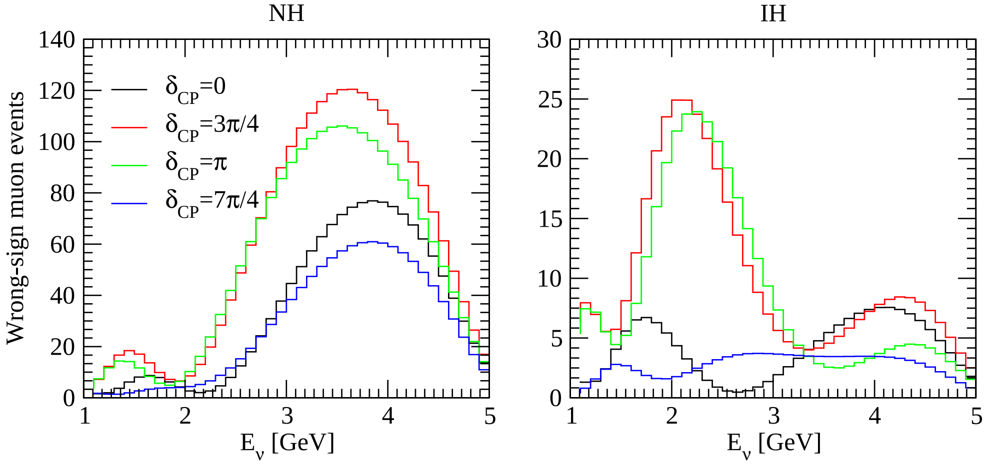

Figure 8.1: *The signal spectra of different* $\delta_{\rm CP}$ *for the* ν_μ *appearance channel of TASD at the neutrino factory, using* $E_\mu = 5$ GeV*and* $L = 2540$ km. *The oscillation parameters are chosen based on Eqn.(8.8).*

with $\Delta_{31} \equiv \Delta m^2_{31} L/(4E)$ and $\hat{A} = \pm 2\sqrt{2}\, E\, G_F\, n_e/\Delta m^2_{31}$ where n_e is the number density of electrons in matter. The signs in the second term and $\hat{A}$ are positive for neutrinos and negative for anti-neutrinos. This channel provides the wrong sign muons at the neutrino factory. Let's reorganize $|\hat{A}| = 7.59 \times 10^{-5}[\frac{\rho}{\rm g/cm^3}][\frac{E}{\rm GeV}][\frac{\rm eV^2}{|\Delta m^2_{31}|}]$ with $\Delta_{31} = |\Delta_{31}|$ for Normal Hierarchy (NH) and $\Delta_{31} = -|\Delta_{31}|$ for Inverted Hierarchy (IH) with $|\Delta_{31}| = 1.269[\frac{|\Delta m^2_{31}|}{\rm eV^2}][\frac{\rm GeV}{E}][\frac{L}{\rm km}]$. On one hand, to meet the requirement of $\sin[(1-\hat{A})\Delta_{31}] = 0$ we should have

$$(1 + |\hat{A}|) \cdot |\Delta_{31}| \;=\; n\pi \qquad \text{for IH}\,, \tag{8.2}$$

$$(1 - |\hat{A}|) \cdot |\Delta_{31}| \;=\; m\pi \qquad \text{for NH}\,, \tag{8.3}$$

where n and m are positive integers. On the other hand, to meet the need of $\sin[(1-\hat{A})\Delta_{31}] = \pm 1$ we arrive at

$$(1 + |\hat{A}|) \cdot |\Delta_{31}| \;=\; (n - \frac{1}{2})\pi \qquad \text{for IH}\,, \tag{8.4}$$

$$(1 - |\hat{A}|) \cdot |\Delta_{31}| \;=\; (m - \frac{1}{2})\pi \qquad \text{for NH}\,, \tag{8.5}$$

Eqn.(8.2) and Eqn.(8.5) have different hierarchies so that we can make use of them to obtain the interesting baseline and beam energy:

$$\left[\frac{\rho}{\rm g/cm^3}\right] \cdot \left[\frac{L}{\rm km}\right] \;\approx\; (n - m + 1/2) \times 16308\,, \tag{8.6}$$

$$\left[\frac{E}{\rm GeV}\right] \;=\; 0.8079 \times \frac{1}{n + m - 1/2}\left[\frac{|\Delta m^2_{31}|}{\rm eV^2}\right] \cdot \left[\frac{L}{\rm km}\right] \tag{8.7}$$

We could obtain the so-called bimagic baseline $L \approx 2540$ km if we take $n = 1$ and $m = 1$ as an example and assume $\rho = 3.21 {\rm g/cm^3}$ in the matter *. The interesting beam energy

---

*For the details of matter density in the earth, see the Preliminary Reference Earth Model [51].

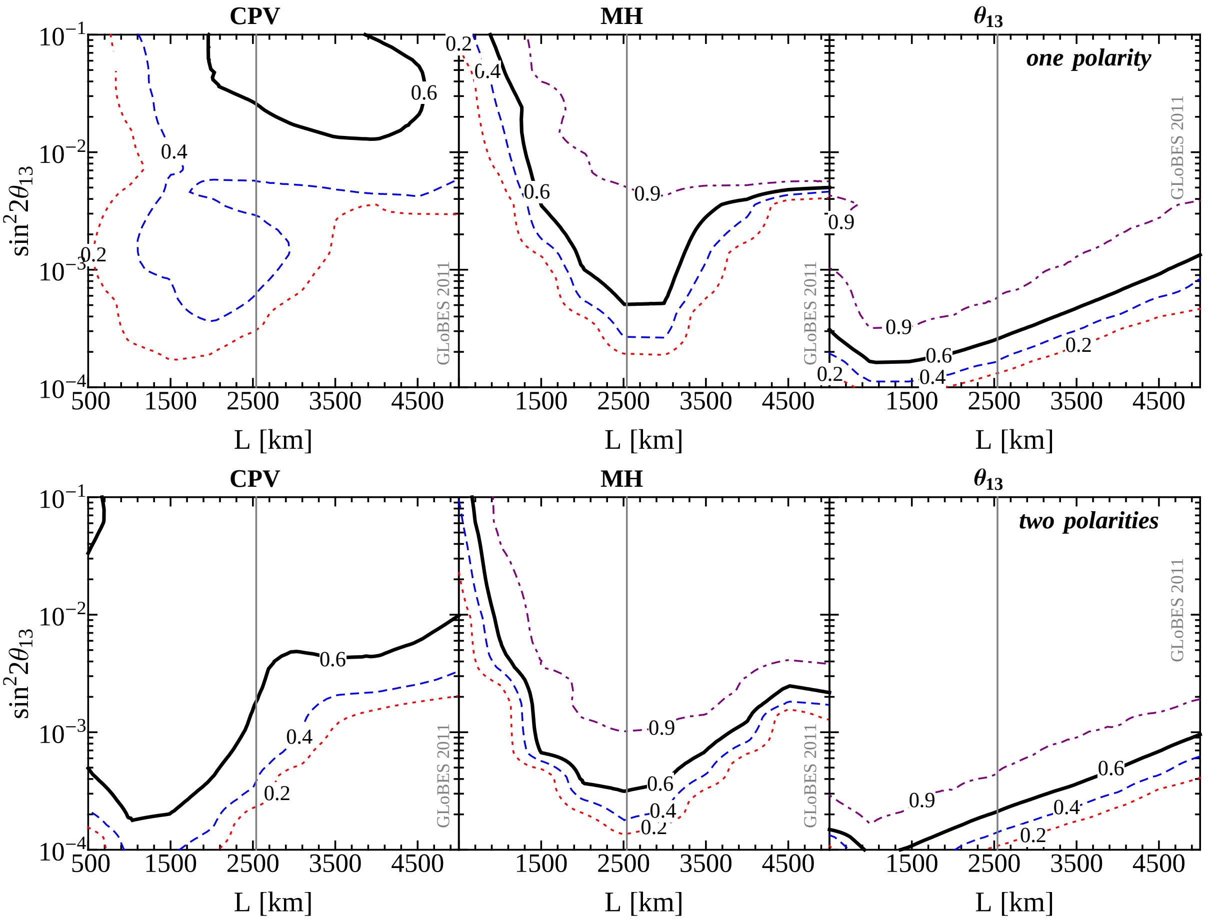

Figure 8.2: Discovery reach in $\sin^2 2\theta_{13}$ as a function of baseline for CPV, MH, and θ_{13} discovery and specific fractions of $\delta_{\rm CP}$ (contours). The upper row is for one polarity (μ^+ stored), the lower for two polarities. Normal hierarchy, 3σ.

would be $E \approx 3.28$ GeV.

We consider the magnetized type of Totally Actively liquid Scitillator Detector (TASD) in the neutrino factory with only one polarity in the storage ring. The best-fit oscillation parameters are taken as follows [49]:

$$\begin{aligned} &\sin^2\theta_{12} = 0.3\,, \quad \sin^2\theta_{13} = 10^{-2}\,, \quad \sin^2\theta_{23} = 0.5 \\ &\Delta m^2_{21} = 7.65\times 10^{-5}{\rm eV}^2\,, \quad \Delta m^2_{31} = 2.4\times 10^{-3}{\rm eV}^2\,. \end{aligned} \tag{8.8}$$

We impose external 1σ errors on Δm^2_{21} (4%) and θ_{12} (4%) and on Δm^2_{31} (5%) and θ_{23} (5%) as conservative estimates for the current measurement errors [94]. We also include a 2% matter density uncertainty [95,96]. As shown in Fig. 8.1, we have the signal spectra of NH and IH for different $\delta_{\rm CP}$ for the ν_μ appearance channel of TASD at the neutrino factory. It should be comparable to Fig.2 in [49]. There is no shading area, since we do not take into account the errors of θ_{13}. The shape and peak are located in the similar way. As shown in Fig. 8.2, we scan the baseline dependence of the discovery reach of CPV and

MH at different $\sin^2 2\theta_{13}$, respectively. We find that there is no essential preference for the so-called bimagic baseline at 2540 km.

Our main observations can be summarized as follows:

- The optimal baseline choice depends on the performance indicator, long baselines are mostly preferred for the MH. Therefore, the conclusions in Ref. [49] imply that the MH was chosen as preferred performance indicator. Measuring CPV would clearly lead to a different baseline optimization.
- There is clear preference for using both muon polarities, which will lead to a much better absolute sensitivity.
- There is no particular preference for exactly this baseline value, for none of the performance indicators, in the sense of the "magic baseline" [22] where a clear, narrow dip can be seen in the numerical study. In addition, the "bimagic effect" cannot be clearly attributed to the particular suggested energy windows. For example, if one masks the bins around the bimagic energies (0.3 GeV windows around 1.9 and 3.3 GeV), the sensitivity is hardly affected.

We have tested that our observations do not rely on the true hierarchy, or the energy resolution of the detector.

In conclusion, it is a good choice to use a 2540 km baseline for the TASD if one wants to measure the MH as primary performance indicator. There is, however, no preference of this exact baseline value. Instead of 2540 km, a relatively wide baseline window between 2000 km and 3000 km is allowed for good physics performance studies. In addition, if CPV is considered as a most important indicator of neutrino factory, a different baseline optimization will be definitely preferred. We also do not find any reason to consider only one muon polarity, since both polarities fo beam will be produced in the target. Finally, it is hardly possible to name a bimagic baseline based on our analysis, since the physics statements are far from the motivations.

Chapter 9

Oscillations by three active plus one sterile neutrinos

There has been the exceptional LSND measurement with an incompatible anomaly [11]. The simplest interpretation has been an additional sterile neutrino added to the standard picture with $|\Delta m^2_{41}| \gg |\Delta m^2_{31}|$. A global fit to all experimental data, however, is not in favor to this hypothesis [12], which means that more exotic scenarios would be required to describe this anomaly, such as a decaying sterile neutrino [13]. The recent results from MiniBooNE, however, are consistent with sterile neutrino oscillations in the antineutrino sector [14]. Note that the LSND interpretation requires significant mixings with the active neutrinos, whereas small ad-mixtures, even if $|\Delta m^2_{41}| \gg |\Delta m^2_{31}|$, are not excluded. On the other hand, sterile neutrinos with $|\Delta m^2_{41}| \sim |\Delta m^2_{31}|$ or $|\Delta m^2_{41}| \sim \Delta m^2_{21}$, as they are motivated by a recent cosmological data analysis [15], have been hardly studied in the literature. Of course, such sterile neutrinos have to have small mixings with the active ones in order not to spoil the leading three-flavor fits. Therefore, we discuss sterile neutrinos beyond LSND, *i.e.*, without any constraints to Δm^2_{41} including the full range. We consider the simplest case of only one additional sterile neutrino. Note that we do not impose cosmological constraints on the sterile neutrino masses, but we assume that the masses are to be constrained in a self-consistent way with long-baseline experiments.

While earlier studies have constrained the active-sterile mixing in the short-baseline sector, or have focused on sterile neutrinos with a LSND-like mass splitting $\mathcal{O}(\mathrm{eV}^2)$ (see, *e.g.*, Refs. [1, 12, 101]), we cannot rely on constraints from the atmospheric and solar experiments, which need to be re-analyzed in a global fit for the presence of very light sterile neutrinos in a self-consistent way. Therefore, we consider the Neutrino Factory (NF), which allows for a self-consistent treatment.

9.1 Oscillation probabilities

The general evolution equation of flavor eigenstates in matter can be expressed as

$$i\frac{d}{dt}|\nu_\alpha\rangle = \mathcal{H}_{\alpha\beta}|\nu_\beta\rangle = \frac{1}{2E}(UD^2U^\dagger + \mathcal{A})|\nu_\beta\rangle\,, \tag{9.1}$$

where $D \equiv \mathrm{Diag}\{m_1, m_2, m_3, m_4\}$ is the diagonal mass matrix and $\mathcal{A} = \mathrm{Diag}\{a_e, 0, 0, -a_n\}$ is the matter potential with $a_e = 2\sqrt{2}EG_F n_e$ and $a_n = \sqrt{2}EG_F n_n$ (see, *e.g.*, Ref. [102] for details). Here n_e and n_n are the electron and neutron number density in matter, respectively, with $n_e \simeq n_n$ in Earth matter. Note that the neutral current matter effect may lead to additional matter-driven effects, which are not easy to capture in an analytical treatment. The perturbative solution of this equation depends on the Δ_{41}-regime. We will discuss different regimes separately.

At this time, the mixing matrix should be extended to four neutrinos. We will then make use of the following parametrization, as adopted in Ref. [12]:

$$U = R_{34}(\theta_{34},\, 0)\; R_{24}(\theta_{24},\, 0)\; R_{23}(\theta_{23},\, \delta_3)\; R_{14}(\theta_{14},\, 0)\; R_{13}(\theta_{13},\, \delta_2)\; R_{12}(\theta_{12},\, \delta_1)\,. \tag{9.2}$$

This parametrization has the following features:

- The standard PMNS matrix has to be recovered in the case of small new mixing angles; that fixes the order of the corresponding sub-sector rotations
- The phases are attached to the 12-, 13- and 23-rotations. Therefore, if one of the standard mixing angles can be rotated away in a particular measurement, the corresponding phase also automatically becomes unphysical.
- The order of the 34-24-14-rotations is arbitrary. We choose the 34-angle as the left-most one, which makes it hardest to observe (it affects the ν_τ-ν_s-mixing). Changing the order here does not change the fact that one of the rotations is difficult to extract.

9.1.1 Very short baseline

If we do expansion by $\eta_2\,, \eta_3$ up to $\mathcal{O}(\eta_i^0)$ for all channels with $\Delta \equiv \frac{\Delta m_{41}^2}{4E}L$, we arrive at:

$$\mathcal{P}_{e\mu} = 4c_{14}^2 s_{14}^2 s_{24}^2 \sin^2(\Delta) \tag{9.3}$$
$$\mathcal{P}_{e\tau} = 4c_{14}^2 c_{24}^2 s_{14}^2 s_{34}^2 \sin^2(\Delta) \tag{9.4}$$
$$\mathcal{P}_{es} = 4c_{14}^2 c_{24}^2 c_{34}^2 s_{14}^2 \sin^2(\Delta) \tag{9.5}$$
$$\mathcal{P}_{ee} = 1 - \sin^2(2\theta_{14}) \sin^2(\Delta) \tag{9.6}$$
$$\mathcal{P}_{\mu e} = 4c_{14}^2 s_{14}^2 s_{24}^2 \sin^2(\Delta) \tag{9.7}$$
$$\mathcal{P}_{\mu\tau} = 4c_{14}^4 c_{24}^2 s_{24}^2 s_{34}^2 \sin^2(\Delta) \tag{9.8}$$
$$\mathcal{P}_{\mu s} = 4c_{14}^4 c_{24}^2 c_{34}^2 s_{24}^2 \sin^2(\Delta) \tag{9.9}$$
$$\mathcal{P}_{\mu\mu} = 1 - c_{14}^2 s_{24}^2 \left[3 + 2c_{14}^2 \cos(2\theta_{24}) - \cos(2\theta_{14})\right] \sin^2(\Delta) \tag{9.10}$$

If we consider $\mathcal{P}_{e\mu} + \mathcal{P}_{e\tau} + \mathcal{P}_{es} + \mathcal{P}_{ee}$ and $\mathcal{P}_{\mu e} + \mathcal{P}_{\mu\tau} + \mathcal{P}_{\mu s} + \mathcal{P}_{\mu\mu}$, the unitarity requires them to be 1. Actually, we check this resummation and the unitarity recovers very well. It has to be noted that all results presented here are generated by an automatic mathematica program, even though it takes a while. Therefore, all can be easily reproduced if a new convenient parameterization is chosen.

Note that the neutral current rate is proportional to $1-\mathcal{P}_{es}$ for electron neutrinos at the source, and $1-\mathcal{P}_{\mu s}$ for muon neutrinos at the source. These probabilities correspond to the near detector limit at the Neutrino Factory, where the baseline depends on the sensitive $|\Delta m^2_{41}|$. For example, at $d \simeq 18\,\mathrm{km}$, one has optimal sensitivity for $|\Delta m^2_{41}| \sim 1\,\mathrm{eV}^2$, whereas at $d \simeq 1.5\,\mathrm{km}$, one has optimal sensitivity for $|\Delta m^2_{41}| \sim 10\,\mathrm{eV}^2$ with the 25 GeV Neutrino Factory (*cf.*, Fig. 2 in Ref. [103]). Here d is the distance to the end of the decay straight, which is related to an effective baseline $L_{\mathrm{eff}} = \sqrt{d(d+s)}$ with s the length of the decay straight if the decays are averaged over the straight [32].

9.1.2 Intermediate baseline

As for the intermediate baselines, we have to include two-mass scale dominance results. In the two-mass dominance approximation, they are:

$$\begin{aligned}
&\mathcal{P}_{e\mu} = 4c^2_{14}s^2_{14}s^2_{24}\sin^2(\Delta) \\
&+ (\Delta\eta_3)\sin(\Delta)\left[2c^2_{14}s_{14}s_{23}\sin(2\theta_{13})\sin(2\theta_{24})\cos(\Delta-\delta_2+\delta_3) - 2s^2_{13}s^2_{24}\cos(\Delta)\sin^2(2\theta_{14})\right]
\end{aligned} \tag{9.11}$$

$$\begin{aligned}
&\mathcal{P}_{e\tau} = 4c^2_{24}c^2_{14}s^2_{14}s^2_{34}\sin^2(\Delta) \\
&+ 4c_{24}c^2_{14}s_{14}s_{34}(\Delta\eta_3)\{\sin(2\theta_{13})\left[c_{23}c_{34}\cos(\Delta-\delta_2) - s_{23}s_{24}s_{34}\cos(\Delta-\delta_2+\delta_3)\right]\sin(\Delta) \\
&- c_{24}s^2_{13}s_{14}s_{34}\sin(2\Delta)\}
\end{aligned} \tag{9.12}$$

$$\begin{aligned}
&\mathcal{P}_{\mu\tau} = 4c^4_{14}c^2_{24}s^2_{24}s^2_{34}\sin^2(\Delta) \\
&+ c_{24}c^2_{14}s_{24}s_{34}(\Delta\eta_3)\{8c_{13}c_{23}c_{34}\left[c_{13}c_{24}s_{23}\cos(\Delta-\delta_3) - s_{13}s_{14}s_{24}\cos(\Delta-\delta_2)\right]\sin(\Delta) \\
&- 2s_{34}\left(c^2_{13}s^2_{23} - s^2_{13}s^2_{14}\right)\sin(2\theta_{24})\sin(2\Delta) \\
&- 2s_{14}s_{23}s_{34}\sin(2\theta_{13})\left[\cos(\delta_2-\delta_3)\sin(2\Delta)\cos(2\theta_{24}) - 2\sin(\delta_2-\delta_3)\sin^2(\Delta)\right]\}
\end{aligned} \tag{9.13}$$

9.2 Mass schemes

We study the constraints to the general four neutrino scheme without any assumptions at the Neutrino Factory. While the global fits imply the mixings between active and sterile neutrinos must be small, the four neutrino scheme has to recover the standard picture once we switch off the small mixings between active and sterile neutrinos. The four neutrino schemes can be categorized into two different classes: the 2+2 scheme, in which the solar and atmospheric mass squared splittings are separated by a new splitting, and the 3+1 scheme, in which the new mass eigenstate is added somewhere to the existing mass pattern. The 2+2 scheme is, at least for an LSND-like new mass squared splitting, strongly disfavored by global fits [76,105]. The 3+1 scheme, on the other hand, naturally recovers the standard picture in the case of small mixings. Therefore, naturally, we consider the 3+1 scheme only. We show the possible mass ordering of four neutrino eigenstates in

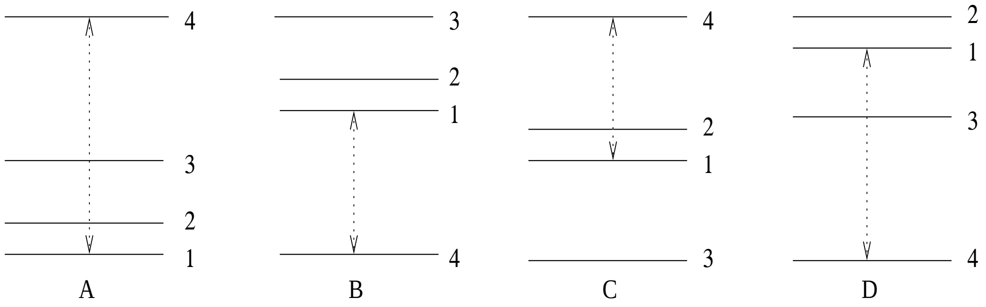

Figure 9.1: *The mass ordering of four neutrino eigenstates (not to scale). The arrow illustrates the new characteristic mass squared difference* Δm^2_{41}*. The four different scenarios correspond to* $\Delta m^2_{31} > 0$, $\Delta m^2_{41} > 0$ *(A),* $\Delta m^2_{31} > 0$, $\Delta m^2_{41} < 0$ *(B),* $\Delta m^2_{31} < 0$, $\Delta m^2_{41} > 0$ *(C), and* $\Delta m^2_{31} < 0$, $\Delta m^2_{41} < 0$ *(D). The figure is taken from [104].*

Fig. 9.1. The arrow illustrates the new characteristic mass squared difference Δm^2_{41}. The four different scenarios correspond to $\Delta m^2_{31} > 0$, $\Delta m^2_{41} > 0$ (A), $\Delta m^2_{31} > 0$, $\Delta m^2_{41} < 0$ (B), $\Delta m^2_{31} < 0$, $\Delta m^2_{41} > 0$ (C), and $\Delta m^2_{31} < 0$, $\Delta m^2_{41} < 0$ (D). Unless noted explicitly, we show the results for scenario (A).

9.3 Generalized exclusion limits

In this section, we discuss general constraints to the new mixing angles θ_{14}, θ_{24}, and θ_{34}, and the additional mass squared difference Δm^2_{41} *without any additional assumptions.* In particular, we do not assume that Δm^2_{41} is in a particular range, such as the LSND-motivated one which leads to averaging at the long baselines. In addition, we do not assume that some of the not shown parameters take particular fixed values.

As performance indicator, we use the sensitivity to θ_{ij} similar to the CHOOZ limit for the θ_{13}-Δm^2_{31} plane. We compute the simulated rates with $\theta_{14} = \theta_{24} = \theta_{34} = 0$ and $\Delta m^2_{41} = 0$, corresponding to the hypothesis of no effect of an additional sterile neutrino. Then we can discuss several exclusion limits for the new mixing angles, with the unknown parameters marginalized over. The exclusion limit for each new mixing angle will, in general, depend on Δm^2_{41} similar to the CHOOZ limit. Therefore, we show three different exclusion planes θ_{i4}-Δm^2_{41}. Note that the sensitivity for any combination θ_{i4}-θ_{k4} $(i \neq k)$ will typically vanish, since Δm^2_{41} is marginalized over. For a comparison to the existing literature, see the next section.

The exclusion limit for $\sin^2 2\theta_{i4}$–$\Delta m^2_{41} (i = 1, 2, 3)$ (region on the right-hand side of curves excluded). Let us first of all discuss the effect of the near detectors separately (thick dashed curves). Obviously, the main sensitivity is obtained at about $\Delta m^2_{41} \simeq 10\,\mathrm{eV}^2$, which comes from the distance chosen for the near detectors. By changing the near detector locations, the position of the main peak can be controlled. If required by the recent MiniBooNE results, a longer baseline than 2 km may have to be chosen. The main sensitivity to θ_{14} comes from electron neutrino (antineutrino) disappearance and the main

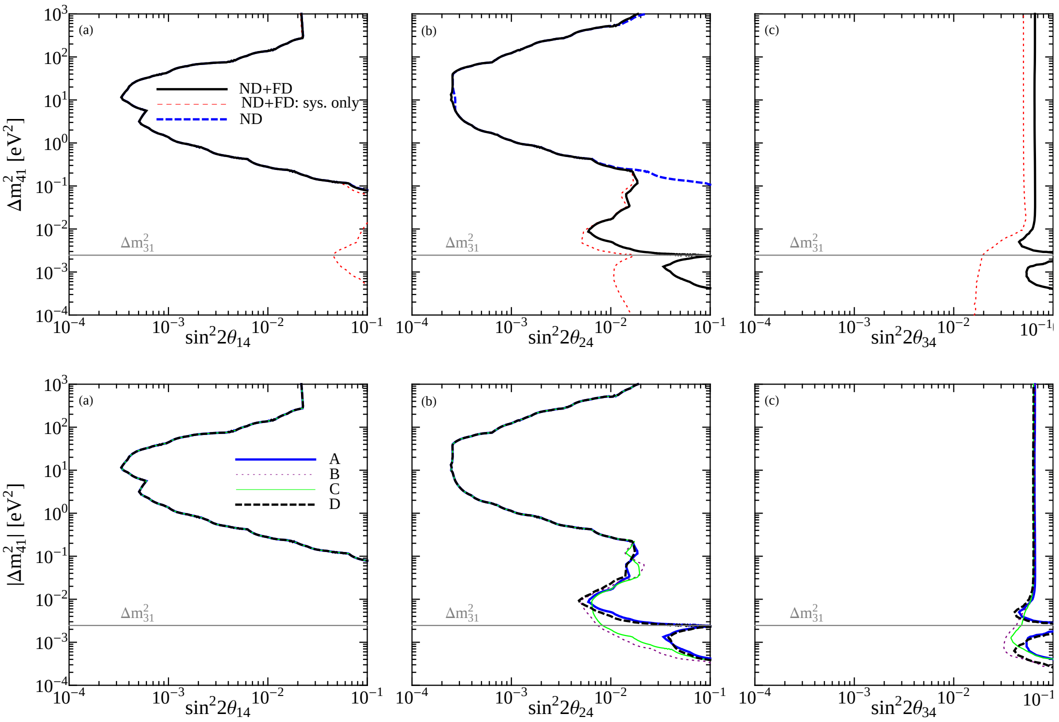

Figure 9.2: *The exclusion limit for* $\sin^2 2\theta_{i4}$–$\Delta m^2_{41} (i = 1, 2, 3)$ *(region on the right-hand side of curves excluded). The upper panel shows the results with or without mixing angle correlations, including a ND setup and a combination of ND and FD. The lower panel gives results of the standard IDS-NF (*4000 *km and* 7500 *km) setup with detectors for the four different mass orderings in Fig. 9.1; 90% CL (2 d.o.f.).*

sensitivity to θ_{24} from muon neutrino (antineutrino) disappearance. Since the efficiencies for muon neutrino detection are typically better, the sensitivity to θ_{24} is slightly better than that to θ_{14} for our assumptions. As expected, there is no sensitivity to θ_{34} coming from the near detectors, because the ν_τ disappearance channel does not exist.

To illustrate the effect from different mass orderings, as shown in Fig. 9.1, we display these figures for the standard IDS-NF (4000 km and 7500 km) setup in combination with near detectors in Fig. 9.2. Note that only the absolute value of the new mass squared difference is shown at the vertical axes. The upper peak hardly depends on the mass ordering. The lower (long-baseline) peak, which is only present in the middle and right panels, somewhat depends on the mass ordering. We identify two qualitatively different cases: In schemes A and D, the sensitivity is destroyed just at the value of Δm^2_{31}. In these cases, *cf.*, Fig. 9.1, mass eigenstates 3 and 4 are on top of each other, which means that there is no additional mass squared difference. The parameter correlations (marginalization over the unknown parameters) then destroy the sensitivity because the new mixing angles cannot be disentangled, in spite of the additional neutral current matter effect. This is different for schemes B and C, for which mass eigenstate 4 is on the opposite site of mass eigenstate 3. Although the absolute values of Δm^2_{41} and Δm^2_{31} are similar,

Δm_{41}^2 [eV^2]	$\sin^2 2\theta_{14}$	$\sin^2 2\theta_{24}$	$\sin^2 2\theta_{34}$	$\theta_{14}[°]$	$\theta_{24}[°]$	$\theta_{34}[°]$
0.001	0.403	0.029	0.042	19.7	4.9	5.9
0.01	0.224	0.004	0.044	14.1	1.9	6.1
0.1	0.054	0.013	0.047	6.7	3.3	6.3
1	0.001	0.0009	0.047	0.9	0.8	6.3
10	0.0002	0.0002	0.047	0.5	0.5	6.3
100	0.0043	0.0006	0.047	1.9	0.7	6.3
1000	0.0168	0.015	0.047	3.7	3.5	6.3

Table 9.1: *Exclusion limits (90% CL, 1 d.o.f.) for several selected (fixed) values of* Δm_{41}^2*. Mass ordering A assumed. The simulation includes both near and far detectors.*

these mass squared differences have different signs leading to different (charged current) matter effects.

9.4 Exclusion limits with special assumptions

Here we compare our analysis with different approaches in the literature under special assumptions. The most common assumption for sterile neutrino bounds at the long baselines is $|\Delta m_{41}^2| \sim \mathcal{O}(1)$ eV^2, as motivated by LSND, which leads to averaging over the fast Δm_{31}^2 at the long baselines. Another assumption, which we have found in Ref. [106], is $\Delta m_{41}^2 \to 0$. The third case we consider is the two-flavor short-baseline limit. These examples are particularly useful to discuss some subtleties when short- and long-baseline results are to be combined. Note that, for the comparison to the existing literature, we use studies which use the same parametrization of the four neutrino mixing matrix as ours for the sake of simplicity.

9.4.1 LSND-motivated Δm_{41}^2

The first assumption, which we test, is an LSND-motivated Δm_{41}^2. In general, we assume that $|\Delta m_{41}^2| \gg |\Delta m_{31}^2|$, which leads to the averaging of the fast oscillations at the long baselines. This limit is frequently used for the discussion of long baselines only, *i.e.*, without near detectors, since oscillation effects may be present in the near detectors.

We show in Fig. 9.3 an example for such an analysis using the far detectors only (thick solid curve), which is to be compared with Fig. 9 in Ref. [93] for slightly different parameter values (here the simulated $\theta_{14} = 0$). For comparison, the current bound is shown (*cf.*, Fig. 2 in Ref. [107]). One can easily see that the Neutrino Factory could improve the current bounds on θ_{24} and θ_{34} by a factor of a few if $|\Delta m_{41}^2|$ is assumed to be large. Note, however, that the marginalization over Δm_{41}^2 would lead to vanishing sensitivity. If the (thick dashed) curve with only systematics is considered, the cross terms in the long-baseline probabilities as in $\mathcal{P}_{\mu\mu}$, are switched off, and result improves along

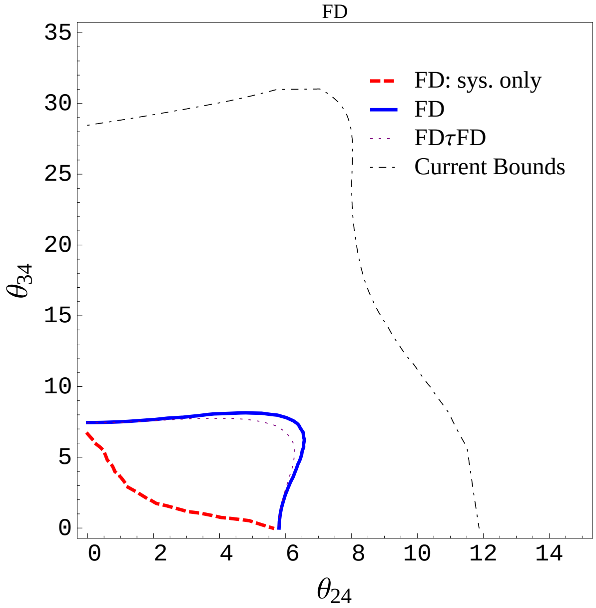

Figure 9.3: *The exclusion limit for θ_{24}–θ_{34} in degrees (90% CL, 2 d.o.f.), where $|\Delta m^2_{41}| \gg |\Delta m^2_{31}|$. We show the result for the IDS-NF setup (*4000 *km and* 7500 *km) using far detectors only (thick solid curve). The thick dashed curve corresponds to the result without correlations (systematics only), the dotted curve the result including a ν_τ detector at* 4000 *km. In addition, the current bounds are shown (from Ref. [107]). The figure is taken from [104].*

the diagonal. Such cross terms are also present in $\mathcal{P}_{\mu\tau}$, sometimes called the "discovery channel" [93], which leads to a slight improvement if an additional ν_τ detector at the intermediate baseline is used (thin dotted curve). However, as we noted above, the main effect on θ_{34} comes from the disappearance channels, especially of the very long (7500 km) baseline.

Let us now test the impact of additional near detectors on this scenario. Obviously, we have to be careful, because a $\Delta m^2_{41} \sim 1\,\mathrm{eV}^2$ might cause observable effects in the near detectors, and, in principle, we also have to marginalize over Δm^2_{41}. We especially expect some impact on the measurement of θ_{24} by the muon neutrino disappearance channel. If we fix $\Delta m^2_{41} = 1\,\mathrm{eV}^2$, we find considerably better sensitivity including the near detectors, compare the dashed-dotted curve (without near detectors) with the thick dashed curves. However, note that the marginalization over Δm^2_{41} will in this case destroy the sensitivity again. This problem can be circumvented by additional assumptions. Consider, for instance, a non-zero value of $\sin^2 2\theta_{14}$ chosen by Nature. Then Δm^2_{41} can be actually measured by $\mathcal{P}_{ee}$ in the near detectors, and the marginalization over Δm^2_{41} can be performed. In this case, the impact of the Δm^2_{41} marginalization is small, as it can be seen from the comparison between the thick dashed and thick solid curves. Another plausible assumption may be that Δm^2_{41} is so large that the effect even averages out in the near detectors. Therefore, we show the thin dotted curve for a KeV sterile neutrino with

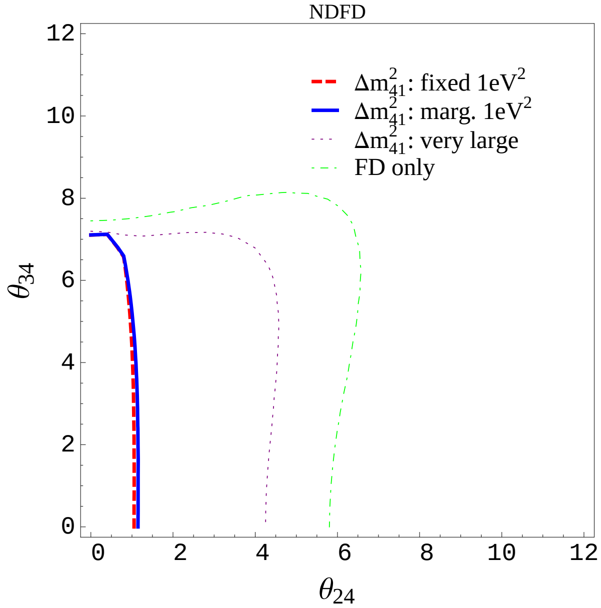

Figure 9.4: *The exclusion limit for* θ_{24}*–*θ_{34} *in degrees (90% CL, 2 d.o.f.), where* $|\Delta m^2_{41}| \gg |\Delta m^2_{31}|$*. Compared to Fig. 9.3, additional near detectors at 2 km are used. This leads to the dependence on the assumptions for* Δm^2_{41} *(and* $\sin^2 2\theta_{14}$*), as given in the plot legend (see main text for details). Here "very large* Δm^2_{41}*" means that the oscillations average out already at the near detectors, such as for keV sterile neutrinos. Here we assume* $\sin^2 2\theta_{14} = 0.01$ *for the curves including near detectors. Note that the dashed-dotted curve corresponds to the thick solid curve in Fig. 9.3. The figure is taken from [104].*

$\Delta m^2_{41} = 10^6\,\mathrm{eV}^2$, which is sufficiently large. Here the near detectors somewhat improve the sensitivity compared to the no near detector case, but the effect is not as large as for the $\Delta m^2_{41} \sim 1\,\mathrm{eV}^2$, $\sin^2 2\theta_{14} = 0.01$ case. The purpose of this example is to illustrate that any combined fit of two new parameters not including Δm^2_{41}, such as the one in Fig. 9.3, face subtleties if near and far detectors are combined. Typically, additional assumptions are needed, and the interpretation of the results becomes assumption-dependent. This is in contrast to the figures in the previous section, which do not depend on assumptions.

A similar analysis is performed in Ref. [106] by the MINOS collaboration. The mixing matrix parametrization in this reference is equivalent to ours since they fix their δ_2, corresponding to our δ_1, to zero. One of the schemes tested in Ref. [106] assumed that $|\Delta m^2_{41}| \gg |\Delta m^2_{31}|$ (in mass ordering A). We show their result for the combined fits in the θ_{34}–θ_{24} (a), θ_{23}–θ_{24} (b), and θ_{34}–θ_{23} (c) planes in Fig. 9.5. Note that the not shown parameters are fixed, such as $\theta_{14} = 0$ and the phases, and that θ_{13} is fixed to two different values (not marginalized over). The best-fit values are also marked. We also show the results for the Neutrino Factory under the same assumptions, where we use the 4000 km baseline only. Obviously, the Neutrino Factory would reduce the allowed parameter space significantly, especially if θ_{13} is large. Again, note that some of the parameters are fixed here, and the full marginalization would destroy the sensitivities. The impact of additional

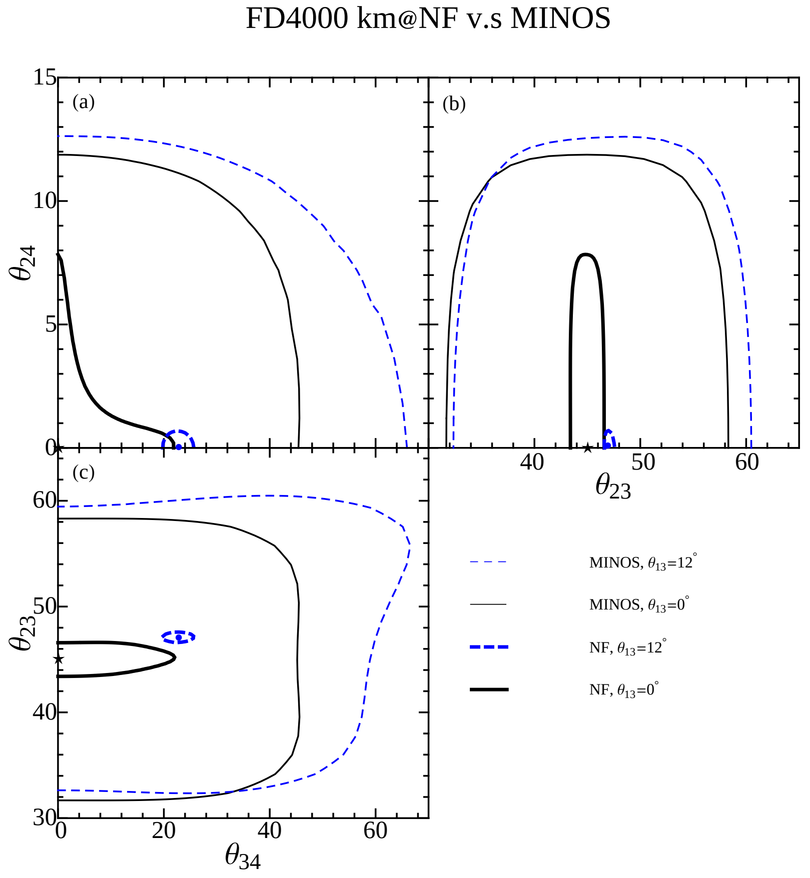

Figure 9.5: *Exclusion limits in the* θ_{34}*–*θ_{24} *(a),* θ_{23}*–*θ_{24} *(b), and* θ_{34}*–*θ_{23} *(c) planes at the 90% CL. The different curves correspond to MINOS and the Neutrino Factory (NF) with* $\Delta m^2_{41} = 1\ eV^2$*. Here only one NF far detector at 4000 km is used (without near detectors). All contours represent* 90% *confidence level. The solid curves assume* $\theta_{13} = 0°$*, while the dashed curves assume* $\theta_{13} = 12°$*. The best-fit values are marked in the figure, the one of* θ_{24} *is zero. The MINOS curves are taken from Ref. [106]. The figure is taken from [104].*

near detectors, which are especially sensitive to θ_{24}, and an additional far detector at 7500 km, which is sensitive to θ_{34}, is shown in Fig. 9.6. Here the NF contours for large $\theta_{13} = 12°$ almost shrink to points, and are hardly visible anymore. In this figure, $\Delta m^2_{41} = 1\,\mathrm{eV}^2$ is assumed, and Δm^2_{41} is not marginalized over. For such a value of Δm^2_{41}, we would also expect a small effect in the MINOS near detector, which is, however, not considered in Ref. [106].

9.4.2 The special case $\Delta m^2_{41} \to 0$

As similar kind of analysis can be performed in the special case $\Delta m^2_{41} \to 0$, for which also no additional mass squared difference appears and $m_1 = m_4$. In this case, we have some sensitivity to θ_{34} in $\mathcal{P}_{\mu\mu}$. The comparison between MINOS and the Neutrino

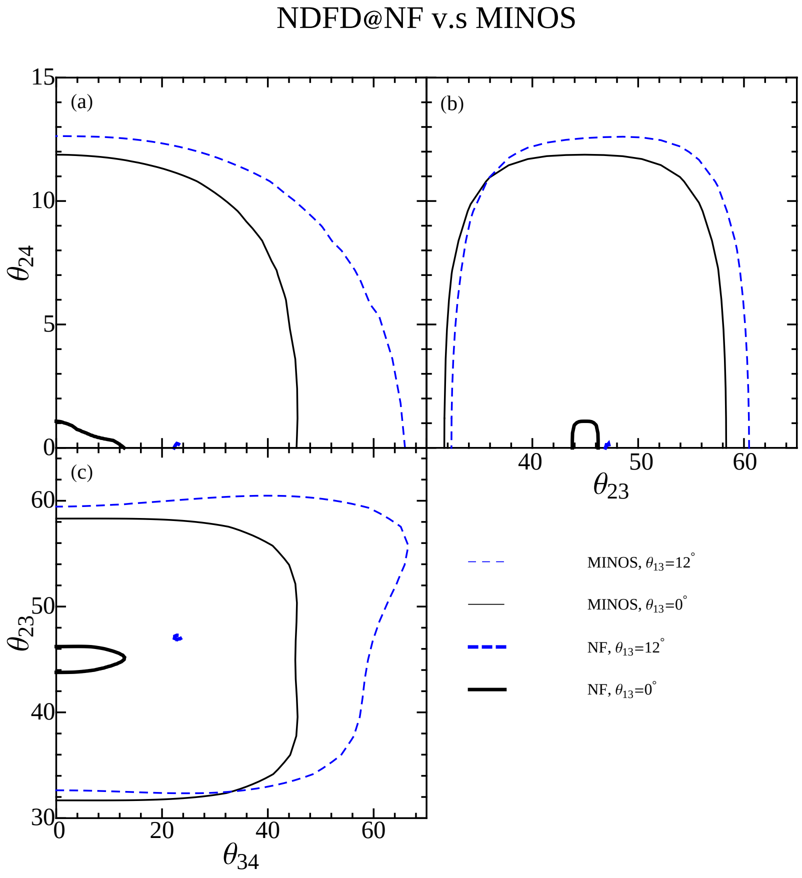
NDFD@NF v.s MINOS

Figure 9.6: *Same as Fig. 9.5, but additional far detector at 7500 km and near detectors at 2 km included. The NF contours for large* $\theta_{13} = 12^\circ$ *almost shrink to points. The figure is taken from [104].*

Factory is shown for this special case in Fig. 9.7, and again the Neutrino Factory has an excellent sensitivity. The marginalization over Δm_{41}^2 and the other parameters will, however, destroy the sensitivity to θ_{34}, since there is no sensitivity in Fig. 9.2 for $\Delta m_{41}^2 \rightarrow 0$. This is another good example that the set of assumptions determines the outcome, whereas the general analysis would simply produce no sensitivity.

We have discussed sterile neutrinos beyond LSND, *i.e.*, sterile neutrinos with small active-sterile mixings and an arbitrary Δm_{41}^2. We have used the Neutrino Factory for the simulation, since this experiment can be used for a self-consistent approach including near and far detectors. We have used the simplest possible hypothesis, namely one extra sterile neutrino in a 3+1-like scheme in which the standard scenario is recovered for small active-sterile mixing angles. While we obtain the expected sensitivity to the active-sterile mixing in the large LSND-motivated $|\Delta m_{41}^2| \gtrsim 1\,\mathrm{eV}^2$ region, we also find sensitivity close to the atmospheric Δm_{31}^2. We have pointed out that there are no global fits for this case yet, and a re-analysis of atmospheric and solar data should demonstrate what we can learn for $\Delta m_{41}^2 \ll 1\,\mathrm{eV}^2$. Note that recent cosmological fits point towards one or two such

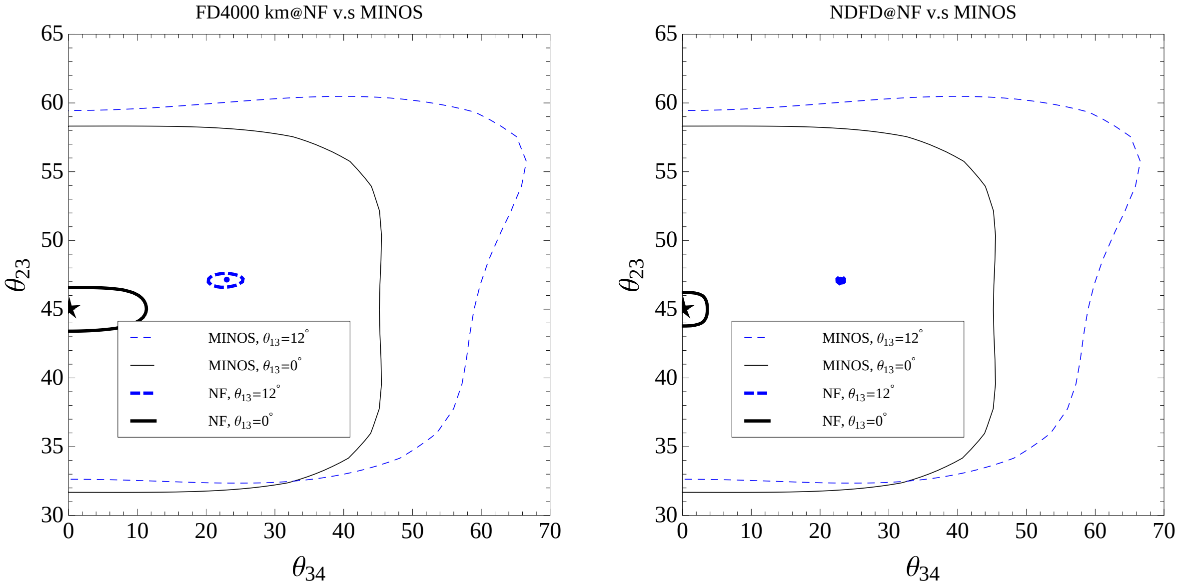

Figure 9.7: *Exclusion limits in the* θ_{34}–θ_{23} *plane at the 90% CL. The different curves correspond to MINOS and the Neutrino Factory (NF) with* $\Delta m^2_{41} = 0$ *eV*^{2}*. Here only one NF far detector at 4000 km is used (without near detectors) in the left panel, whereas in the right panel two long-baseline detectors at 4000 km and 7500 km together with the near detectors at 2 km are included. The solid curves assume* $\theta_{13} = 0°$*, while the dashed curves assume* $\theta_{13} = 12°$*. The best-fit values are marked in the figure, the one of* θ_{24} *is zero. The MINOS curves are taken from Ref. [106] and curves for neutrino factory are taken from [104].*

light sterile neutrinos [15].

Here gives a short summary. We have demonstrated that, especially at the short baselines, the disappearance channels are the primary channels of interest for light sterile neutrino constraints, no matter if a parametrization-independent approach or a particular parametrization for the mixing matrix is used. For the combined analysis of short and long baselines including charged and neutral current matter effects, however, we have used a particular parametrization. We have demonstrated that the most general constraint on sterile species can be shown as exclusion limits in the θ_{i4}–Δm^2_{41}–planes ($i = 1, 2, 3$), similar to the CHOOZ limit for θ_{13}–Δm^2_{31}. The Neutrino Factory turns out to have excellent sensitivity to the three mixing angles in a wide range of Δm^2_{41}. However, one of the three mixing angles (θ_{14} in our parametrization) can only be very well measured for large $|\Delta m^2_{41}| \gtrsim 1\,\mathrm{eV}^2$ at the near detectors, and one (θ_{34} in our parametrization) better for small $|\Delta m^2_{41}| \sim |\Delta m^2_{31}|$, whereas the third ($\theta_{24}$) can be measured in the combined range. An electron neutrino disappearance channel at the long baselines could solve this problem for θ_{14}, which is, however, difficult at the Neutrino Factory, because electron charge identification might be required. An improved measurement of θ_{34} for large $|\Delta m^2_{41}| \gtrsim 1\,\mathrm{eV}^2$ would require a hypothetical ν_τ disappearance channel. We have also investigated the impact of different mass orderings as shown in Fig. 9.1 on the sensitivities. We have found that there is a qualitative difference between the cases $\Delta m^2_{31} \sim \Delta m^2_{41}$ and $\Delta m^2_{31} \sim -\Delta m^2_{41}$ due to different matter effects. Furthermore, we have tested the impact of additional ν_τ detectors with an aggressive 10 kt OPERA-like detector at the short and long baselines, and we have not found any significant effect on the sensitivities.

Apart from the general constraints, we have compared our analysis to special cases in the literature. For instance, we have tested the case $|\Delta m^2_{41}| \gtrsim 1\,\mathrm{eV}^2$ leading to averaging of the fast oscillations at the long baselines. We have looked into the special case of a θ_{24}-θ_{34} fit. We have shown that this assumption involves subtleties, especially if additional near detectors are considered, because the assumption for Δm^2_{41} implies that there may be effects in the near detectors. We have illustrated that in this case additional assumptions are required, and the interpretation of the sensitivities becomes strongly assumption-dependent. This does not apply to our general bounds we discussed above. We have also tested the impact of ν_τ detection ("discovery channel"), and we could find a marginal improvement. The main sensitivity, however, comes from the muon neutrino disappearance channel for $E_\mu = 25\,\mathrm{GeV}$. We have moreover compared the Neutrino Factory to a recent MINOS analysis using the same assumptions, and we have found excellent sensitivities. However, including the full marginalization over the unknown parameters, the sensitivities were basically destroyed.

Chapter 10

Summary and outlook

We have introduced the basic knowledge of neutrino oscillations in theory and reproduced the perturbative oscillation probabilities which are frequently used in the literature. Based on two different methods, we have discussed their valid energy ranges under a certain circumstance. We have demonstrated that these approximations of oscillation probabilities are able to provide useful clues of neutrino oscillation channels for future's design of experiments. In addition, we have briefly reviewed the current status of neutrino oscillation experiments so far and summarized their global results in terms of three-neutrino oscillation analysis. Neutrino sources, detections and how to extract useful information of oscillation parameters in the Earth-based experiments have also been included there. Then we have approached the design study of the neutrino factory so far and reported recent progress within the collaboration group.

We have studied the phenomenology of neutrino oscillations at a neutrino factory in four different parts. One is about the physics study with near detectors at the neutrino factory. The other is about the reoptimization of baseline and beam energy for the neutrino factory in terms of the updated descriptions of MIND. Another is to clarify the concept of the low-energy neutrino factory and figure out the minimal requirements to achieve the physics goals. At last, it is about the searching for sterile neutrino in terms of a combination of previous proposed near detectors and traditional far detectors. The main conclusions are listed in the following:

First, we have proposed near detector setups to cancel the systematic uncertainties with regard to the cross sections, flux normalizations and the background uncertainties. We have demonstrated that near detectors are required for precision measurements. We have argued how many near detectors are needed and what the role of the flux monitoring is by near detectors. We have found that near detectors play an important role in the measurements of leading atmospheric parameters if the neutrino factory has only one baseline, whereas systematic uncertainties partially cancel in terms of near detectors.

Second, we have reoptimized the baseline and beam energy of the neutrino factory in light of the latest Monte Carlo simulations of MIND. In addition, the potential effects of τ decays come from oscillation channels $\nu_\mu \to \nu_\tau$ or $\nu_e \to \nu_\tau$, which is ignored in the early study. We have also taken them into account based on the physics performance of discovery reach of mass hierarchy, CP violation, and θ_{13}. We figure out that the effects of these τ decays are negligible for MIND. For the baseline and beam energy optimization for small $\sin^2 2\theta_{13}$, we have recovered the similar results with earlier simulations of the MIND detector. We find optimal baselines of about 2 500 km to 5 000 km for the CP violation measurement, where the beam energy of E_μ as low as about 12 GeV may be possible. However, for large $\sin^2 2\theta_{13}$, we show that the lower threshold and the backgrounds reconstructed at lower energies allow in fact for muon energies as low as 5 GeV at a shorter baseline, such as FNAL-Homestake. We have discovered that with the latest MIND analysis, low- and high-energy versions of the Neutrino Factory are just two different versions of the same experiment optimized for different parts of the parameter space.

Third, we have proposed that a detector designed for the low energy neutrino factory may be used off-axis in a high energy neutrino factory beam. We have found that for large θ_{13} (θ_{13} discovered by the next generation of experiments), a low energy neutrino factory might be the most plausible minimal version to test the unknown parameters. However, if a higher muon energy is needed for new physics searches, a high energy version including an off-axis detector may be an interesting alternative. For small θ_{13} (θ_{13} not discovered by the next generation), a high energy neutrino factory is preferred. Apart from that, we have briefly commented on the idea of using the bi-magic baseline to do the low-energy neutrino factory. We have demonstrated there is no preference towards this baseline setup in terms of the CP violation searches.

Finally, we have discussed effects of three active neutrinos plus one additional sterile neutrino with arbitrary mass at the high energy neutrino factory with near detectors. We have demonstrates a combination of short and long baseline setup provides good sensitivities, especially that near detectors could show the expected sensitivity at the LSND-motivated Δm^2_{41}-range, while some sensitivity can also be obtained in the region of the atmospheric mass splitting from the long baselines.

The proposed neutrino factory is the most powerful tool to carry out precision measurements of neutrino oscillation parameters so far. It is not only because the neutrino factory could perform standard three generation active neutrino physics, but also because it can tell us the story beyond three flavor neutrino oscillation physics, such as unitarity violations of the mixing matrix and non-standard interactions during neutrino productions, propagation in matter, or detections. What happens if there are both active and sterile neutrinos? Does it change the allowed fit values from oscillation experiments and direct lepton decays? The interference between them will lead to new phenomena in neutrino oscillation physics. Of course, more flavor neutrinos will always bring in more mixing angles, CP phases and mass squared differences. Their pollutions at the standard measurements should also be included and discriminated. Moreover, it is also interesting to keep a connection of neutrino oscillation physics and lepton flavor violation processes such $\mu \to e\gamma$. Last but not least, could neutrinos open a new window in geophysics since neutrinos can produced by fusions in the sun and beta decays of the nuclei in the earth? We expect further detailed studies to present applications of neutrino oscillations in geophysics.

Appendices

11.1 Details of perturbative expansions of oscillation probabilities

Here we provide some details of perturbative derivations at the neutrino oscillation probability shown in the Chapter 2. Under the condition of $\Delta m^2_{21} \ll \Delta m^2_{31}$ and the matter induced term $a \equiv 2EV_{CC} \ll \Delta m^2_{31}$, we obtain the following transition matrix element in the section 2.2.1:

$$
\begin{aligned}
S_0(x)_{\beta\alpha} &= \left\{ U\mathrm{exp}\left(-i\tfrac{x}{2E} \begin{bmatrix} 0 & 0 & 0 \\ 0 & 0 & 0 \\ 0 & 0 & \Delta m^2_{31} \end{bmatrix} \right) U^\dagger \right\}_{\beta\alpha} \\
&= U_{\beta i} \begin{bmatrix} 1 & 0 & 0 \\ 0 & 1 & 0 \\ 0 & 0 & \exp(-i\frac{\Delta m^2_{31}\cdot x}{2E}) \end{bmatrix}_{ij} U^\dagger_{j\alpha} \\
&= \textstyle\sum_i U_{\beta i}U^\dagger_{i\beta} + U_{\beta 3}U^*_{\alpha 3}\left[\exp(-i\frac{\Delta m^2_{31}\cdot x}{2E}) - 1\right] \\
&= \delta_{\beta\alpha} + U_{\beta 3}U^*_{\alpha 3}\left[\exp(-i\frac{\Delta m^2_{31}\cdot x}{2E}) - 1\right] \qquad (11.1)
\end{aligned}
$$

$$
\begin{aligned}
S_1(x)_{\beta\alpha} &= e^{-i\mathcal{H}_0 x}(-i)\textstyle\int_0^x dt\mathcal{H}_I(t) \\
&= (-i)\textstyle\int_0^x dt\left[e^{-i\mathcal{H}_0(x-t)}\mathcal{H}_I e^{-i\mathcal{H}_0 t}\right]_{\beta\alpha} \\
&= (-i)\textstyle\int_0^x dtU_{\beta i} \begin{bmatrix} 1 & 0 & 0 \\ 0 & 1 & 0 \\ 0 & 0 & \exp(-i\frac{\Delta m^2_{31}}{2E}(x-t)) \end{bmatrix}_{ij} U^*_{\gamma\eta}U_{\eta k} \begin{bmatrix} 1 & 0 & 0 \\ 0 & 1 & 0 \\ 0 & 0 & \exp(-i\frac{\Delta m^2_{31}}{2E}t) \end{bmatrix}_{kl} U^*_{\alpha l} \\
&= (-i)U_{\beta i}U^*_{\gamma i}(\mathcal{H}_I)_{\gamma\eta}U_{\eta k}U^*_{\alpha k}\left[\textstyle\int_0^x dte^{-i\frac{\Delta m^2_{31}}{2E}[(x-t)\delta_{i3}+t\delta_{k3}]}\right] \qquad (11.2)
\end{aligned}
$$

with

$$
\begin{aligned}
U^*_{\gamma i}(\mathcal{H}_I)_{\gamma\eta}U_{\eta k} &= \tfrac{1}{2E}\left(\begin{bmatrix} 0 & 0 & 0 \\ 0 & \Delta m^2_{21} & 0 \\ 0 & 0 & 0 \end{bmatrix} + U^\dagger \begin{bmatrix} a & 0 & 0 \\ 0 & 0 & 0 \\ 0 & 0 & 0 \end{bmatrix} U \right)_{ik} \\
&= \tfrac{\Delta m^2_{21}}{2E}\delta_{i2}\delta_{k2} + \tfrac{a}{2E}U^*_{ei}U_{ek} \qquad (11.3)
\end{aligned}
$$

$$\begin{aligned}
&\int_0^x dte^{-i\frac{\Delta m_{31}^2}{2E}[(x-t)\delta_{i3}+t\delta_{k3}]} \\
=&\delta_{i3}\delta_{k3}xe^{-i\frac{\Delta m_{31}^2\cdot x}{2E}} + \left[(1-\delta_{i3})\delta_{k3}+\delta_{i3}(1-\delta_{k3})\right]\frac{e^{-i\frac{\Delta m_{31}^2}{2E}}-1}{-i\frac{\Delta m_{31}^2}{2E}} + (1-\delta_{i3})(1-\delta_{k3})x
\end{aligned} \tag{11.4}$$

Combine them so that

$$\begin{aligned}
S_1(x)_{\beta\alpha} =&(-2i)e^{-i\frac{\Delta m_{31}^2}{4E}x}\sin\left(\frac{\Delta m_{31}^2}{4E}x\right)U_{\beta 3}U_{\alpha 3}^*\left[\frac{a}{\Delta m_{31}^2}(\delta_{\alpha e}+\delta_{\beta e}-2|U_{e3}|^2)-i\frac{a\cdot x}{2E}|U_{e3}|^2\right] \\
&-i\frac{\Delta m_{31}^2}{2E}x\left\{\frac{\Delta m_{21}^2}{\Delta m_{31}^2}U_{\beta 2}U_{\alpha 2}^*+\frac{a}{\Delta m_{31}^2}\left[\delta_{\alpha e}\delta_{\beta e}+U_{\beta 3}U_{\alpha 3}^*(2|U_{e3}|^2-\delta_{\alpha e}-\delta_{\beta e})\right]\right\}
\end{aligned} \tag{11.5}$$

When we come to the next assumption with $\Delta m_{21}^2 \ll \Delta m_{31}^2$ but $2E \cdot V_{CC} \sim \Delta m_{31}^2$ as given in the section 2.2.2, for the derivation of perturbation of oscillation probabilities in matter, we have the explicit eigenvectors as follows:

$$V = \begin{bmatrix} 1 & \frac{c_{12}s_{12}\left(c_{12}^2-s_{12}^2\right)\alpha^2}{A^2}+\frac{c_{12}s_{12}\alpha}{A} & \frac{s_{13}}{A-1}-\frac{A\alpha s_{12}^2 s_{13}}{(A-1)^2} \\ \frac{\alpha^2 c_{12}s_{12}\left(s_{12}^2-c_{12}^2\right)}{A^2}-\frac{\alpha c_{12}s_{12}}{A} & 1 & \frac{(A+1)\alpha c_{12}s_{12}s_{13}}{A} \\ \frac{A\alpha s_{13}s_{12}^2}{(A-1)^2}+\frac{s_{13}}{1-A} & \frac{A\alpha c_{12}s_{12}s_{13}}{1-A} & 1 \end{bmatrix} \tag{11.6}$$

so that the effective mixing matrix $\widetilde{U} = \hat{R}_{23}(\theta_{23})U_\delta V$ with $A \equiv \frac{a}{\Delta m_{31}^2}$:

$$\begin{aligned}
\widetilde{U}_{e1} =&1 \\
\widetilde{U}_{e2} =&\frac{c_{12}s_{12}\alpha^2\left(c_{12}^2-s_{12}^2\right)}{A^2}+\frac{c_{12}s_{12}\alpha}{A} \\
\widetilde{U}_{e3} =&\frac{s_{13}}{A-1}-\frac{As_{12}^2 s_{13}\alpha}{(A-1)^2} \\
\widetilde{U}_{\mu 2} =&c_{23}+\frac{Ac_{12}s_{12}s_{13}s_{23}\alpha e^{i\delta}}{1-A} \\
\widetilde{U}_{\mu 3} =&\frac{(A+1)c_{12}c_{23}s_{12}s_{13}\alpha}{A}+s_{23}e^{i\delta} \\
\widetilde{U}_{\tau 3} =&-\frac{(A+1)c_{12}s_{12}s_{13}s_{23}\alpha}{A}+c_{23}e^{i\delta}
\end{aligned} \tag{11.7}$$

11.2 Details of neutrino fluxes and cross sections in simulations

To facilitate the neutrino oscillation simulations at a certain experiment, we need to implement the neutrino beam energy, how many flavors in the beam, the baseline between neutrino sources and detectors, the detector resolutions. Meanwhile, the useful running time for the luminosity is needed. In addition, we have to include all the uncertainties and backgrounds relevant to them in order to perform the likelihood analysis. The more details gathered in the simulation, the more realistic results we could obtain. Since we perform all the simulations at a neutrino factory, we pay much more attention to neutrino productions from muon decays.

Neutrino fluxes by Muon decays

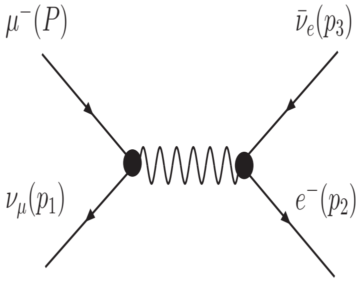

Figure 11.1: A tree-level Feynman diagram for muon decays.

As given in Fig. 11.1, the tree level Feynman diagram for muon decays in Standard Model provides us with the following amplitude:

$$\begin{aligned} i\mathcal{M} &= \left[\bar{u}(p_1)\frac{-ie\gamma_\mu P_L}{\sqrt{2}\sin\theta_w}u(P)\right]\frac{-ig^{\mu\nu}}{q^2-m_W^2+i\varepsilon}\left[\bar{u}(p_2)\frac{-ie\gamma_\nu P_L}{\sqrt{2}\sin\theta_w}v(p_3)\right] \\ &\approx \frac{+i}{-m_W^2}\left(\frac{e^2}{2\sin^2\theta_w}\right)\left[\bar{u}(p_1)\gamma^\mu P_L u(P)\right]\left[\bar{u}(p_2)\gamma_\mu P_L v(p_3)\right] \end{aligned} \tag{11.8}$$

In the second line, we use the approximation:$q^2 \ll m_W^2$. Therefore, with $e = g_2 \sin\theta_w$ in mind, the spin-summed and -averaged amplitude squared is:

$$\begin{aligned} \sum_s |\mathcal{M}|^2 &= \frac{2g_2^4}{m_W^4}(p_1\cdot p_2)(P\cdot p_3) \\ &= 64G_F^2(p_1\cdot p_2)(P\cdot p_3) \end{aligned} \tag{11.9}$$

We take use of $\frac{G_F}{\sqrt{2}} = \frac{g_2^2}{8m_W^2}$ in the last line. The muon differential decay rate has the form:

$$\boxed{d\Gamma = \frac{1}{2m_\mu}\prod_{i=1}^{3}\frac{d^3\,\vec{\mathbf{p_i}}}{(2\pi)^3 2E_i}\sum_s|\mathcal{M}|^2(2\pi)^4\delta^{(4)}(P-\sum_i p_i)} \tag{11.10}$$

In terms of Lorentz invariance, the following statement always holds that:

$$\int\frac{d^3\,\vec{\mathbf{p_2}}}{(2\pi)^3 2E_2}\int\frac{d^3\,\vec{\mathbf{p_3}}}{(2\pi)^3 2E_3}(2\pi)^4\delta^{(4)}(X-p_2-p_3)p_2^\alpha p_3^\beta = Ag^{\alpha\beta}X^2 + BX^\alpha\beta\,, \tag{11.11}$$

with dimensionless constants A and B. It seems like to deal with a 2-body phase space integration, choosing $X^2\ 0, \vec{X}= 0$. At first, we can choose $\alpha = \beta = 0$, the equation becomes:

$$\int\frac{d^3\,\vec{\mathbf{p_2}}}{(2\pi)^3 2E_2}\int\frac{d^3\,\vec{\mathbf{p_3}}}{(2\pi)^3 2E_3}(2\pi)^4\delta^{(4)}(X-p_2-p_3)E_2E_3 = (A+B)X^2 \tag{11.12}$$

Proof:

$$\begin{aligned}\text{LHS} &= \frac{1}{4\times(2\pi)^2}\int d^3\,\vec{\mathbf{p_2}}\int d^3\,\vec{\mathbf{p_3}}\;\delta^{(4)}(X-p_2-p_3)\\ &= \frac{1}{16\pi^2}\int d^3\,\vec{\mathbf{p_2}}\;\delta(X^0-2|\,\vec{\mathbf{p_2}}\,|)\\ &= \frac{1}{16\pi^2}(2\pi)\int|\,\vec{\mathbf{p_2}}\,|^2 d\,\vec{\mathbf{p_2}}\;\delta(X^0-2|\,\vec{\mathbf{p_2}}\,|)\\ &= \frac{1}{8\pi}\left(\frac{X}{2}\right)^2\\ &= \frac{X^2}{32\pi}\end{aligned} \tag{11.13}$$

Second, the master equation can be multiplied by $g^{\alpha\beta}$ and with $p_2\cdot p_3=\frac{1}{2}X^2$ becomes:

$$\int\frac{d^3\,\vec{\mathbf{p_2}}}{(2\pi)^3 2E_2}\int\frac{d^3\,\vec{\mathbf{p_3}}}{(2\pi)^3 2E_3}(2\pi)^4\delta^{(4)}(X-p_2-p_3)\frac{1}{2}X^2=(4A+B)X^2 \tag{11.14}$$

Proof:

$$\begin{aligned}\text{LHS} &= \frac{1}{8\times(2\pi)^2}\int\frac{d^3\,\vec{\mathbf{p_2}}}{|\,\vec{\mathbf{p_2}}\,|^2}\delta(X-2|\,\vec{\mathbf{p_2}}\,|)X^2\\ &= \frac{1}{16\pi}X^2\end{aligned} \tag{11.15}$$

Combine both of reduced equations, we can obtain the value of constants: $A=\frac{1}{96\pi}$ and $B=\frac{1}{48\pi}$. It means that:

$$[\cdots]\equiv\int\frac{d^3\,\vec{\mathbf{p_2}}}{(2\pi)^3 2E_2}\int\frac{d^3\,\vec{\mathbf{p_3}}}{(2\pi)^3 2E_3}(2\pi)^4\delta^{(4)}(X-p_2-p_3)p_2^\alpha p_3^\beta=\frac{1}{96\pi}\left[g^{\alpha\beta}(P-p_1)^2+2(P-p_1)^\alpha(P-p_1)^\beta\right] \tag{11.16}$$

Now 3-body phase space goes on like this:

$$\begin{aligned}\int\frac{d^3\,\vec{\mathbf{p_1}}}{(2\pi)^3 2E_1}[\cdots]p_{1\alpha}P_\beta &= \frac{1}{96\pi}\frac{1}{(2\pi)^3}(4\pi)\int\frac{E_1 dE_1}{2}\left\{m_\mu E_1(m_\mu^2-2m_\mu E_1)+2m_\mu E_1(m_\mu^2-2m_\mu E_1)\right\}\\ &= \frac{m_\mu^6}{24\cdot 2^4(2\pi)^3}\int(3-2x_1)x_1^2 dx_1\,,\end{aligned} \tag{11.17}$$

with $x_1\equiv\frac{2E_1}{m_\mu}$ so that the differential decay rate is:

$$\boxed{\frac{d\Gamma}{dx_1}=\frac{m_\mu^6}{24\cdot 2^4(2\pi)^3}\times\frac{1}{2m_\mu}\times 64G_F^2x_1^2(3-2x_1)=\frac{G_F^2m_\mu^5}{96\pi^3}x_1^2(3-2x_1)} \tag{11.18}$$

Similarly, we can set $Y=P-p_3$ so that we can make use of $[\cdots]=\frac{1}{96\pi}[g^{\alpha\beta}(P-p_3)^2+2(P-p_3)^\alpha(P-p_3)^\beta]$. Then we can integrate out first p_1 and p_2 like this:

$$\begin{aligned}\int\frac{d^3\,\vec{\mathbf{p_3}}}{(2\pi)^3 2E_3}[\cdots]p_1^\alpha p_2^\beta &= \frac{1}{96\pi}\frac{1}{(2\pi)^3}(4\pi)\int\frac{|\,\vec{\mathbf{p_3}}\,|^2 d|\,\vec{\mathbf{p_3}}\,|}{2E_3}\times 6\left[(P\cdot p_3)(P-p_3)^2\right]\\ &= \frac{m_\mu^6}{4\times(2\pi)^3\times 2^4}\int x_3^2(1-x_3)dx_3\end{aligned} \tag{11.19}$$

Finally, we arrive at:

$$\boxed{\frac{d\Gamma}{dx_3} = \frac{m_\mu^6}{4\cdot 2^4(2\pi)^3} \times \frac{1}{2m_\mu} \times 64G_F^2x_3^2(1-x_3) = \frac{G_F^2m_\mu^5}{16\pi^3}x_3^2(1-x_3)} \tag{11.20}$$

In experiment, almost all quantities are observed or measured in the laboratory frame. It's necessary to translate the center of mass frame (C.M. frame) into the laboratory frame before any application in experiment. We can set the high-energy muon moves long the z axis with velocity $\beta = p_\mu/E_\mu \approx 1$ and a Lorentz boost factor $\gamma = \frac{1}{\sqrt{1-\beta^2}} = E_\mu/m_\mu \gg 1$. From now on, quantities in the C.M. frame will be labeled with the superscript $\bigstar$. We need the neutrino spectra in terms of the laboratory quantities E_ν, θ, and ϕ, where the zenithal angle ϕ must be uniform in all space. We seek the transformation:

$$\frac{d^2\Gamma}{dE_1 d\cos\theta} = \frac{d^2\Gamma}{dE_1^\bigstar d\cos\theta^\bigstar}\mathcal{J}(E_1^\bigstar, \cos\theta^\bigstar; E_1, \cos\theta)\,, \tag{11.21}$$

$$\frac{d^2\Gamma}{dE_3 d\cos\theta} = \frac{d^2\Gamma}{dE_3^\bigstar d\cos\theta^\bigstar}\mathcal{J}(E_3^\bigstar, \cos\theta^\bigstar; E_3, \cos\theta) \tag{11.22}$$

Take the muon neutrino for instance. We can express its 4-vector momentum in different frames without loss of generality:

$$\text{In C.M. frame,} \quad p_1^{\bigstar\alpha} = (E_1^\bigstar, 0, E_1^\bigstar\sin\theta^\bigstar, E_1^\bigstar\cos\theta^\bigstar) \tag{11.23}$$

$$\text{In Laboratory frame,} \quad p_1^\beta = (E_1, 0, E_1\sin\theta, E_1\cos\theta) \tag{11.24}$$

According to Lorentz boosts, the muon neutrino energy and momentum component along the z axis p_1^z are given by

$$E_1 = \gamma(E_1^\bigstar + \beta\mathbf{p}_{1z}^\bigstar) \tag{11.25}$$

$$\mathbf{p}_{1z} = \gamma(\beta E_1^\bigstar + \mathbf{p}_{1z}^\bigstar)\,. \tag{11.26}$$

The equation (11.25) means that neutrinos will get a higher energy in the laboratory, given the angle $\theta^\bigstar \approx 0$ and $\gamma \gg 1$. Thus the amount of neutrinos in the forward direction with a given laboratory angle depends on the relativistic velocity of muons. The smaller the laboratory angles, the higher energy neutrinos will have.

It's easy to get the differential:

$$\begin{cases} \frac{\partial E_1^\bigstar}{\partial E_1} = \gamma(1-\beta\cos\theta) \\ \frac{\partial E_1^\bigstar}{\partial\cos\theta} = -\gamma\beta E_1 \\ \frac{\partial\cos\theta^\bigstar}{\partial E_1} = 0 \\ \frac{\partial\cos\theta^\bigstar}{\partial\cos\theta} = \frac{1-\beta^2}{(1-\beta\cos\theta)^2} \end{cases} \tag{11.27}$$

It's easy to see:

$$\mathcal{J}(E_1^\bigstar, \cos\theta^\bigstar; E_1, \cos\theta) = \begin{vmatrix} \gamma(1-\beta\cos\theta) & -\gamma\beta E_1 \\ 0 & \frac{1-\beta^2}{(1-\beta\cos\theta)^2} \end{vmatrix} = \frac{1}{\gamma(1-\beta\cos\theta)} \tag{11.28}$$

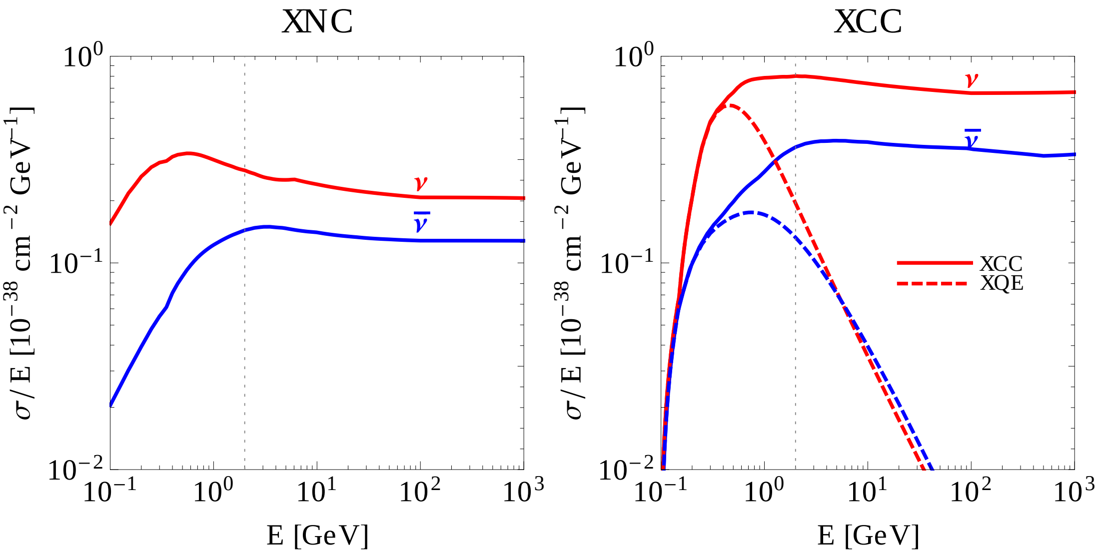

Figure 11.2: *The cross sections of neutrino and antineutrinos. “XNC” denotes the neutral current cross sections and “XCC” is the total charge current cross sections. In addition, “XQE” in dashed lines expresses the quasi-elastic charge current cross sections. The gray dotted vertical line sets the energy threshold of MIND in terms of the latest migration matrices [108, 109].*

In the lab frame, we get the unpolarized decay spectra:

$$\frac{d^2\Gamma}{dE_1 d\cos\theta} = \frac{G_F^2 m}{24\pi^3}\gamma(1-\beta\cos\theta)E_1^2\left[3m - 4\gamma E_1(1-\beta\cos\theta)\right] , \tag{11.29}$$

$$\frac{d^2\Gamma}{dE_3 d\cos\theta} = \frac{G_F^2 m}{4\pi^3}\gamma(1-\beta\cos\theta)E_3^2\left[m - 2\gamma E_3(1-\beta\cos\theta)\right] . \tag{11.30}$$

Cross sections

The neutrino interactions at a relatively low energy range ($\ll 10^3$ GeV) are provided, as shown in Fig. 11.2. It gives the charge and neutral current cross sections. When the neutrino energy is larger than 1 GeV, the cross section is almost flat. In addition, we depict the cross sections induced by quasi-elastic charge current interactions. These cross sections are included in the simulation software GLoBES [85,86] in sequence by data files separately.

Acknowledgments

I am deeply grateful to Professor Reinhold Rückl who agrees to be my official supervisor and Walter Winter for an admission into his group. Walter's fast explanations, self-organizations and deep physics ideas have transmitted to me his professional and genuine enthusiasm in doing physics over these years. Meanwhile, our group members Toshihiko Ota, Davide Meloni, Carlos Yaguna, Svenja Hümmer, Phillip Baerwald, and Martin Krause share their physics understandings with me. It helps me a lot and I really appreciate that. Especially, I cannot present the German abstract without the help from Phillip Baerwald. In addition, I warmly thank Patrick Huber for his stimulating collaboration and kindly hospitality at Virginia Tech. Then I would like to remember Sanjib K. Agarwalla for many fruitful collaborations and other members of IDS-NF for interesting discussions.

I thank all the members of GRK1147 research training group for suggestions and advice, especillally for those in my Beutreuungskommission. The four-month financial support of the final period in the GRK1147 really helps me out of risk. In addition, I should say thanks to our colleagues in the TPII. Prof. Werner Porod agrees to write the letter of recommedation for me. Ben O'Leary kindly offers English proof readings to my thesis. Without Alexander Schenkel's help, it is impossible to move into my current apartment. I am also grateful to the soccer participants in our institute. Every Tuesday we enjoy our games and beer. Awesome! Besides, I should devote many thanks to Christian Speckner and Matthias Bruhnke for our social activities at KaffeeKluge.

Moreover, my family supports my study all the time. I owe them too much. They ask me to take care of myself anytime and anywhere, and leave little worries to me, and teach me how to get along with others properly. Especially, my wife Jing-Fei Dong salvages my insane at the end of my PhD period and encourages me to finish it in time anyway.

In the end, many thanks should be devoted to Chinese students at Wuerzburg. You guys organize so many interesting parties and other activities. It is especially a lot of fun to share physics ideas and jokes with Chinese students Gang Li, Chao-Xing Liu, and Hai-Qing Zhong from our physics faculty during lunch time. Thanks a lot.

Bibliography

[1] M. C. Gonzalez-Garcia and M. Maltoni, Phys. Rept. **460**, 1 (2008), `0704.1800`.

[2] Y. Fukuda *et al.* (Super-Kamiokande), Phys. Rev. Lett. **81**, 1562 (1998), `hep-ex/9807003`.

[3] P. Adamson *et al.* (MINOS), Phys. Rev. Lett. **101**, 131802 (2008), `0806.2237`.

[4] Q. R. Ahmad *et al.* (SNO), Phys. Rev. Lett. **89**, 011301 (2002), `nucl-ex/0204008`.

[5] T. Araki *et al.* (KamLAND), Phys. Rev. Lett. **94**, 081801 (2005), `hep-ex/0406035`.

[6] M. Apollonio *et al.* (CHOOZ), Eur. Phys. J. **C27**, 331 (2003), `hep-ex/0301017`.

[7] G. L. Fogli, E. Lisi, A. Marrone, A. Palazzo, and A. M. Rotunno, Phys. Rev. Lett. **101**, 141801 (2008), `0806.2649`.

[8] K. Abe *et al.* (T2K Collaboration), Phys.Rev.Lett. **107**, 041801 (2011), `1106.2822`.

[9] P. Adamson *et al.* (MINOS Collaboration), Phys.Rev.Lett. (2011), `1108.0015`.

[10] T. Adam *et al.* (OPERA Collaboration) (2011), `1109.4897`.

[11] A. Aguilar *et al.* (LSND), Phys. Rev. **D64**, 112007 (2001), `hep-ex/0104049`.

[12] M. Maltoni and T. Schwetz, Phys. Rev. **D76**, 093005 (2007), `0705.0107`.

[13] S. Palomares-Ruiz, S. Pascoli, and T. Schwetz, JHEP **09**, 048 (2005), `hep-ph/0505216`.

[14] A. A. Aguilar-Arevalo *et al.* (The MiniBooNE) (2010), `1007.1150`.

[15] J. Hamann, S. Hannestad, G. G. Raffelt, I. Tamborra, and Y. Y. Y. Wong (2010), `1006.5276`.

[16] M. Apollonio *et al.* (2002), `hep-ph/0210192`.

[17] C. Albright *et al.* (Neutrino Factory/Muon Collider) (2004), `physics/0411123`.

[18] A. Bandyopadhyay *et al.* (ISS Physics Working Group) (2007), `arXiv:0710.4947[hep-ph]`.

[19] T. Abe *et al.* (ISS Detector Working Group), JINST **4**, T05001 (2009), `0712.4129`.

[20] J. S. Berg *et al.* (ISS Accelerator Working Group) (2008), `0802.4023`.

[21] *International design study of the neutrino factory*, `http://www.ids-nf.org`.

[22] P. Huber and W. Winter, Phys. Rev. **D68**, 037301 (2003), `hep-ph/0301257`.

[23] V. Barger, S. Geer, and K. Whisnant, Phys. Rev. **D61**, 053004 (2000), `hep-ph/9906487`.

[24] A. Cervera *et al.*, Nucl. Phys. **B579**, 17 (2000), `hep-ph/0002108`.

[25] J. Burguet-Castell, M. B. Gavela, J. J. Gomez-Cadenas, P. Hernandez, and O. Mena, Nucl. Phys. **B608**, 301 (2001), `hep-ph/0103258`.

[26] M. Freund, P. Huber, and M. Lindner, Nucl. Phys. **B615**, 331 (2001), `hep-ph/0105071`.

[27] A. Donini, E. Fernandez-Martinez, D. Meloni, and S. Rigolin, Nucl. Phys. **B743**, 41 (2006), `hep-ph/0512038`.

[28] P. Huber, M. Lindner, M. Rolinec, and W. Winter, Phys. Rev. **D74**, 073003 (2006), `hep-ph/0606119`.

[29] R. Gandhi and W. Winter, Phys. Rev. **D75**, 053002 (2007), `hep-ph/0612158`.

[30] J. Kopp, T. Ota, and W. Winter, Phys. Rev. **D78**, 053007 (2008), `0804.2261`.

[31] N. C. Ribeiro, H. Minakata, H. Nunokawa, S. Uchinami, and R. Zukanovich-Funchal, JHEP **12**, 002 (2007), `0709.1980`.

[32] J. Tang and W. Winter, Phys. Rev. **D80**, 053001 (2009), `arXiv:0903.3039`.

[33] S. Antusch, C. Biggio, E. Fernandez-Martinez, M. B. Gavela, and J. Lopez-Pavon, JHEP **10**, 084 (2006), `hep-ph/0607020`.

[34] E. Fernandez-Martinez, M. B. Gavela, J. Lopez-Pavon, and O. Yasuda, Phys. Lett. **B649**, 427 (2007), `hep-ph/0703098`.

[35] A. Abada, C. Biggio, F. Bonnet, M. B. Gavela, and T. Hambye, JHEP **12**, 061 (2007), `0707.4058`.

[36] S. Goswami and T. Ota, Phys. Rev. **D78**, 033012 (2008), `0802.1434`.

[37] M. Malinsky, T. Ohlsson, and H. Zhang (2009), `0903.1961`.

[38] D. Meloni, T. Ohlsson, W. Winter, and H. Zhang, JHEP **04**, 041 (2010), `0912.2735`.

[39] P. Huber, T. Schwetz, and J. W. F. Valle, Phys. Rev. **D66**, 013006 (2002), `hep-ph/0202048`.

[40] S. Antusch, J. P. Baumann, and E. Fernandez-Martinez, Nucl. Phys. **B810**, 369 (2009), `0807.1003`.

[41] M. Blennow, D. Meloni, T. Ohlsson, F. Terranova, and M. Westerberg, Eur. Phys. J. **C56**, 529 (2008), `0804.2744`.

[42] T. Ohlsson and H. Zhang, Phys. Lett. **B671**, 99 (2009), `0809.4835`.

[43] M. Malinsky, T. Ohlsson, and H. Zhang, Phys. Rev. **D79**, 011301 (2009), `0811.3346`.

[44] M. B. Gavela, D. Hernandez, T. Ota, and W. Winter, Phys. Rev. **D79**, 013007 (2009), `0809.3451`.

[45] S. Geer, O. Mena, and S. Pascoli, Phys. Rev. **D75**, 093001 (2007), `hep-ph/0701258`.

[46] A. D. Bross, M. Ellis, S. Geer, O. Mena, and S. Pascoli, Phys. Rev. **D77**, 093012 (2008), `0709.3889`.

[47] P. Huber and W. Winter, Phys. Lett. **B655**, 251 (2007), `0706.2862`.

[48] A. Bross *et al.*, Phys. Rev. **D81**, 073010 (2010), `0911.3776`.

[49] A. Dighe, S. Goswami, and S. Ray (2010), `1009.1093`.

[50] C. Giunti, C. W. Kim, and W. P. Lam, Phys. Rev. D **43**(1), 164 (1991).

[51] A. Dziewonski and D. Anderson, Phys. Earth Planet. Inter. **25**, 297 (1981).

[52] L. Wolfenstein, Phys. Rev. **D17**, 2369 (1978).

[53] L. Wolfenstein, Phys. Rev. **D20**, 2634 (1979).

[54] J. Liu, Phys. Rev. D **45**(4), 1428 (1992).

[55] K. Nakamura and P. D. Group, Journal of Physics G: Nuclear and Particle Physics **37**(7A), 075021 (2010), URL `http://stacks.iop.org/0954-3899/37/i=7A/a=075021`.

[56] E. K. Akhmedov, R. Johansson, M. Lindner, T. Ohlsson, and T. Schwetz, JHEP **04**, 078 (2004), `hep-ph/0402175`.

[57] P. Huber, M. Lindner, and W. Winter, Nucl. Phys. **B645**, 3 (2002), `hep-ph/0204352`.

[58] V. Barger, D. Marfatia, and K. Whisnant, Phys. Rev. **D65**, 073023 (2002), `hep-ph/0112119`.

[59] G. Giacomelli and M. Sioli (2002), `hep-ex/0211035`.

[60] E. K. Akhmedov pp. 103–164 (1999), `hep-ph/0001264`.

[61] M. Honda, T. Kajita, K. Kasahara, S. Midorikawa, and T. Sanuki, Phys.Rev. **D75**, 043006 (2007), `astro-ph/0611418`.

[62] K. Sato and H. Suzuki, Phys. Rev. Lett. **58**(25), 2722 (1987).

[63] C. B. Bratton, D. Casper, A. Ciocio, R. Claus, M. Crouch, S. T. Dye, S. Errede, W. Gajewski, M. Goldhaber, T. J. Haines, T. W. Jones, D. Kielczewska, *et al.*, Phys. Rev. D **37**(12), 3361 (1988).

[64] E. N. Alekseev, L. N. Alekseeva, I. V. Krivosheina, and V. I. Volchenko, Phys. Lett. **B205**, 209 (1988).

[65] P. Lipari, Nucl.Phys.Proc.Suppl. **112**, 274 (2002), `hep-ph/0207172`.

[66] M. Diwan *et al.* (MINOS), *A study of* $\nu_\mu \to \nu_e$ *sensitivity in MINOS*, Tech. Rep. NuMI-L-714 (2001).

[67] Y. Ashie *et al.* (Super-Kamiokande Collaboration), Phys.Rev.Lett. **93**, 101801 (2004), `hep-ex/0404034`.

[68] IceCube,
`http://icecube.wisc.edu/`.

[69] Borexino,
`http://borex.lngs.infn.it/`.

[70] ICARUS,
`http://icarus.lngs.infn.it/`.

[71] M. Freund, P. Huber, and M. Lindner, Nucl. Phys. **B585**, 105 (2000), `hep-ph/0004085`.

[72] J. N. Bahcall, A. M. Serenelli, and S. Basu, Astrophys.J. **621**, L85 (2005), `astro-ph/0412440`.

[73] B. Aharmim *et al.* (SNO Collaboration), Phys.Rev. **C72**, 055502 (2005), `nucl-ex/0502021`.

[74] M. Ahn *et al.* (K2K Collaboration), Phys.Rev. **D74**, 072003 (2006), `hep-ex/0606032`.

[75] K. Eguchi *et al.* (KamLAND), Phys. Rev. Lett. **90**, 021802 (2003), `hep-ex/0212021`.

[76] M. Maltoni, T. Schwetz, M. A. Tortola, and J. W. F. Valle, New J. Phys. **6**, 122 (2004), `hep-ph/0405172`.

[77] T. Schwetz, M. Tortola, and J. Valle, New J.Phys. **13**, 109401 (2011), `1108.1376`.

[78] LBNE,
`http://lbne.fnal.gov/`.

[79] L. P. Ekstrom and R. B. Firestone WWW Table of Radioactive Isotopes, database version 2/28/99 from URL http://ie.lbl.gov/toi/.

[80] A. Cervera, A. Laing, J. Martin-Albo, and F. J. P. Soler (2010), `1004.0358`.

[81] A. Laing, *Optimization of Detectors for the Golden Channel at a Neutrino Factory*, Ph.D. thesis, Glasgow university (2010).

[82] J. Bernabeu, M. Blennow, P. Coloma, A. Donini, C. Espinoza, *et al.* (2010), `1005.3146`.

[83] S. Geer, Phys. Rev. **D57**, 6989 (1998), `hep-ph/9712290`.

[84] A. De Rujula, M. B. Gavela, and P. Hernandez, Nucl. Phys. **B547**, 21 (1999), `hep-ph/9811390`.

[85] P. Huber, M. Lindner, and W. Winter, Comput. Phys. Commun. **167**, 195 (2005), `http://www.mpi-hd.mpg.de/lin/globes/`, `hep-ph/0407333`.

[86] P. Huber, J. Kopp, M. Lindner, M. Rolinec, and W. Winter, Comput. Phys. Commun. **177**, 432 (2007), `hep-ph/0701187`.

[87] NOMAD (2008), `0812.4543`.

[88] D. Indumathi and N. Sinha, Phys.Rev. **D80**, 113012 (2009), `arXiv:0910.2020`.

[89] A. Donini, J. J. Gomez Cadenas, and D. Meloni (2010), `1005.2275`.

[90] R. Acquafredda *et al.* (OPERA), New J. Phys. **8**, 303 (2006), `hep-ex/0611023`.

[91] A. Donini, D. Meloni, and P. Migliozzi, Nucl. Phys. **B646**, 321 (2002), `hep-ph/0206034`.

[92] D. Autiero *et al.*, Eur. Phys. J. **C33**, 243 (2004), `hep-ph/0305185`.

[93] A. Donini, K.-i. Fuki, J. Lopez-Pavon, D. Meloni, and O. Yasuda, JHEP **08**, 041 (2009), `0812.3703`.

[94] M. C. Gonzalez-Garcia, M. Maltoni, and J. Salvado, JHEP **04**, 056 (2010), `1001.4524`.

[95] R. J. Geller and T. Hara, Phys. Rev. Lett. **49**, 98 (2001), `hep-ph/0111342`.

[96] T. Ohlsson and W. Winter, Phys. Rev. **D68**, 073007 (2003), `hep-ph/0307178`.

[97] S. K. Agarwalla, P. Huber, J. Tang, and W. Winter, JHEP **01**, 120 (2011), `1012.1872`.

[98] W. Winter, Phys. Rev. **D78**, 037101 (2008), `0804.4000`.

[99] S. K. Raut, R. S. Singh, and S. Sankar (2009), `0908.3741`.

[100] V. Barger, M. Dierckxsens, M. Diwan, P. Huber, C. Lewis, *et al.*, Phys.Rev. **D74**, 073004 (2006), `hep-ph/0607177`.

[101] M. Maltoni, T. Schwetz, and J. W. F. Valle, Phys. Rev. **D65**, 093004 (2002), `hep-ph/0112103`.

[102] C. Giunti and C. W. Kim Oxford, UK: Univ. Pr. (2007) 710 p.

[103] C. Giunti, M. Laveder, and W. Winter, Phys. Rev. **D80**, 073005 (2009), `0907.5487`.

[104] D. Meloni, J. Tang, and W. Winter, Phys. Rev. **D82**, 093008 (2010), `1007.2419`.

[105] M. Maltoni, T. Schwetz, M. A. Tortola, and J. W. F. Valle, Phys. Rev. **D67**, 013011 (2003), `hep-ph/0207227`.

[106] P. Adamson *et al.* (The MINOS) (2010), `1001.0336`.

[107] A. Donini, M. Maltoni, D. Meloni, P. Migliozzi, and F. Terranova, JHEP **12**, 013 (2007), `0704.0388`.

[108] M. D. Messier UMI-99-23965.

[109] E. A. Paschos and J. Y. Yu, Phys. Rev. **D65**, 033002 (2002), `hep-ph/0107261`.

List of Tables

List of Figures

List of Publications

1. **Jian Tang** and Walter Winter, Requirements for a New Detector at the South Pole Receiving an Accelerator Neutrino Beam, arXiv:1110.5908 [hep-ph].
2. Davide Meloni, **Jian Tang** and Walter Winter, Arbitrarily massive sterile neutrinos at the neutrino factory, AIP Conf. Proc. **1382**, 97 (2011).
3. International Design Study for the Neutrino Factory: Interim Design Report by S. Choubey, ..., D. Meloni, **J. Tang**, W. Winter, et al. (IDS-NF collaboration) IDS-NF-20, Mar. 2011 *https://www.ids-nf.org/wiki/FrontPage/Documentation/IDR*
4. Sanjib K. Agarwalla, Patrick Huber, **Jian Tang**, Walter Winter Optimization of the Neutrino Factory, revisited arXiv:1012.1872 [hep-ph] *JHEP **01**, 120(2011).*
5. Davide Meloni, **Jian Tang**, Walter Winter Sterile neutrinos beyond LSND at the neutrino factory arXiv:1007.2419 [hep-ph] *Phys. Rev. D **82**, 093008(2010)*
6. **Jian Tang**, Walter Winter Neutrino factory in stages: Low energy, high energy, off-axis arXiv:0911.5052 [hep-ph] *Phys. Rev. D **81**, 033005(2010)*
7. **Jian Tang**, Walter Winter On near detectors at a neutrino factory
   Contributed to 11th International Workshop on Neutrino Factories, Superbeams and Betabeams: NuFact09, Chicago, Illinois, 20-25 Jul 2009.
   arXiv:0909.4667 [hep-ph] *AIP Conf.Proc.1222:88-92,2010.*
8. **Jian Tang**, Walter Winter Physics with near detectors at a neutrino factory arXiv:0903.3039 [hep-ph] *Phys. Rev. D **80**, 053001(2009)*
9. Qing-Peng Qiao, **Jian Tang**, Xue-Qian Li Restudy on Dark Matter Time-Evolution in the Littlest Higgs model with T-parity arXiv:0711.3254 [hep-ph], *Commun. Theor. Phys. **50**: 1211-1218 (2008).*
10. Hong-Wei Ke, **Jian Tang**, Xi-Qing Hao, Xue-Qian Li Analysis on Heavy Quarkonia Transitions with Pion Emission in Terms of the QCD Multipole Expansion and Determination of Mass Spectra of Hybrids arXiv:0706.2074v2[hep-ph] *Phys. Rev. D **76**, 074035 (2007)*

Erklärung

Diese Doktorarbeit wurde am Lehrstuhl für Theoretische Physik II, Theoretische Elementarteilchenphysik, der Julius-Maximilians-Universität Würzburg angefertigt.Ich erkläre hiermit, dass ich diese Dissertation selbständig verfasst und keine anderen als die angegebenen Quellen und Hilfsmittel benutzt habe.Ich erkläre außerdem, dass diese Dissertation weder in gleicher noch in anderer Form bereits in einem anderen Prüfungsverfahren vorgelegen hat.Ich habe früher außer den mit dem Zulassungsgesuch urkundlich vorgelegten Graden keine weiteren akademischen Grade erworben oder zu erwerben versucht.

Jian Tang
Würzburg, 2011